Fontan Circulation

The hemodynamic performance of different conduit sizes

L.C. van ‘t Hul

TU Delft

Erasmus MC
University Medical Center Rotterdam

The hemodynamic performance of different conduit sizes in the Fontan circulation

by

L.C. van ’t Hul

to obtain the degree of Master of Science
at the Delft University of Technology,
to be defended on Thursday July 15th, 2021 at 12.15 pm.

Student number:	4972457	
Project duration:	November, 2021 – July, 2021	
Thesis committee:	Prof. dr. P. French	TU Delft, supervisor
	Dr. ir. J.J. Wentzel	Erasmus MC
	Prof. dr. J. Dankelman	TU Delft
	Dr. A.A.W. Roest	LUMC

An electronic version of this thesis is available at `http://repository.tudelft.nl/`.

TU Delft

Preface

L.C. van 't Hul
Amsterdam, 2021

After a year of hard work, I am proud to present you my final work as a student of the Biomedical Engineering master at the TU Delft. Last year I started full of enthusiasm and excitement this scientific journey. During the past year, I have learned a lot about researching on a topic that is technically and clinically challenging and being part of a highly motivated multidisciplinary team including medical doctors and engineers.

The year has certainly not gone by without setbacks, professionally, but certainly also personally. I have had a lot of support from the people around me, whether or not involved in the project, for which I am extremely grateful. That is why I would like to thank a number of people in this preface.

First of all, my TU Delft supervisor, Prof. dr. Paddy French for the help and feedback during our monthly meetings. Then, my daily supervisor from the Erasmus Medical Center, Dr. Ir. Jolanda Wentzel. I am very grateful that she supported me professionally but also personally during the entire project and got the best out of me. Furthermore, the collaboration with Dr. Arno Roest and Dr. Friso Rijnberg from the LUMC has always been motivating, inspiring, and very helpful. They were always ready to help me out and motivated to take this project to the next level. Then, two fellow students, Tawab Karim and Rosemary Bolt, who were always open to interesting discussions about difficulties we were facing in the project.

In particular I would like to thank the people who have unconditionally supported me outside the project, even in extremely difficult and emotional periods during this year, are Jorijn, my parents, my roommates and closest friends.

Additionally, I am grateful that Prof. dr. Paddy French, Dr. Ir. Jolanda Wentzel, Prof. dr. Jenny Dankelman and dr. Arno Roest are the members of my thesis committee.

Abstract

The Fontan circulation is the final stage of surgical palliation for children born with congenital heart defect with a single ventricle. Currently, the most used procedure to complete the Fontan circulation is the Extracardiac Total Cavopulmonary connection and is performed when the patient is at an age of 3-5 years old. In this procedure, a prosthetic extracardiac conduit is implanted that connect the Inferior Vena Cava directly with the Pulmonary Arteries, bypassing the heart. This extracardiac conduit is available in several conventional sizes. However, little knowledge is available on the performance of these different conduit sizes, especially when patients grow older. Therefore, it is difficult to make a well-informed choice on the conduit size at the time of implantation.

This study aimed to obtain more insight into the performance of three conduit sizes (16, 18 and 20 mm), using computational fluid dynamic simulations conducted on anatomically three-dimensional models with accurate boundary conditions, both reconstructed from MRI (N = 19). In addition, it is proposed in the literature that body growth affects the conduit's performance in the Fontan circulation. In order to include body growth in this study, the effect of an increasing body surface area is analysed for the patients with a 16 and 18 mm conduit implanted. Power loss, pressure drop, normalised resistance and the flow stagnation volume were used as parameters indicating the performance, i.e. efficiency of the Fontan circulation. Furthermore, to get a complete picture of the performance, two physical conditions (rest and exercise) are included and a distinction is made in respiratory phases (inspiration and expiration).

For all three conduit sizes, the power loss, pressure drop and normalised resistance increase with exercise. Also, the power loss and pressure drop increase with inspiration. An increase of these parameters indicate a decreased efficiency of the Fontan circulation. Furthermore, the results describe higher values for the 16 mm conduit than the 18 and 20 mm conduits according to the power loss, pressure drop and normalised resistance, with significant differences found during expiration in rest and exercise. In contrast, flow stagnation volume, decreases with exercise and inspiration, and no clear trend was seen for the flow stagnation volume between the conduit sizes. The flow stagnation levels were close to zero, indicating that the performance is not limited by oversized conduits in these patients.

According to the body growth, for the 16 mm conduit, significant correlations were found between the body surface area and power loss, pressure drop and normalised resistance. No trend was seen for the 18 mm conduit. From these findings it appears that probably a smaller conduit is disadvantageous considering the patient's growth.

In conclusion, the results from this study indicate that the 16 mm conduit is the least beneficial compared to the 18 and 20 mm conduit. However, whether the 18 and 20 mm conduit perform sufficiently is questionable and should be investigated patient-specific by linking these results to clinical relevant parameters such as exercise tolerance. Furthermore, the main limitation of this study is the small patient population. Although already convincing trends have been found, the results should be confirmed by further research with a larger patient population.

Contents

Nomenclature

- *2D* Two dimensional
- *3D* Three dimensional
- *BSA* Body Surface Area
- *CFD* Computational Fluid Dynamics
- *CFL* Courant-Friedrichs-Lewy
- *ECC* Extracardiac Conduit
- *ECG* Electrocardiogram
- *ECTC* Extracardiac Total Cavopulmonary Connection
- *CHD* Congenital Heart Disease
- *HLHS* Hypoplastic Left Heart Syndrome
- *HV* Hepatic Vein
- *IVC* Inferior Vena Cava
- *IQR* Interquartile Range
- *LPA* Left Pulmonary Artery
- *MRI* Magnetic Resonance Imaging
- *PA* Pulmonary Artery
- *PC-MRI* Phase-Contrast Magnetic Resonance Imaging
- *ePFTE* polytetrafluoroethylene
- *RF* Radio Frequency
- *RPA* Right Pulmonary Artery
- *STL* Standard Triangle Language
- *SVC* Superior Vena Cava
- *TCPC* Total Cavopulmonary Connection
- *VAT* Ventilatory Anaerobic Threshold
- *VDR* Viscous Dissipation Rate
- *VMTK* Vascular Modelling Toolkit
- *VTK* Visualization Toolkit
- VO_2 *max* Maximal oxygen uptake

1

Introduction

1.1. Background

Congenital heart disease (CHD) is the most common birth defect and is reported in approximately 4 to 10 out of 1000 childbirths in the general population [1–5]. It is defined as a structural abnormality of the heart present at birth. CHD consists of many types of defects, ranging from relatively simple to complex with life-threatening symptoms. Numerous CHD exists with abnormal vascular connections and underdeveloped ventricles. As a consequence, the standard blood flow in the heart to pump the blood to the aorta is disrupted. The blood flow can be blocked, slow down, directed in the wrong direction or to the wrong location [5, 6].

The cardiovascular system in a healthy human body consists of two blood circulations, the systemic and pulmonary, respectively connected by the left and right heart halves. The left half of the heart (Fig. 1.1 displayed in red) is responsible for the systemic circulation, supplying the body with oxygenated blood coming from the lungs. The oxygenated blood flows via the veins of the lungs, the left atrium and the left ventricle through the aorta to the body. The systemic circulation ends when the blood returns to the atrium of the right half of the heart. The right half of the heart is responsible for the pulmonary circulation (Fig. 1.1 displayed in blue) . In this circulation the deoxygenated blood flows via the right atrium and the right ventricle to the pulmonary arteries. After the blood passed the lungs, the oxygenated blood returns to the left atrium, where the systemic circulation starts again [7].

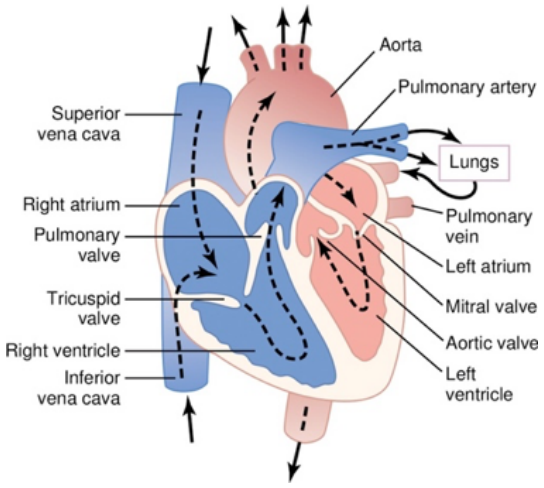

Figure 1.1: Blood flow through the healthy heart [8].

A form of CHD with a highly complex defect is functionally univentricular CHD; this subgroup is characterized by only one completely developed and functional ventricle. The incidence of univentricular CHD ranges up to 0.04% of all newborn. Currently, there are about 22.000 patients with functionally univentricular

CHD in Europe and 50.000 in the USA [9]. Three most prevalent underlying diagnoses are first the hypoplastic left heart syndrome (HLHS), where the left ventricle is underdeveloped (see Fig. 1.2). Second, tricuspid atresia, in which the valves between the right atrium and ventricle are not developed. Third, double inlet left ventricle, which means that both atriums are connected to the left ventricle [9]. Taking these diagnoses together, the underlying anatomical issue is the absence of a functioning second ventricle resulting in non-separated blood circulations. When the circulations are not separated, oxygenated and deoxygenated blood is mixed, causing arterial desaturation. Also, chronic volume overload of the single ventricle is likely to occur, leading to congestive heart failure and eventually dead [10, 11].

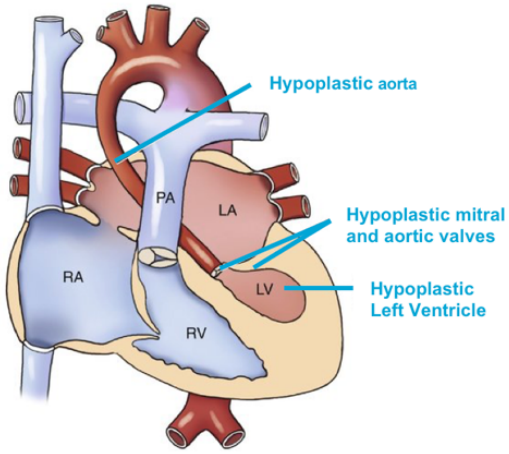

Figure 1.2: Hypoplastic Left Heart Syndrome [12].

1.2. Total Cavopulmonary connection

Since univentricular CHD is a life-threatening disease, these children will die without intervention. Due to the fact that the underlying anatomical problems cannot be resolved directly with a biventricular repair, the surgeon is required to reconstruct parts of the heart so that blood flow directions are restored and the two circulations are separated again [11]. The current intervention used is the Total Cavopulmonary Connection (TCPC); in the case of an HLHS, this is a three-staged surgical palliation procedure. In most other cases, only the last two stages of the TCPC need to be accomplished [13].

The first stage is the Norwood procedure. During this procedure, three connections are created. First, a connection between the main pulmonary artery (PA) and the aorta. Second, a connection between the left and right atria, allowing blood to flow from one side of the heart to the other. Third, a shunt is placed between the pulmonary arteries and the newly formed aorta (Blalock-Taussig shunt) or right ventricle (Sano shunt) to supply the blood to the lungs. Consequently, the single working ventricle pumps mixed blood through the body by the systemic and pulmonary circulation [14].

The Norwood procedure is followed up by the bi-directional Glenn procedure, the second stage. During this stage, the superior vena cava (SVC) is disconnected from the heart and attached to the right PA. The new connection causes deoxygenated blood to flow from the head and arms directly to the lungs, bypassing the heart [15].

The third and final stage is the Fontan procedure. During this last procedure, the two circulations are fully separated. This separation is done by disconnecting the inferior vena cava (IVC) from the heart and attach it, like the SVC, to the PAs. This new form of blood flow circulation is called the Fontan circulation. From this stage on, the heart with just one working ventricle takes care of the systemic circulation, and the direct connection of the SVC and the IVC to the PAs ensures the pulmonary circulation [9, 16]. The Fontan procedure, connecting the IVC to the PAs, can be performed with several techniques. The two most commonly used are either the Intracardiac Total Cavopulmonary Connection, better known as the intracardiac lateral tunnel, or the Extracardiac Total Cavopulmonary Connection (ECTC; see Fig. 1.3) [13].

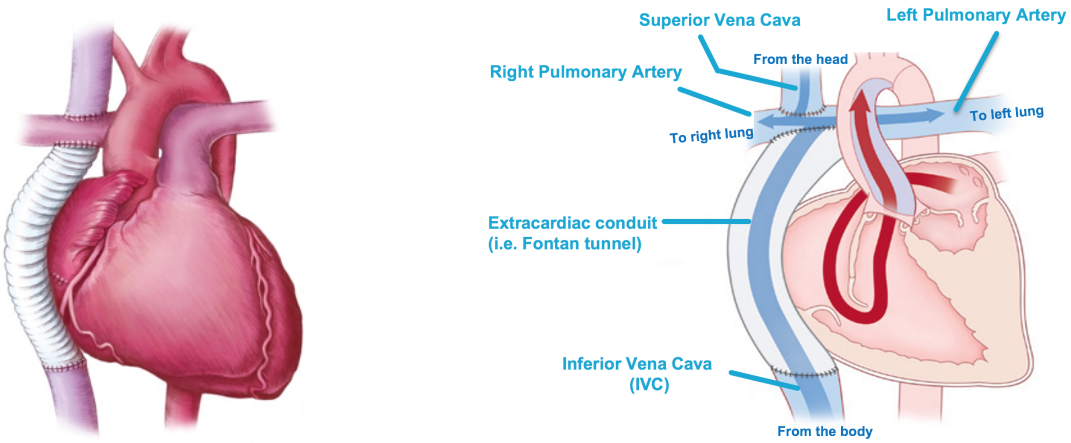

Figure 1.3: Left: Extracardiac total cavopulmonary connection (ECTC) [17]. Right: The bloodflow trough the ECTC [18].

1.3. Extracardiac conduit

Currently, the preferred surgical strategy to create the Fontan circulation is the ECTC technique, using a prosthetic extracardic conduit (ECC), i.e. Fontan tunnel [9, 19–22]. The reasoning for using ECTC over the intracardiac lateral tunnel is based on theoretical advantages. The use of ECTC reduces the risk for arrhythmias by avoiding extensive atrial suture lines and exposure of the atrium to higher venous pressures. Furthermore, theoretically, laminar flow can be achieved in the ECC, avoiding turbulence and stasis, resulting in lower energy losses [23–26]. These theoretical advantages are supported by experimental studies that show optimized flow dynamics, lower frequency of atrial arrhythmias and technical ease of the procedure [27, 28].

Several types of ECCs are available for completion of the ECTC. However, Gore-Tex grafts are most commonly used during the Fontan procedure. These grafts are made of polytetrafluoroethylene (i.e. ePTFE) and most frequently used because of the minimal peel formation and good resistance to calcification compared to several other types such as the Dacron conduit [29, 30]. The Gore-Tex grafts are commercially available in several conventional sizes, ranging from 14 to 26 mm in diameter. At the time of ECTC completion the patient is around 3 years old. At this age, the patient's vessels are considered of sufficient size to attach the prosthetic conduit [19]. However, the conduit is a rigid tube that will not grow with the patient's somatic growth. This rigidity makes careful selection of the conduit size of high importance, meaning not only considering the most suitable conduit size at the time of implantation but also the expected performance of the conduit in the body when these children grow older.

1.4. Performance conduit sizes

To better understand the conduit's performance in the patient's body after implantation, there are two approaches: a) a technical approach, looking into the hemodynamics, and b) considering clinical parameters affected by the conduit size. From the literature, it appears that little is known regarding the performance of the conduit with respect to its diameter size. However, few interesting conclusions can be retrieved from the studies found.

First, in the studies considering hemodynamics, mainly blood flow stagnation volume and energy loss are used as performance parameters. High levels of blood flow stagnation volume and energy loss are considered harmful due to high-risk of low flow induced thrombosis and blood flow inefficiency in the ECTC. Inefficient ECTC with high energy losses can cause Fontan complications such as exercise intolerance, protein losing enteropathy and liver fibrosis [31, 32]. The studies found conclude that a larger conduit size, in a range from 10 to 30 mm in diameter, corresponds to increased blood flow stagnation volumes and, for patients under the age of ten, lower energy losses until an optimum size of 20 mm [33, 34].

Second, the studies concerning clinical performance of the conduit included the following relevant parameters: exercise capacity, mortality and morbidity. It was found that a conduit of 18 or 20 mm provides

the best results for an optimal exercise capacity [35]. Also, conduits smaller than 16 mm are related to significantly higher mortality rates [36]. Lastly, small-sized patients with a conduit larger than 16 mm result in higher occurrences of thrombosis than in a small-sized patient with a 16 mm conduit implanted [37].

In addition, several studies found that the used performance parameters are not affected by the conduit size only but also by other variables: the IVC size in relation to the conduit size, the body growth, the respiration phase, and the exercise condition [33, 38–40]. The results found on the effect of these variables will be briefly discussed.

IVC size First of all, the IVC diameter size in proportion with the conduit diameter size seems to be important in order of blood flow efficiency; a discrepancy between the IVC and the conduit causes a sudden increase or decrease in blood velocity. Such a acceleration or deceleration appear to result in higher or lower energy losses (Fig. 1.4: left) [38, 40].

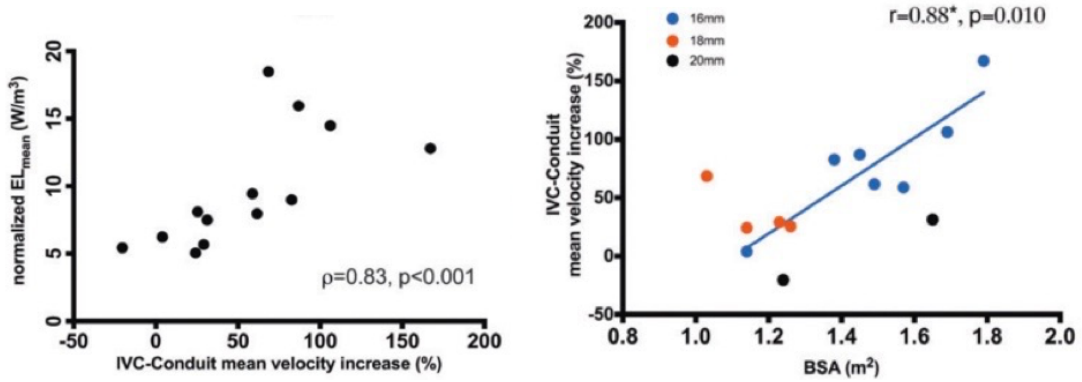

Figure 1.4: Left: Relation IVC-conduit mean velocity increase and normalized mean energy loss. Right: Relation BSA and IVC-conduit mean velocity increase (%) [40].

Body growth The study of Rijnberg et al. [40] found, for patients with a 16 mm conduit, a relation between a larger body surface area (BSA) and IVC-conduit mean velocity increase, resulting in higher energy losses (Fig. 1.4: right). In other words, body growth result in disadvantageous hemodynamics for patients with a 16 mm conduit implanted. Also, the study of Hagler et al. [39] found that body growth is the main cause for stenosed, i.e. narrowed, conduits in adult patients. This stenosis is a consequence of strechting, in length, of the conduit. However, both studies lack information to generalize these findings for all conduit sizes.

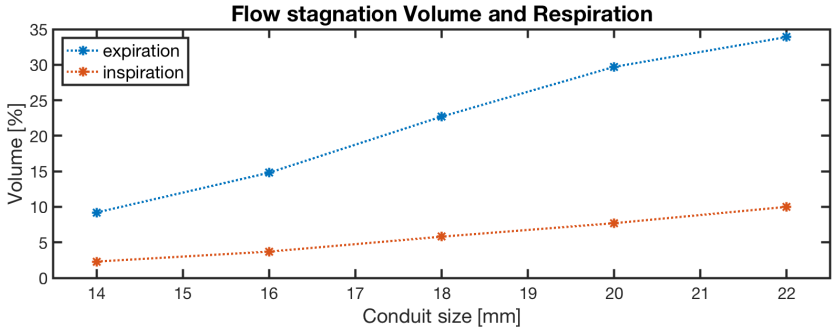

Figure 1.5: Flow stagnation volume during inspiration and expiration phase for different conduit sizes [33].

Respiration The effect of the respiration phase, either inspiration or expiration, is studied by Itatani et al. (2009) [33]. Their study demonstrated that respiration influences hemodynamics; the blood flow rate increases with inspiration and decreases again with expiration. Consequently lower values of blood flow stagnation volumes are found in inspiration and higher volumes in expiration. Fig.1.5 shows the blood flow stag-

nation volume, defined as the volume of blood with a flow velocity below 0.01m/s, as a function of conduit size for inspiration and expiration.

Physical condition Most studies only included performance measurements in a resting condition, whereas the study of Itatani et al. [33] showed the influence of two exercise levels on the conduit performance considering flow stagnation volume (Fig. 1.6). From their findings it appears that the exercise condition result in lower flow stagnation volumes, which is a considerable positive effect with less chance of thrombus formation.

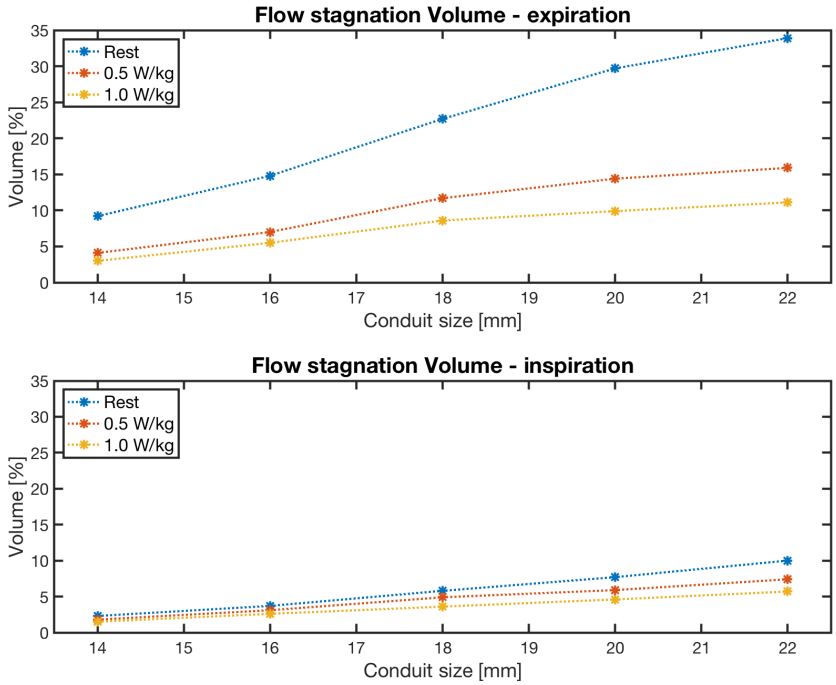

Figure 1.6: Flow stagnation volume as function of conduit size for expiration (top) and inspiration (bottom) in a resting and two exercise conditions [33].

1.5. Research gap

Overall, the available literature indicates the relatively good performance of implanted conduit sizes of 16 mm in diameter or larger. However, the results are difficult to generalize because of the scarce availability of studies in the literature on this topic. Furthermore, the small and young patient populations, variation in methodologies and diversity in measured parameters, make comparison of the found studies complicated. To conclude, no study exist that has yet researched all relevant parameters and variables at once. Consequently, there is still a research gap regarding the performance of different implanted conduit sizes, due to lacking information on the relevant parameters and variables for a considerable large and grown-up patient population. This research gap makes a well-informed choice on the best conduit size for the Fontan procedure complicated with respect to the growing patient.

1.6. Research question

This research aims to answer the following research question: How do different implanted conduit sizes perform hemodynmaically in Fontan patients, considering the influence of respiration, physical condition and body growth? In order to find an answer to this question, the study is subdivided into two parts. In the first part, the performance of three implanted conduit sizes (16, 18 & 20 mm) is compared in resting and exercise condition. In the second part, the effect of body growth, using BSA, on the performance of two different implanted conduit sizes (16 & 18 mm) is analysed in resting and exercise condition. For both parts, the influence of respiration will be taken into account.

2

Methods

In this chapter, the complete research pipeline is described, and the following topics will be discussed: patient selection, background on the used applied technologies: Computational Fluid Dynamics (CFD) and Magnetic Resonance Imaging (MRI), procedural steps needed before simulation of the blood flow in the ECTC using CFD (i.e. pre-processing), the simulation using CFD (i.e. processing), the analysis of the outcome data from CFD (i.e. post-processing) and the statistical methods. Additionally, a schematic overview of the pipeline is given in Appendix A.1.

2.1. Patient population

In total, nineteen patients with Fontan circulation are included in this master thesis project (see Table 2.1). MRI patient data was selected from a cross-sectional research study, the TOP-FLOW project executed by the Leiden University Medical Centre. The included patients have an age ranging from 11.9 to 27.3 years and underwent the Fontan procedure at an age between 2.0 to 7.4 years old. During the Fontan procedure, either a 16, 18 or 20mm extracardiac conduit, made of ePTFE, was implanted in these patients.

Table 2.1: Patient characteristics

N	19	
Gender (male/female)	9/10	
Age (y)	16.6 ± 3.7	[11.9 – 27.3]
Age at Fontan (y)	3.4 ± 1.3	[2.0 – 7.4]
BSA (m^2)	1.66 ± 0.18	[1.33 – 2.01]
Average Tunnel Flow (L/min)	3.4 ± 0.9	[2.1 – 4.9]
N - 16mm	8	
N - 18mm	6	
N - 20mm	5	

mean ± SD [min-max]

In order to answer the research question in this master thesis, the patients were selected differently for each part. For the first part, fifteen patients were selected based on the implanted conduit size (16, 18 and 20 mm) and average flow in the conduit, i.e. tunnel flow, measured with real-time MRI. These patients are divided into three groups with different conduit size but approximately equal average tunnel flow.

For the second part, ten patients were selected based on the implanted conduit size (16 and 18 mm) and increasing BSA. Since no follow-up data were available, increasing BSA was used as a measure of "anatomical age" as an alternative for measuring one patient multiple times over time. This selection procedure makes it possible to indirectly analyse the effect of body growth on the performance of a specific conduit size.

2.2. Technical Background

This section gives a brief explanation of the theories behind two applied technologies, Computational Fluid Dynamics, to simulate the blood flow in the ECTC and Magnetic Resonance Imaging with which the patient's geometry and blood flow data is obtained.

2.2.1. Computational Fluid Dynamics

The main principle of CFD is to model moving fluid, i.e. fluid flow. Fluid flow is characterised by three general equations: the momentum equation, the continuity equation and the energy equation. These are better known as the law of the conservation of mass, the law of motion and the law of conservation of energy, all applied to fluids. These three principles are included in the Navier-Stokes equations, describing the relationship between velocity, pressure, density and temperature of the fluid flow [41]. In this study the fluid of which the flow was simulated is blood. In order to simulate blood, it was considered as an incompressible fluid with a constant density independent from pressure changes. Furthermore, it is important to realise that blood is a non-Newtonian fluid due to its consistence of three parts: red blood cells, white blood cells and platelets, and plasma. Newtonian fluids are characterized by a viscosity (i.e. the ratio between shear stress and shear rate) that is independent of shear rate. These fluids display a linear relation between shear stress and shear rate [42]. Since blood has the properties of a non-Newtonian fluid it is often defined in a Carreau fluid model. This model accounts for the non-Newtonian shear-thinning properties of blood, meaning that its viscosity is lower at higher shear rates, without having to model blood as a three-phase system which is complicated and computationally intensive [41]. The equation of the Carreau fluid model is defined in Eq. 2.1.

$$\eta_{eff}(\dot{\gamma}) = \eta_{\infty} + (\eta_0 - \eta_{\infty})\left(1 + (\lambda\dot{\gamma})^2\right)^{\frac{n-1}{2}} \tag{2.1}$$

Where $\dot{\gamma}$ represents the shear rate, η_{eff} the fluid viscosity depending on the shear rate, η_{∞} the viscosity at high shear rate, η_0 the viscosity at zero shear rate, λ the relaxation time and n the power index.

Taking these blood characteristics into account, the Navier-Stokes equations for blood with a constant density and variable viscosity described using the Carreau fluid model is described in Eq. 2.2 and is coupled to the continuity equation (Eq. 2.3).

$$\rho\left[\frac{\partial u}{\partial t} + (u \cdot \nabla)u)\right] = \nabla\left[-p\mathbb{I} + \eta_{eff}(\nabla u + (\nabla u)^T)\right] \tag{2.2}$$

$$\nabla \cdot \vec{u} = 0 \tag{2.3}$$

With u representing the velocity, ρ the density, η_{eff} the fluid viscosity depending on the shear rate by Carreau's model, p the fluid pressure and t the time.

Finding an exact solution, analytically, of these equations can only be achieved for relatively simple fluid cases. However, the blood flow in the ECTC is rather complicated. Therefore, these equations are numerically solved in this study using the Finite Volume Method. In this method, the entire geometry is divided into smaller control volumes, also known as cells. These cells together form the so-called mesh. The Navier-Stokes equations (Eq. 2.2) can then be discretised into multiple sets of algebraic equations for all cells apart. These algebraic equations enable calculations of velocity and pressure at the centre of a cell, based on the previously calculated values of the neighbouring cells. The higher-order used for these discrete algebraic equations, the more values of neighbouring cells are considered for the new value calculation of that particular cell. The resulting equations of all cells are added together in a large matrix. Iteratively this matrix is solved per time step. Selecting the time step is important while solving these equations numerically; a smaller time step will result in a smaller absolute error between the numerical solution and the exact solution. However, the smaller the time step size, the longer the computing time. Selecting a sufficient time step size can be done with the help of the Courant-Friedrichs-Lewy (CFL) condition [43]. The CFL condition determines the time step size using the mesh size and the velocity magnitude of the flow, and is calculated as follows:

$$CFL = \frac{v * \Delta t}{\Delta x} \leq 1 \tag{2.4}$$

Where v is the velocity magnitude, Δt is the time step size and Δx the control volume size.

The computational time of solving these equations is, besides the time step size, depending on the order used for the discrete algebraic equations, the number of cells into which the geometry is divided (i.e. mesh resolution) and the number of time steps for which it needs to be solved. It is important to make a considerable trade-off between computing time, spatial and temporal resolution appropriate to the purpose of the simulations. The CFD solver used in this project, is ANSYS Fluent (v19.3, ANSYS, Inc.).

In order to create a CFD model to simulate the blood flow through the ECTC geometry. Two main components are needed, 1) a patient-specific 3D geometry of the ECTC and 2) flow data as boundary conditions. Boundary conditions are constraints set to the flow inlets, flow outlets and wall in order to solve the simulation. The pipeline of the whole CFD modelling process is given in Fig. 2.1 and is divided in pre-processing, processing and post-processing. The top half of the figure represents the obtainment of the flow boundary conditions and the bottom half the obtainment of the ECTC geometry model. The individual steps are explained and their implantation described, for modelling the blood flow in the ECTC, in the upcoming sections of this chapter.

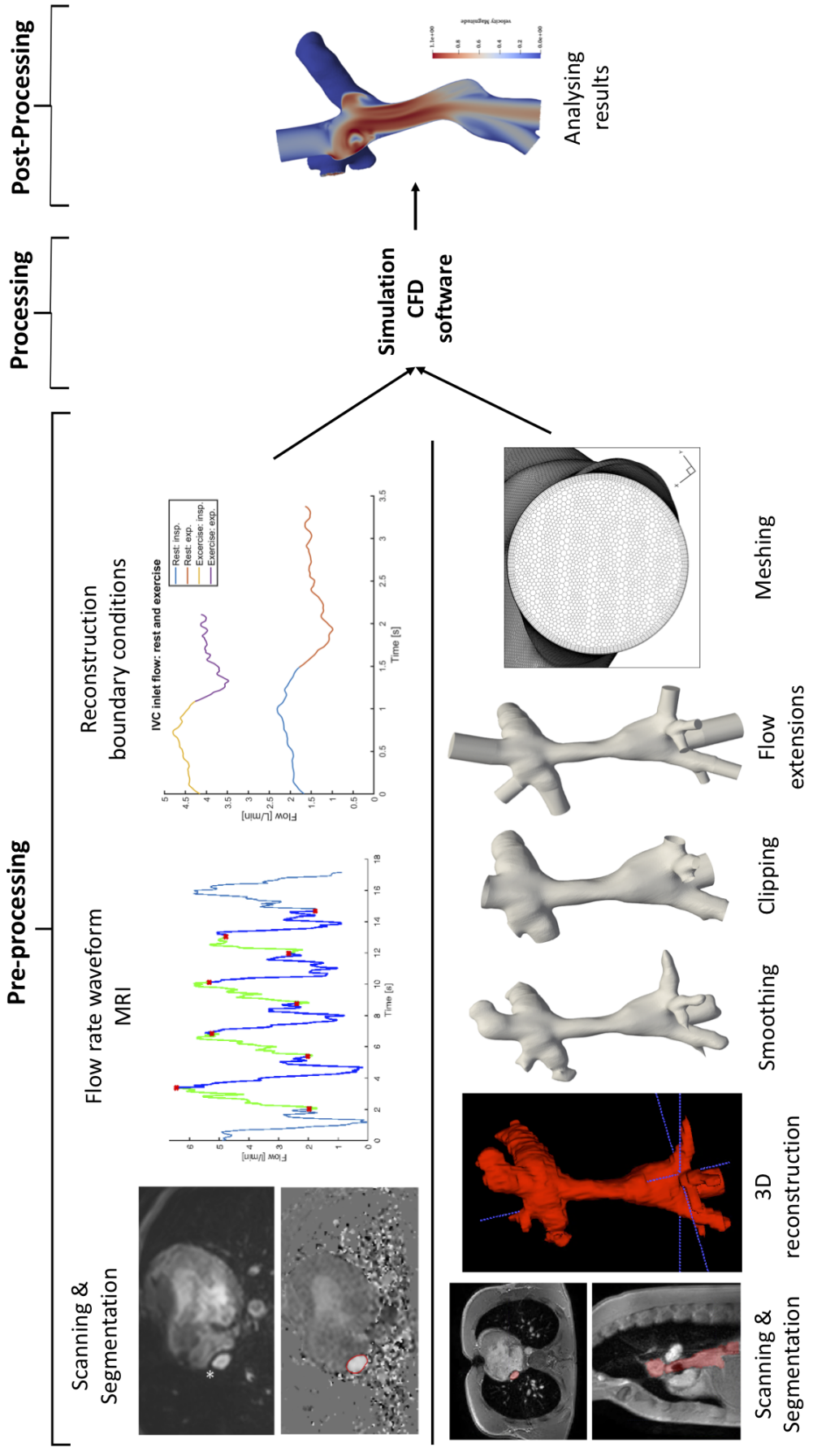

Figure 2.1: CFD pipeline subdivided in pre-processing, processing and post-processing.

2.2.2. Magnetic Resonance Imaging

MRI provides detailed images of tissues and organs by making use of the fact that these tissues and organs contain hydrogen atoms, also called protons. Normally these protons move in a random direction (Fig. 2.2 box 1). However, when a strong magnetic field is created by an MRI scanner, around the area of the body to be scanned, the nuclei of the protons react by aligning with the magnetic field (Fig. 2.2 box 2). Thereafter the MRI scanner directs a radio frequency (RF) pulse through a certain area of the body forcing the proton nuclei out of alignment with the strong magnetic field and inducing a spin of the protons, causing some protons to absorb energy (Fig. 2.2 box 3). When the RF pulse is turned off, the stored energy is released from the body by radio waves, which are detected as an electrical current by receivers in the MRI scanner (Fig. 2.2 box 4). Because protons in different kinds of tissues release different amounts of energy, a distinction in tissues can be made [44].

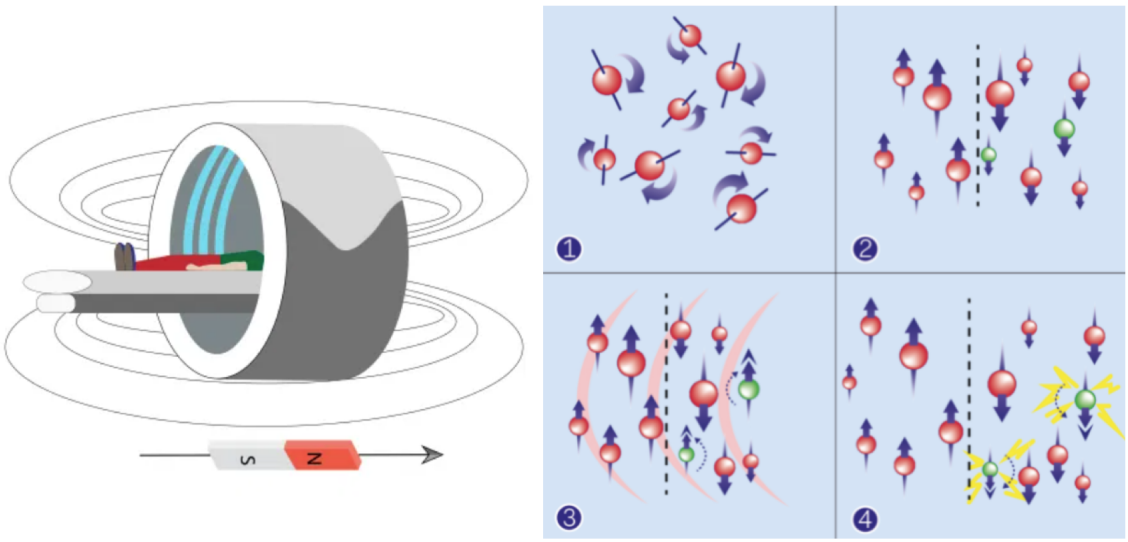

Figure 2.2: Left: MRI scanner including the magnatic field [45]. Right: Schematically overview of the MRI acquisition sequence at proton level [46].

From voxels, which are a volume elements containing millions of protons, the final MRI signal is extracted via a computer using a Fourier transformation. The resulting MRI signal consists of a magnitude and a direction (i.e. phase). Static MRI uses only the magnitude of the signal from which an image in pixels can be obtained, whereas a special form of MRI, Phase-Contrast MRI (PC-MRI), uses both the magnitude and the phase of a voxel. With the inclusion of the phase in PC-MRI, the velocity of moving fluid (i.e. blood flow) can be extracted from the MRI signal by the proton's phase-shift proportional to its velocity when placed in a strong magnetic field. These phase shifts can be transformed in PC velocity images, from which blood flow rates can be quantified [44].

Three types of MRI are used in this project using a Philips Ingenia 3.0 Tesla MR system. First, a 3D geometrical model of the patient's ECTC anatomy was obtained from static 2D MRI images. Second, the patient's blood flow data of the ECTC inlet and outlet vessels was extracted from free-breathing non-ECG gated 2D PC-MRI (i.e. real-time MRI) and ECG-gated 2D-3dir PC-MRI. The derivation of the 3D geometrical model from the 2D MRI images is further described in section 2.3.1. The principals of the used types of PC-MRI is explained here.

Free-breathing non-ECG gated 2D PC-MRI (i.e. real-time MRI) Real-time MRI uses thin slices containing voxels (see Fig. 2.3), in which the velocity of the blood flow is encoded in only one direction. The plane of the slices is placed perpendicular to the imaged blood vessels so that the velocity, encoded in a through-plane direction, is in the same direction as the blood flow. Furthermore, at the expense of a potentially higher risk of motion artefacts, since no gating is used for cardiac and respiratory motion, the cardiac and respiratory effects (due to free breathing) on blood flow are present in the obtained MRI signal. Although it is the in-

tention that the respiration effects on the blood flow are included, the motion artefacts are not wanted since they influence the quality of the MRI. However, since the MRI technique allowed for 15 images per second, the artefacts due to respiratory motion is reduced. The final used slice thickness is 5 mm, the in-plane spatial resolution is 2.5x2.5 mm and the temporal resolution is 67.0 ms. An example of real-time MRI in the ECTC with the resulting flow-rate waveform over time is displayed in Fig. 2.4.

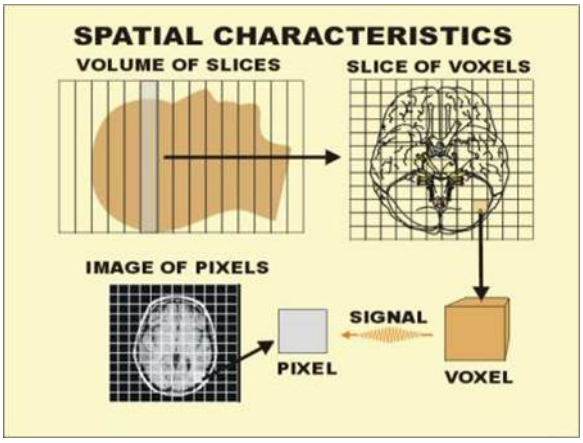

Figure 2.3: Spatial characteristic of MRI imaging [47].

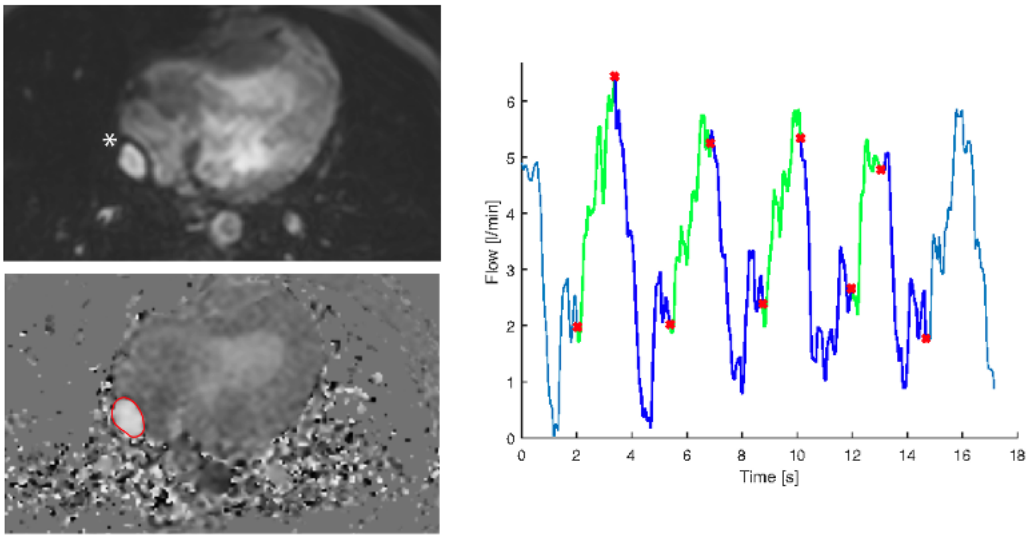

Figure 2.4: Left: Slice of the real-time MRI with contouring the Extracardiac Conduit. Right: The flow-rate waveform obtained from the real-time MRI signal.

ECG-gated 2D-3dir PC-MRI It was proposed to have all blood flow velocities measured with real-time MRI. However, due to technical issues this was not succeeded. Therefore, also another type of MRI is used in this study: ECG-gated 2D-3dir PC-MRI. 2D-3dir PC-MRI uses, like the real-time MRI, thin slices perpendicular to the imaged blood vessels. However, in this type of MRI the velocity is encoded in three directions: one through plane direction and two in-plane directions. Although three directions are encoded, in this study only the through plane direction was used which is in the same direction as the blood flow. Furthermore, with this type of MRI electrocardiogram (ECG) gating is used to avoid cardiac motion artefacts. This type of gating is done with continuous data acquirement over the full cardiac cycle for multiple heartbeats. The obtained data is afterwards synchronized and averaged to a velocity dataset including one cardiac cycle, resulting in fewer artefacts. However, a major drawback is that with the use of ECG gating the respiratory effects on the blood flow will be averaged and therefore only the cardiac effect on the blood flow is considered [48]. The

final used slice thickness is 5 mm, the in-plane spatial resolution is 1.5x1.5 and the temporal resolution is 41.0 m.

2.3. Pre-processing

In order to be able to do a performance analysis of the different sized conduits in the Fontan circulation, first, computational fluid dynamics was used to simulate the blood flow through the patient's the ECTC. Three essential components are required to perform the CFD simulations: geometry, boundary conditions and material properties. The pre-processing steps to obtain these components and several relevant additional simulation settings are discussed in this section.

2.3.1. Anatomical geometry

The first essential component required to perform CFD simulations is the geometry. Although the geometries for this project were previously obtained by the research group, a brief description is given here.

In order to create a 3D model of the patients' Fontan circulation, first, static 2D MR images were obtained. More specifically, in 2D static MRI, slices of 5 mm thick (with 2.5 mm overlap) in the transverse and sagittal plane were created from which images could be obtained of the relevant tissue (see left in Fig. 2.5). To create a 3D geometrical model from these images, several steps were performed. The first step was rigid registration; this makes sure the 2D static MR images of the different planes are in spatial alignment. Second, interpolation was done to obtain isotropic voxels, making sure the in-plane and out-of-plane resolution is equal. Then, using the tool of open-source software ITK-SNAP [49] segmentation was done by colouring the desired geometry, here the ECTC, manually in each slice (see left in Fig. 2.5). The geometry after segmentation includes the IVC below the hepatic veins, the hepatic veins, the Fontan tunnel, the SVC, the left and right pulmonary arteries and, the upper lobe side-branches of the right pulmonary artery. This geometry was reconstructed to a 3D model of the Fontan anatomy in a standard triangle language (STL) format (see middle Fig. 2.5). The resulting 3D Fontan model was smoothed and centrelines were obtained for every vessel using the Vascular Modelling Toolkit (VMTK) [50]. An example of such a smoothed 3D reconstruction is displayed on the right in Fig. 2.5.

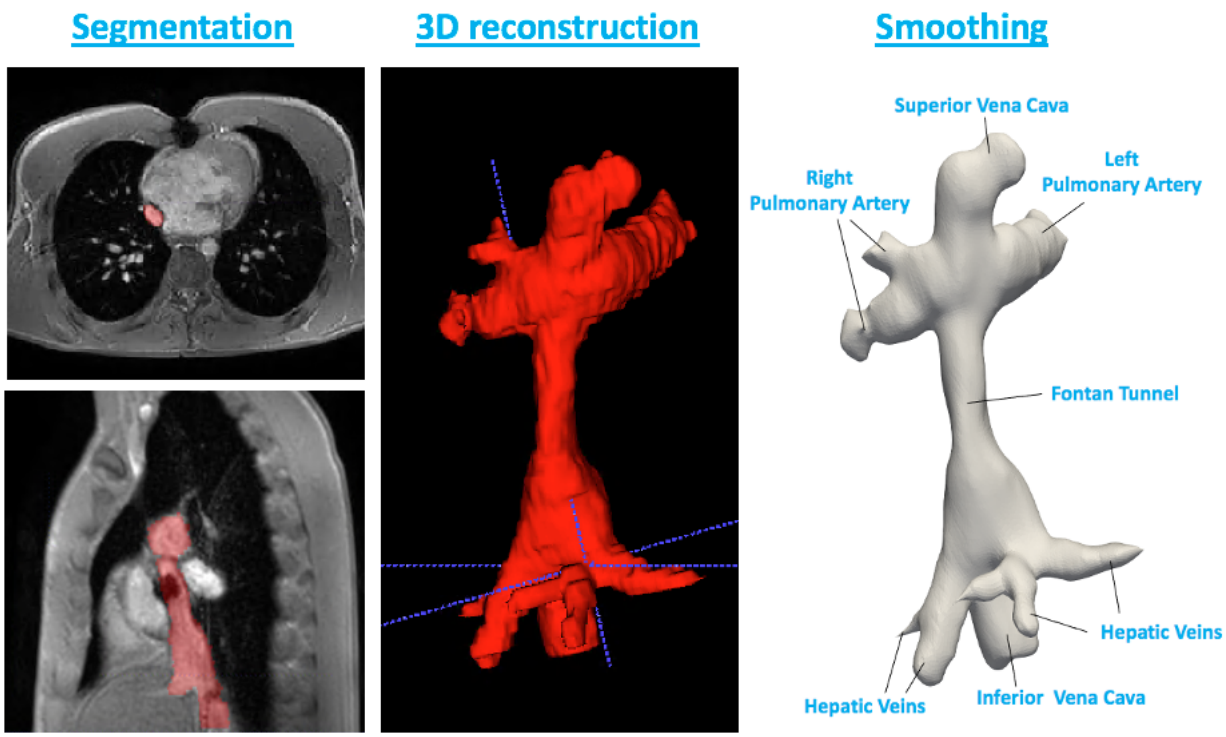

Figure 2.5: Left: Segmentation in the transverse (top) and sagittal (bottom) planes. Middle: 3D reconstruction of the segmented ECTC geometry. Right: Smoothed 3D ECTC geometry model.

The smoothed 3D geometry model is not yet ready for the CFD simulation. In order to be able to apply the flow boundary conditions to the model, the vessel endings should be circular. Furthermore, when blood flow is simulated through the 3D geometry model, the incoming flow first needs to develop before entering the actual geometry. To allow for the assignment of the flow to the inlets and flow development, all the vessel endings of the model were clipped perpendicular to the vessel centreline (see the model in the middle in Fig. 2.6), and cylindric flow extensions were added to the geometry (3x vessel diameter) (see the model at the right in Fig. 2.6). The clipped 3D geometries models of all included patients in this study can be found in Appendix B.1, B.2 and B.3. Lastly, the 3D geometry model needs to be meshed in order to solve the equations used in the numerical Finite Volume Method during the CFD simulations. Therefore, an unstructured polyhedral mesh with four layers of boundary mesh (prism layers) was built using ANSYS-ICEM and ANSYS-Fluent [51]. The mesh cell size was calculated by the average diameter of the inlet and outlet vessels divided by 40 [51]. The resulting mesh cell size ranges between 0.4 and 0.5 mm (see Fig. 2.7), and its performance was checked by the research group during an earlier investigation using a mesh independence study (see Appendix C).

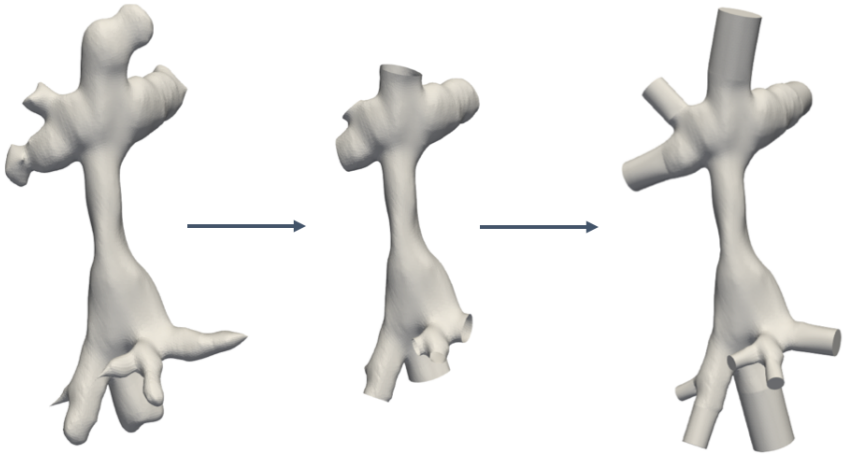

Figure 2.6: Anatomical geometry ECTC. Left: Smoothed 3D geometry model obtained from MRI. Middle: Clipped 3D geometry model. Right: 3D geometry model with added flow extensions.

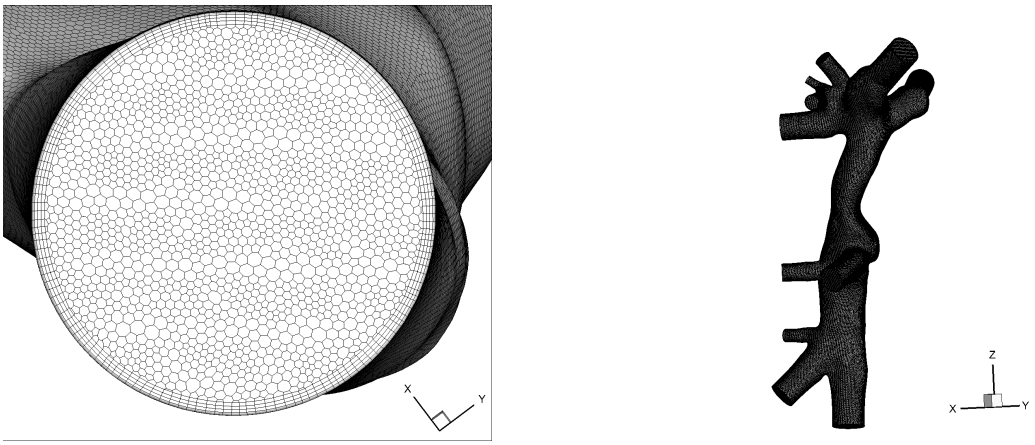

Figure 2.7: Polyhedral mesh. Left: Inlet surface of the Inferior Vena Cava; including boundary layer. Right: Complete ECTC geometry.

2.3.2. Boundary conditions

The second essential component is the boundary conditions. With boundary conditions, the patients' measured blood flow is implemented into the CFD simulations. The blood flow at the inlets (IVC, HVs and SVC) and outlets (left and right pulmonary arteries) was obtained from MRI data, acquired previously by the research group (see Fig. 2.8). The procedures for obtaining the inlet and outlet boundary conditions will be separately explained in this section.

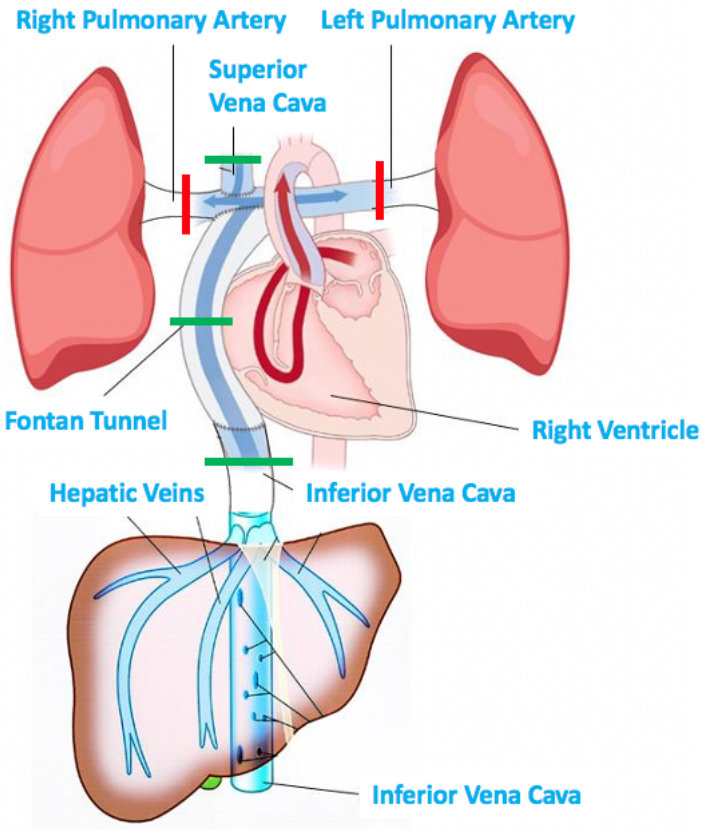

Figure 2.8: Locations of the slices from where the flow is obtained with MRI. Green stripes correspond to the locations acquired using real-time MRI and red stripes to the locations acquired with ECG-gated 2D-3dir PC-MRI.

Inlet boundary conditions For the inlet boundary conditions, time-varying blood flow rate waveforms, in a resting condition, were acquired from real-time PC-MRI (free-breathing, non-ECG gated 2D PC-MRI) velocity data. More specifically, slices perpendicular to the patient's IVC, Fontan tunnel and SVC were used to acquire through-plane velocity profiles. These obtained velocities were integrated over the area to compute time-varying blood vessel flow rates. The total HV flow was measured indirectly by subtracting the IVC flow from the measured tunnel flow, see eq. 2.5.

$$Q_{HV\_total} = Q_{rhv} + Q_{mhv} + Q_{lhv} = Q_{tunnel} - Q_{IVC} \tag{2.5}$$

With Q_{tunnel} and Q_{IVC} representing the measured tunnel and IVC flow accordingly. The remaining flow (Q_{HV_total}) was divided by ratios based on the respective cross-sectional area of the separate HVs (right, middle and left).

Since it was proposed by the literature that respiration has an essential effect on blood flow, the patients' respiration was monitored simultaneously with real-time PC-MRI measurements. Monitoring was done using a respiratory belt placed around the patient's abdomen at the diaphragm level. The belt measures the expansion of the abdomen during free breathing. From the resulting signals (PHILIPS Physlog files) the respiratory waveform with the timing of the inspiration and expiration can be extracted. Consequently, the flow and hemodynamic parameters could be presented as an average over the complete respiration cycle, as well as an average for the inspiration or expiration phase separately.

For an accurate simulation of the blood flow in the ECTC using CFD, it is required that the obtained time-varying flow rate waveforms of the inlet vessels (IVC, SVC and HVs) last the same time and have the same vector length. However, as a consequence of measuring artefacts in the obtained MRI signals these requirements are not fulfilled. Therefore, the waveforms were interpolated and corrected for encountered phase shifts in time to make sure they have the same vector length and last the same time. Furthermore, to analyse

the results in order of respiration phases it is important to have the flow rate waveforms start and end at the same moment in the respiratory cycle and distinguish in inspiration and expiration. To do so, the flow rate waveforms were combined with the acquired respiratory waveform.

Finally, the resulting flow rate waveforms were decomposed into Fourier series and used to scale the parabolic velocity profiles on the inlets [52]. Hybrid initialization in ANSYS Fluent was performed to verify these inlet velocity profiles (see Fig. 2.9). Appendix D.1 includes the used MATLAB (R2019b) script for obtaining the final corrected flow rate waveforms from the raw MRI data and the Fourier series.

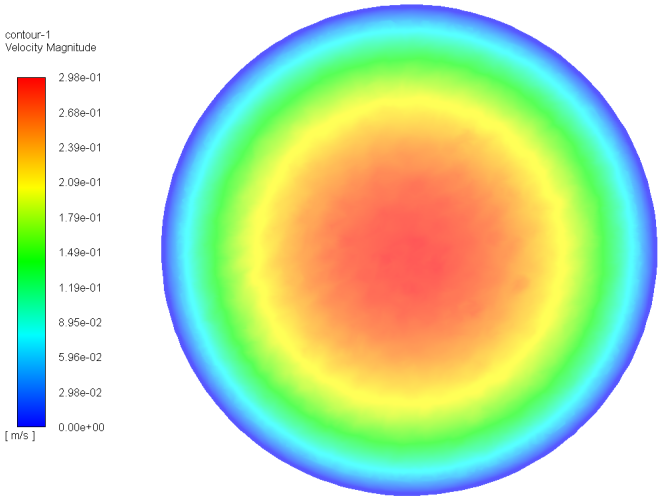

Figure 2.9: Parabolic inlet velocity profile of the IVC. With zero velocity at the blood vessel wall and the highest velocity in the center of the vessel.

Outlet boundary conditions Simulations in CFD need besides inlet boundary conditions also certain boundary conditions for the outlets. The outlets in the case of the ECTC contain the left and right pulmonary arteries (PAs). The outflow boundary conditions on the PAs were imposed as constant outflow ratios. More specifically, the flow entering the ECTC geometry was subdivided over the outlet vessels in a certain consistent ratio. The ratios used were based on the average pulmonary flow distribution to the right and left lung. The pulmonary flow was measured with ECG-gated 2D-3dir PC-MRI, in stead of real-time MRI due to technical issues. If the pulmonary arteries contained side branches, the ratios were further subdivided using the respective cross-sectional area of these branches.

2.3.3. Simulation settings

The main simulation settings are timestep size, the number of timesteps, vessel wall treatment, blood flow properties, solver settings and discretization schemes. The time step size was calculated by dividing the duration of the patient's respiratory cycle by 5,000, fulfilling the CFL condition. To achieve periodic behaviour and exclude start-up effects while simulating, one initial cycle needed to be performed resulting in two respiratory cycles with a total of 10,000 timesteps. Furthermore, the vessel wall was assumed to be rigid, and no-slip conditions were prescribed at the wall. The blood flow was assumed to be laminar and the blood as a non-Newtonian fluid with a density of ρ = 1060 [kg/m3] and modelled using the Carreau model, with the parameters in the model set as follows: $\eta 0$ =0.25 [Pa·s], $\eta \infty$ = 0.0035 [Pa·s], λ = 25 [s] and n = 0.25 [53]. The Semi Implicit Method for Pressure Linked Equations (SIMPLE) algorithm was used for the solver settings. Lastly, the discretization schemes used are Least Square Cell-Based for gradients, a second-order for pressures, a second-order upwind for momentum and a second-order implicit time integration scheme to solve the equations iteratively at each time step before simulating the next time step. Finally, the convergence criteria for continuity and x-y-z-velocities were set for the first initial 5,000 time steps to 1E-3 and for the second 5,000 time steps to 1E-4. Since only the last 5,000 time steps were used for analysis, a less strict criteria has been used for the first 5,000 to save calculation time.

2.3.4. Exercise condition

Since all real-time PC-MRI measurements are obtained in a resting condition, exercise needed to be modelled by adjusting the original time-varying vessel flow rate waveforms based on findings in the literature. The study of Wei et al. [54] was taken as a guideline for the model's parameters. They used lower leg exercise data obtained with an MRI compatible supine bicycle ergometer. The workload was increased during exercise until the heart rate was reached, corresponding to the heart rate at the ventilatory anaerobic threshold (VAT). The VAT was measured by the V-slope method in a previous metabolic exercise test and corresponds to an exercise level at 50-60% of the maximal oxygen uptake (VO_2 max) [55]. The parameters from the study of Wei et al. [54] that are used for the current study are: shortening of the total respiration cycle time with a factor of 1.6, and an increase in the IVC flow magnitude with a factor of 2.44 (this value was also applied on the HVs) and for the SVC flow a factor of 1.67. Since Wei et al. [54] did not discuss the change in inspiration to total respiration time (i.e. inspiratory fraction) during exercise, this parameter was retrieved from a study by Hjortdal et al. [56]. They found an increase in inspiratory fraction of 1.17, meaning that the ratio inspiration-expiration time increases with exercise.

To implement these parameters, first, the inspiratory fraction in exercise was calculated from the inspiratory fraction of the original flow rate waveform. This inspiratory fraction in rest was multiplied with the found factor of 1.17 [56]. With this new inspiratory fraction, the expiratory fraction in exercise could be calculated by subtracting the inspiratory fraction in exercise from 1. After that, the new time vectors were created with the total time divided by a factor of 1.6. Lastly, the flow was increased by multiplication with the factor that corresponds to the specific vessel. Furthermore, interpolation was used to have the flow rate waveform vectors in exercise containing the same length as the original flow rate waveforms. As a consequence the absolute time between data points (time step size) became smaller for the exercise condition compared to the resting condition. The original and resulting adjusted flow rate waveform of a patient's IVC are shown in Fig. 2.10. Appendix D.1 includes the used MATLAB (R2019b) script for obtaining the flow rate waveforms and the Fourier series in exercise condition.

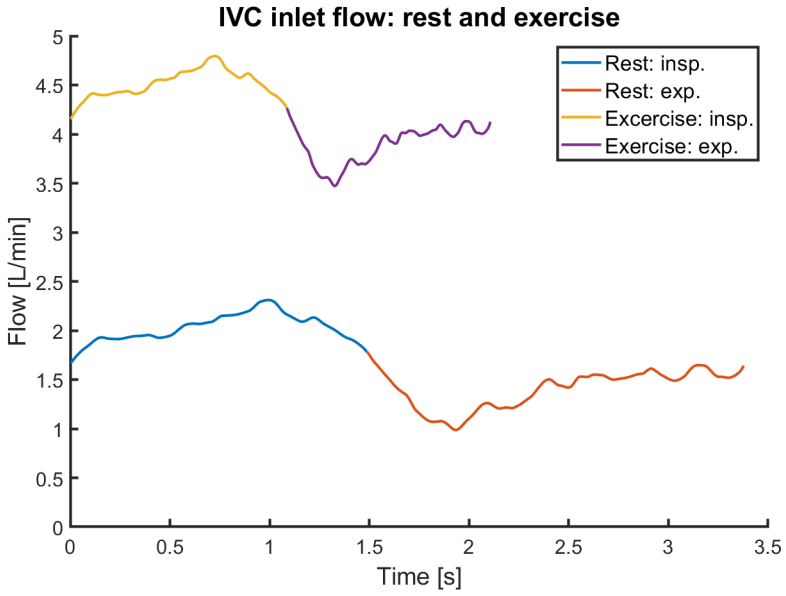

Figure 2.10: The inlet flow is represented of the Inferior Vena Cava for two physical conditions (rest and exercise) distinguished for the respiration phases (inspiration and expiration).

Finally, the newly created flow rate waveforms, in order to simulate exercise, were decomposed into Fourier series. Together with the recalculated time step size, obtained Fourier series were further implemented in the simulation in the same way as the original resting condition.

2.4. Processing

CFD solver software ANSYS-Fluent (v19.2, ANSYS, Inc) was used to perform the CFD simulations. Blood flow simulations in CFD were performed using the Finite Volume Method. Furthermore, a resting condition and an exercise condition were simulated for every patient. In total, 19 patients were included; therefore, 38 simulations were performed. For every simulation, two respiratory cycles were simulated, consisting of 5,000 timesteps per cycle. Every 10th timestep was saved as a *.dat file, and only the outcomes of the second cycle were used for further analysis, resulting in a total of 500 data points per analyzed parameter over time.

2.5. Post-processing

In this section, the post-processing procedure is described. First, the used CFD model was validated by the calculated averaged outlet flow data, to make sure the data was correctly acquired. Then the outcome parameters are described and derived. Finally, it is discussed how the CFD data was used further in the process, specifically concerning the added flow extensions to the ECTC geometry. The following software packages were used during this post-processing procedure: TecPlot (Tecplot 360 EX 2020 R1, Tecplot Inc.), ParaView 5.7.0 and MATLAB (R2019b).

2.5.1. Validation CFD models

Validation of the CFD model was based on the calculated outlet flow at the LPA (m^3/s), averaged over a complete respiration cycle. The calculated average LPA flow was compared to the raw flow data of the LPA and the corrected and interpolated flow data of the LPA. The raw flow data corresponds to the averaged measured real-time MRI flow data of the inlet vessels, before phase-shift correction and interpolation, multiplied with the LPA outflow ratio. The corrected and interpolated flow data was based on the same averaged value of the measured real-time MRI flow data of the inlets, multiplied with the LPA outflow ratio, but after phase-shift correction and interpolation. In Appendix E.1 an overview is given of the three averaged LPA flows based on the same MRI data used for the validation.

2.5.2. Outcome parameters

The parameters analysed to answer the research question regarding the performance of several conduit sizes were *power loss, pressure drop, normalised resistance* and *blood flow stagnation volume*. The parameters and their calculations are briefly described in this section.

Power Loss It is known from the literature that power loss is a commonly used parameter to quantify the performance of the Fontan circulation [57, 58]. Several studies have identified large power losses (mW) with adverse effects limiting patient's quality of life, such as a decrease in exercise capacity. The power loss depends on the blood flow, with higher blood flows causing greater power losses. An inefficient ECTC geometry is less tolerant of flow increases which may result in for example a decreased capacity for oxygen delivery negatively affecting the patient's exercise capacity [58]. Most commonly, a rather simplified power loss is calculated using the control volume approach (see eq. 2.6) [59]. In this equation the p represents the pressure, ρ the density, Q the volumetric flow rate, and A the area.

$$\dot{E}_{simp} = \sum_{inlets} \left(p + \frac{1}{2}\rho \left[\frac{Q}{A} \right]^2 \right) Q - \sum_{outlets} \left(p + \frac{1}{2}\rho \left[\frac{Q}{A} \right]^2 \right) Q \tag{2.6}$$

However, the quantity used for calculating the power loss (mW) in this master thesis is the viscous dissipation rate (VDR) and is defined in eq. 2.7 [57]. Where μ is the dynamic viscosity and u_x, u_y and u_z are the directional velocities. The main advantage of this quantity over the generally used Control Volume Approach is the ability to specify the location of the highest power losses within the geometry [57]. Specifying the location identifies vulnerable area in the ECTC geometry that limit the efficiency.

$$VDR = \mu \left[2\left(\frac{\partial u_x}{\partial x}\right)^2 + 2\left(\frac{\partial u_y}{\partial y}\right)^2 + 2\left(\frac{\partial u_z}{\partial z}\right)^2 + \left(\frac{\partial u_x}{\partial y} + \frac{\partial u_y}{\partial x}\right)^2 + \left(\frac{\partial u_x}{\partial z} + \frac{\partial u_z}{\partial x}\right)^2 + \left(\frac{\partial u_y}{\partial z} + \frac{\partial u_z}{\partial y}\right)^2 \right] \tag{2.7}$$

Pressure Drop The pressure drop (mmHg) across the geometry (ECTC) is a parameter generally used in clinical settings quantifying the performance of the Fontan circulation [58]. Calculating the pressure drop in

this master thesis is done by a derivation of the power loss and is calculated as the average power loss divided by the total venous systemic blood flow in the ECTC (see Eq. 2.8) [59]. In this equation, the PL is representing the power loss and Q_s the systemic venous flow.

$$\Delta P_{TCPC} = \frac{PL}{Q_s} \tag{2.8}$$

Normalised Resistance A further derivation of the power loss, calculated from the pressure drop, is the normalised resistance. This parameter normalises the pressure drop for the systemic venous flow and body posture using BSA, resulting in the actual resistance of the ECTC geometry. The normalised resistance of the ECTC in Woods Units (WU) (mmHg/min/L/m^2) is used by several previous studies [58–60]. The parameter is calculated by first dividing the pressure drop by the total venous systemic blood flow, resulting in Head Loss [mmHg/L/min] (see Eq. 2.9) followed by normalisation for BSA (see Eq. 2.10).

$$Head\ Loss = \frac{\Delta P_{TCPC}}{Q_s} \tag{2.9}$$

$$Normalised\ Resistance = \frac{Head\ Loss}{BSA} = \frac{\Delta P_{TCPC}}{Q_s/BSA} \tag{2.10}$$

Where ΔP_{TCPC} is the pressure drop, Q_s the systemic flow and BSA the body surface area.

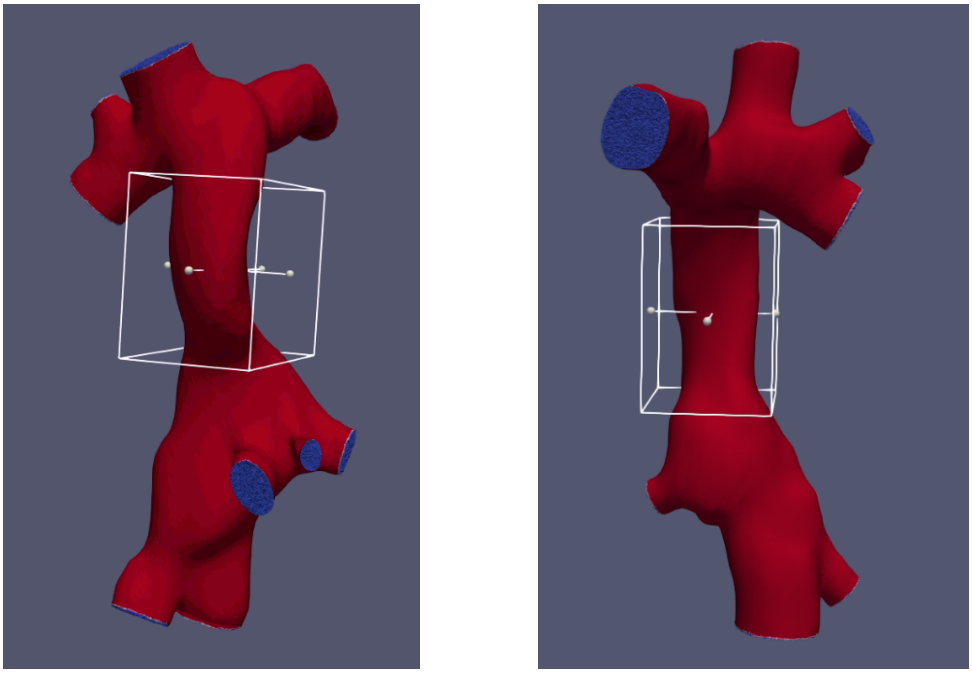

Figure 2.11: The extraction of the Fontan tunnel from the complete ECTC geometry of two patients using box clipping.

Flow Stagnation Volume Thromboembolism is, despite anticoagulation therapy, an important cause of morbidity and mortality in single ventricle patients with a Fontan-circulation and is thought to be related to a gradual increase in pulmonary vascular resistance [61]. 10-35% of the Fontan patients suffer from thromboembolism related to endothelial dysfunction, hypercoagulability and abnormal blood flow such as flow stagnation [62]. Flow stagnation, mostly occurring in oversized conduits, is reported as one of the risks clinicians are dealing with when selecting a suitable conduit size, taking into account the growth potential [33]. The risk for venous thrombosis is mainly described by stagnated blood volumes, where higher stagnated blood volumes increase the risk for thrombosis formation. For this reason, several studies take the blood flow stagnation volume into consideration, where it is quantified as the percentage of blood volume (%) with a velocity lower than 0.01 m/s [33]. However, not only the amount of volume but also the time should be taken into consideration. The period over which venous thrombosis is formed is described in hours or even

days [63]. Thus only regions were the velocities are (almost) permanently below this threshold are of interest. Therefore, in this master thesis, only the minimal stagnation volume is included over a respiratory cycle, assuming that this is the amount of stagnated blood volume permanently present in the ECTC and being at risk for thrombosis formation. Since stagnation volumes are in general inverse with the flow, the minimal stagnation volume is most likely observed as the moment at which the fluid flow is maximal in the ECTC. Calculations are done in ParaView 5.7.0 using the threshold and integrate functions [33]. Additionally, besides the complete ECTC, the minimal flow stagnation volume was also calculated for the Fontan tunnel only. The conduit was extracted with a box clip using ParaView 5.7.0 (Fig. 2.11).

Lastly, since no-slip conditions were assumed in the simulations, all mesh cells at the wall have a velocity of 0.0 m/s. Therefore, the volume was also calculated for the blood volume (%) with a velocity of 0.0m/s. Comparing the flow stagnation volume with the volume for 0.0m/s give insight into the actual amount of stagnated blood volume that is not located at the vessel wall.

2.5.3. Removal flow extensions

Since the added flow extensions are meant to develop the blood flow before entering the actual geometry during the simulation, these flow extensions include redundant data and should not be included in the final analysis. Consequently, it would be ideal to remove the flow extensions before calculating the parameters acquired to analyse the data. Removal of the flow extensions can be done using VTK and VMTK, as these programs can clip 3D geometries with a polyhedral mesh. However, these geometries have a large number of polyhedral cells, making clipping of the flow extensions highly time-demanding. Therefore, it has been carefully considered for which performance parameters clipping was done or not.

First of all, the flow extensions were not removed to analyse the power loss and its related parameters, pressure drop and normalised resistance. This was decided to maintain the ability to analyse the parameters over time. The ability of analysis over time allow distinguishing in respiration phases and calculate average values. However, due to existing energy losses in the flow extensions, it should be kept in mind that the resulting absolute power loss values found will be somewhat higher than is actually the case. The power loss value will increase differently for each case since the diameter and length of the flow extensions are depending on the diameter of the vessels in the ECTC. Nevertheless, since this approach was implemented for all patients, relative comparison between and within patient data will remain accurate to investigate the conduit size performances. To get grip on the amount of overestimating, the power loss was calculated for three patients including and excluding flow extensions at the moment in time at which the power loss was maximal.

Furthermore, for calculating the blood flow stagnation volumes, in the ECTC and tunnel, the flow extensions were clipped. Since only one moment in time was relevant, the minimal flow stagnation volume quantified at the time of maximal fluid flow, clipping could easily be performed for every patient separately. As a result, only the actual geometry was included, and no overestimations of the stagnation volumes are made. Although the inclusion of the flow extensions was not relevant for analysing this parameter in the current project, the flow stagnation volumes in the ECTC were calculated for three patients, including and excluding flow extensions, to get insight into the effect of flow extensions concerning this parameter. This could be relevant for future research purposes in order to analyse the data over time.

2.6. Statistics

In order to answer the research question, several statistics were applied to analyse the outcome data. In general, p-values of <0.05 were considered statistically significant.

Answering the first part of the research question required two types of statistical tests. First, for comparison of the three different conduit sizes (16, 18 and 20 mm,) the data was pre-selected on the basis of the averaged Fontan tunnel flow and was therefore not normally distributed. In order to compare the physical conditions (rest and exercise) and respiratory phases (inspiration and expiration) within the conduit size groups, non-parametric Wilcoxon signed-rank tests were performed for all performance parameters. Second, to compare the three conduit size groups, the Kruskal Wallis test were performed. This is done again for all parameters and including the two physical conditions and respiratory phases.

As for the first part, the patients were pre-selected for the second part of the research question, but on the basis of BSA to simulate growth in the patient group. Therefore, the resulting data was not normally distributed. In order to find an answer for the second part of the research question, Spearman correlations were performed to find whether a significant linear relation exist between the different performance parameters and the BSA. This was done for the two included conduit size groups (16 and 18 mm) separately.

3

Results

This chapter starts off with the results of the patient selection for each part is given. The patient selection is followed up by a general section where the results are given of all the included patients for the different physical conditions (rest and exercise), the two respiration phases (inspiration and expiration) and the relation with body growth. These results allow verifying the relevance of the physical condition, respiration and body growth as proposed in the literature. Finally, the results for the two parts that answer the research question are presented separately. For the general section and the two separate parts, the following performance parameters are discussed: *power loss, pressure drop, normalised resistance, flow stagnation volume in the ECTC* and *flow stagnation volume in the Fontan tunnel.*

3.1. Patient Selection

For answering the research question in this master thesis, the patients were selected differently for each part. For the first part, fifteen patients were selected in total, with five patients per implanted conduit size (16, 18 and 20 mm). The five patients with a certain conduit size were matched to patients with another conduit size based on average tunnel flow measured with real-time MRI (see Fig. 3.1). This resulted in three patient selections with different conduit sizes but an equal distribution of measured tunnel flow (p=0.97). The patient characteristics are given in table 3.1.

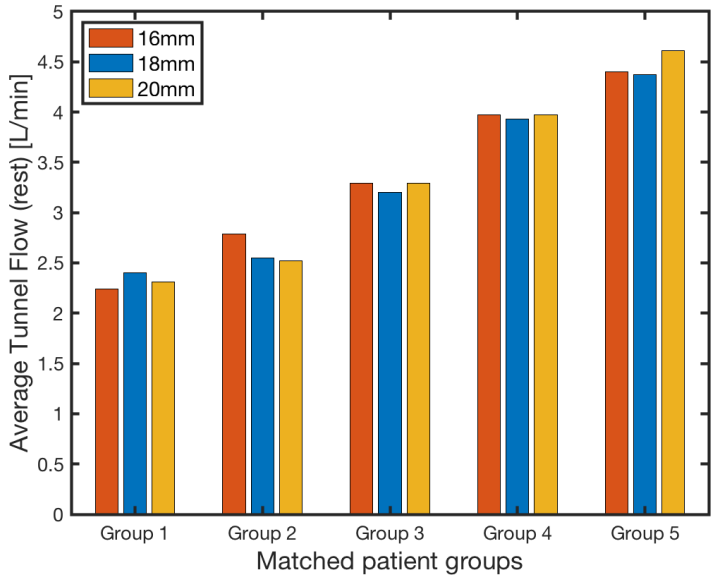

Figure 3.1: The patient selection per conduit size (16, 18 and 20 mm) matched on average Fontan tunnel flow in a resting condition (p=0.97).

Table 3.1: Patient characteristics Part 1 (Median [IQR])

Conduit Size [mm]	**N_{rest}**	**$N_{exercise}$**	**Average Tunnel Flow (Rest)** [L/min]	**Age** [years]
16	5	4	3.29 [1.67]	17.5 [4.2]
18	5	5	3.20 [1.68]	13.8 [1.7]
20	5	5	3.29 [1.88]	17.7 [9.0]

For the second part, ten patients were selected based on the implanted conduit size and BSA. Since there was no real-time MRI follow-up data available, a patient-specific effect of body growth could not be analysed. Therefore, two patient groups were selected with a different conduit size and increasing BSA (see Fig. 3.2). The selection on increasing BSA made it possible to indirectly analyse the effect of body growth on the performance of a specific conduit size. The patient characteristics are given in Table 3.2.

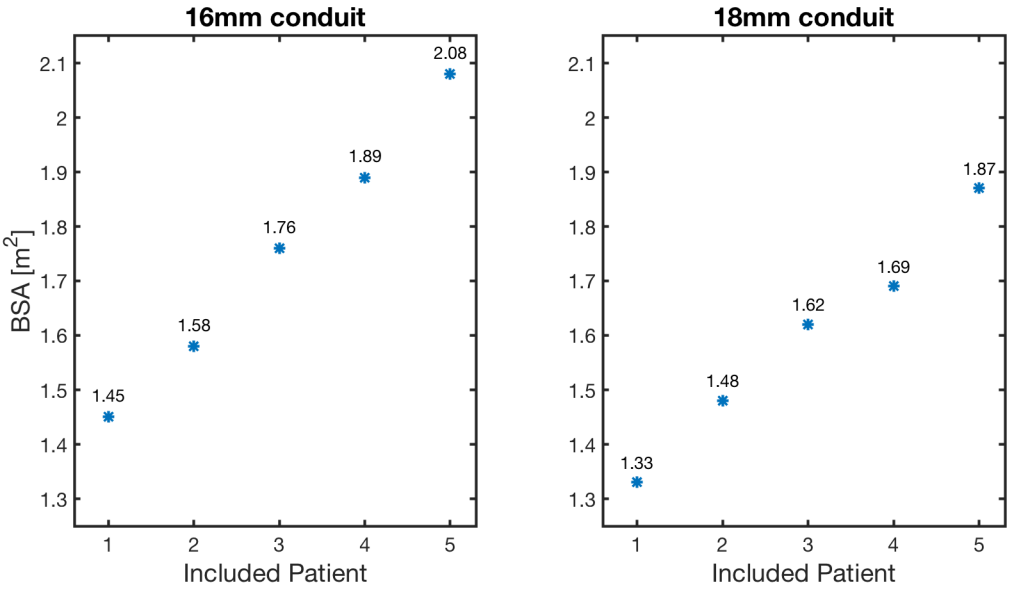

Figure 3.2: The body surface area given for all the patients included in Part 2 in order from smallest to largest in body size. Left: Patients with an implanted conduit size of 16 mm. Right: Patients with an implanted conduit size of 18 mm.

Table 3.2: Patient characteristics Part 2 (Median [IQR])

Conduit Size [mm]	**N_{rest}**	**$N_{exercise}$**	**BSA** [m^2]	**BSA_{min} - BSA_{max}** [m^2]	**Age** [years]
16	5	4	1.76 [0.47]	1.45 - 2.08	17.6 [4.9]
18	5	5	1.62 [0.38]	1.33 - 1.87	13.2 [2.3]

Note that only 19 patients were included in total due to overlapping patients in the two separate parts. Besides, the data of two patients are missing for the exercise condition, therefore only four patients were included in the 16 mm patient group during the analysis of the exercise condition for both parts. Consequently, when considering all patients in the exercise conditions only 17 patients were included. A complete overview of the included patient characteristics is given in Table 3.3, 3.4 and 3.5.

Table 3.3: Characteristics of the patients with an 16 mm conduit implanted.

Pt.	Part	Age [y]	Gender	BSA [m^2]	RT-MRI tunnel flow [L/min]
4	1	17.5	male	1.68	3.29
9	1	18.0	male	1.52	2.79
14	2	15.6	female	1.45	3.64
34	2	17.6	male	2.08	4.87
38	1 & 2	14.4	female	1.58	3.97
39	2	17.6	male	1.89	3.30
42	1 & 2	22.2	female	1.76	4.40
56	1	17.4	female	1.69	2.24

Table 3.4: Characteristics of the patients with an 18 mm conduit implanted.

Pt.	Part	Age [y]	Gender	BSA [m^2]	RT-MRI tunnel flow [L/min]
2	1 & 2	13.2	female	1.69	4.37
7	1 & 2	15.1	female	1.62	3.20
20	1 & 2	14.2	male	1.48	2.55
21	1 & 2	12.7	male	1.87	3.93
50	2	11.9	female	1.33	2.08
51	1	13.8	male	1.41	2.40

Table 3.5: Characteristics of the patients with an 20 mm conduit implanted.

Pt.	Part	Age [y]	Gender	BSA [m^2]	RT-MRI tunnel flow [L/min]
41	1	13.7	female	1.56	3.29
43	1	17.7	male	1.62	2.52
44	1	15.1	female	1.80	2.31
53	1	27.3	female	1.68	3.97
55	1	19.5	male	1.81	4.61

3.2. General results

Before presenting the results answering the research question, several relevant results were retrieved based on the complete cohort (N = 19). From literature, as mentioned earlier, it is proposed that besides the patients ECTC anatomy and conduit size implanted, additional variables play an important role in the performance of the extra cardiac conduit. The four main variables are the average tunnel flow, physical condition (rest and exercise), respiration phases (inspiration and expiration) and body growth. The main results are presented in this section; the exact p-values of the results presented here can be found in Appendix F.1.

Average tunnel flow Since the performance parameters are differently related to the blood flow, it is important to describe this relationship. The resulting correlations between the averaged tunnel flow, obtained with real-time MRI in rest, and the performance parameters are presented here. Significant correlations were found for the power loss ($p<0.01$), pressure drop ($p<0.05$) and flow stagnation volume in the ECTC ($p<0.01$) (see Fig. 3.3). Where a higher tunnel flow result in higher power losses and pressure drops, but in lower flow stagnation volumes. However, no significant correlations were found for the normalised resistance ($p=0.99$) and stagnation volume in the tunnel ($p=0.26$) (see 3.3). Meaning that the amount of average tunnel flow in rest, in this patient population, does not significantly affect the resistance of the ECTC and the flow stagnation volumes in the tunnel.

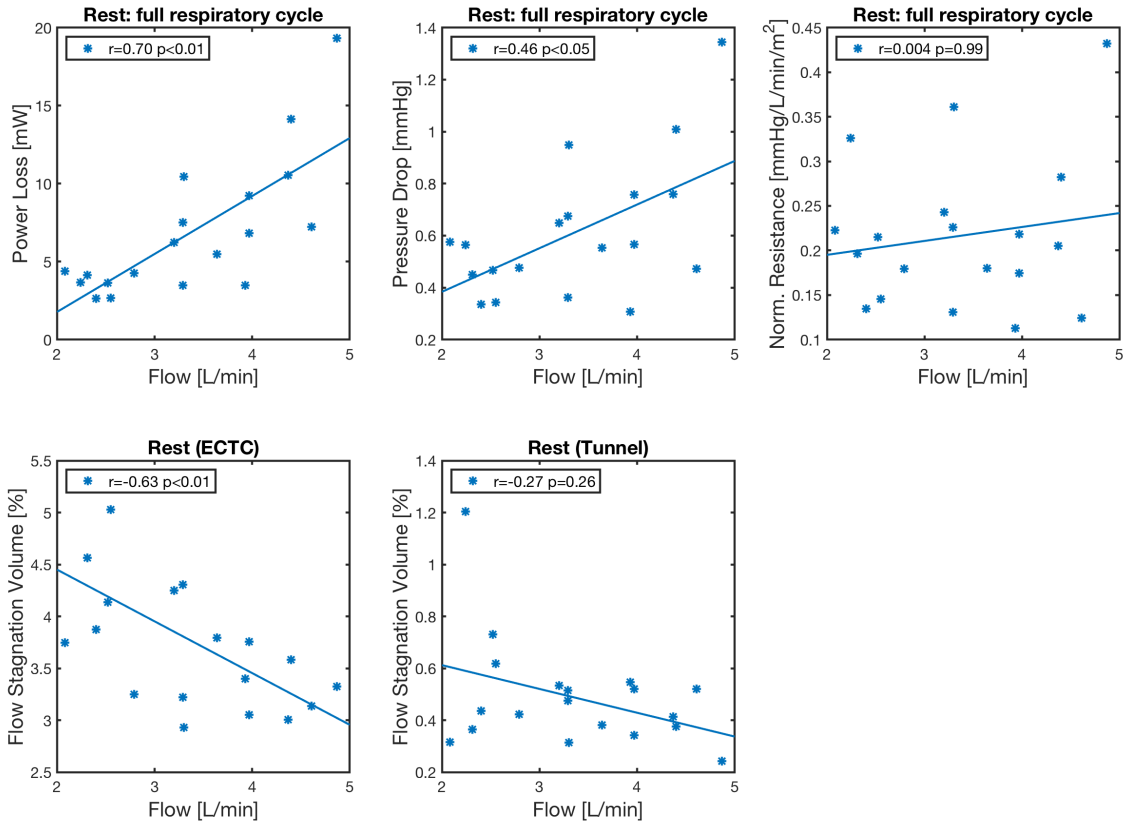

Figure 3.3: The performance parameters related to the averaged real-time tunnel flow [L/min] in a resting condition and for the power loss [mW], pressure drop [mmHg] and normalised resistance [mmHg/L/min/m^2], for the full respiratory cycle.

Physical condition The found results of the performance parameters in Table 3.6 show the relevance of the physical condition. All performance parameters that were computed, show significant differences for a resting and exercise condition. The power loss, pressure drop and normalised resistance increased with exercise compared to the resting condition, whereas the flow stagnation volumes in the ECTC and tunnel decreased with exercise.

Table 3.6: Full respiration cycle, inspiration and expiration in rest and exercise for all included patients.

		Resting Condition				**Exercise Condition**		
Param.	N	Full cyle Median [IQR]	Inspiration Median [IQR]	Expiration Median [IQR]	N	Full cyle Median [IQR]	Inspiration Median [IQR]	Expiration Median [IQR]
PL	19	5.5 [5.6]^{a}	7.2 [6.7]^{ab}	2.3 [3.1]^{ab}	17	37.6 [34.0]^{a}	46.2 [36.2]^{ab}	27.5 [26.6]^{ab}
PD	19	0.56 [0.31]^{a}	0.64 [0.38]^{ab}	0.39 [0.15]^{ab}	17	1.41 [0.94]^{a}	1.55 [0.94]^{ab}	1.24 [0.89]^{ab}
NR	19	0.21 [0.10]^{a}	0.18 [0.09]^{a}	0.24 [0.08]^{a}	17	0.24 [0.09]^{a}	0.19 [0.05]^{a}	0.22 [0.09]^{a}
FS_{ECTC}	19	3.8 [1.0]^{a}	-	-	17	2.9 [0.4]^{a}	-	-
FS_{Tunnel}	19	0.44 [0.17]^{a}	-	-	17	0.44 [0.16]^{a}	-	-

PL is Power Loss [mW]. PD is Pressure Drop [mmHg]. NR is Normalised Resistance [mmHg/L/min/m^2]. FS_{ECTC} is Minimal Flow Stagnation Volume ECTC [%]. FS_{Tunnel} is Minimal Flow Stagnation Volume tunnel [%].^{a} Significant difference (p<0.05) between resting and exercise condition. ^{b} Significant difference (p<0.05) between inspiration and expiration.

Respiration The results for power loss and pressure drop show a significant difference between the two respiration phases (inspiration and expiration), with higher values for the inspiration phase (see Table 3.6). However, no significant difference were found in respiration phases for the calculated normalised resistance. In addition, no distinction is made in respiration for the analyses of the flow stagnation volume since the flow

stagnation volume is only calculated at the moment at which the fluid flow is maximal in the ECTC. For all patients included, this moment takes place in the inspiration phase.

Body growth The association between body growth (i.e. increase in BSA) and performance parameters were studied using correlation measures. From Fig. 3.4 it becomes clear that BSA is significant positively related to the averaged measured Fontan tunnel flow. In other words, patients growing larger will probably have a higher averaged Fontan tunnel flow. Furthermore, concerning the included performance parameters, significant correlations were found between power loss and BSA in both physical conditions and for the different respiration phases (see Table 3.7).

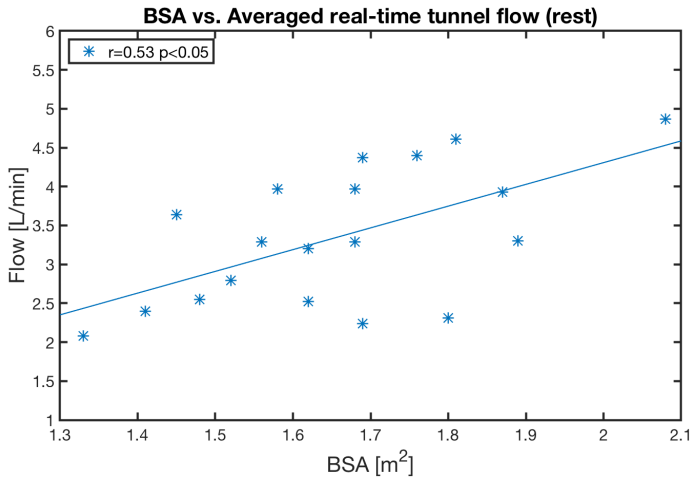

Figure 3.4: Averaged Fontan tunnel flow [L/min], measured in rest with real-time MRI, as function of body surface area [m^2].

Table 3.7: Correlation between BSA and performance parameters: full respiration cycle, inspiration and expiration in rest and exercise for all included patients.

		Resting condition				**Exercise condition**		
Parameter	N	Full cycle r_s	Inspiration r_s	Expiration r_s	N	Full cycle r_s	Inspiration r_s	Expiration r_s
PL	19	0.50*	0.52*	0.38	17	0.57*	0.61**	0.49*
PD	19	0.33	0.39	0.39	17	0.42	0.45	0.43
NR	19	0.29	0.36	0.28	17	0.39	0.42	0.36
FS_{ECTC}	19	-0.35	-	-	17	-0.45	-	-
FS_{Tunnel}	19	-0.16	-	-	17	-0.35	-	-

PL is Power Loss [mW]. PD is Pressure Drop [mmHg]. NR is Normalised Resistance [mmHg/L/min/m^2]. FS_{ECTC} is Minimal Flow Stagnation Volume ECTC [%]. FS_{Tunnel} is Minimal Flow Stagnation Volume tunnel [%]. * Correlation is significant at the 0.05 level. ** Correlation is significant at the 0.01 level.

3.3. Part 1: The performance of three different conduit sizes

This section presents the results for the first part of the research question, where a comparison is made between the performances of the three different implanted conduit sizes (16, 18 & 20 mm). The found results are given for each performance parameter separately. Furthermore, several additional statistics can be found in Appendix F.2.

3.3.1. Power Loss

Prior to presenting the actual results, shortly the results are presented of a small analysis done according to the flow extensions added to the geometry. Since it was decided not to remove the flow extensions while analysing the power losses, to maintain the ability to analyse the parameters over time, the resulting power loss values will be somewhat overestimated. To get a grip on the amount of overestimating, the power loss

was calculated for three patients including and excluding flow extensions at the moment in time at which the power loss was maximal in a resting condition. The results are presented in Table 3.8 and indicate a mean overestimation of approximately 18%.

Table 3.8: Maximal power loss [mW] for three patients in the ECTC including and excluding the flow extensions.

Patient	**Including flow extensions** [mW]	**Excluding flow extensions** [mW]	**Difference** [%]
A	19.8	16.3	-18
B	21.5	18.5	-14
C	17.7	14.0	-21

In Fig. 3.5 and 3.6, the power loss is visualized for two cases; with an implanted conduit size of 18 and 16 mm accordingly. The figures represent the performance at the time of maximum power loss in each respiration phase and the two physical conditions. Several interesting observations can be made regarding these figures. First of all, when comparing both figures it is clear that the 18 mm conduit show less power losses than the 16 mm conduit. Then, when comparing the physical conditions (top row compared to bottom row) it appears that the exercise condition results in higher power losses. Considering the respiration (left figures compared to right figures), the inspiration result in higher power losses compared to the expiration. Furthermore, for both cases, the vulnerable areas for higher power losses are at the locations where flow from different directions converge. More specifically, a large amount of the power losses occurs close to the distal side of the Fontan tunnel, where flow from the IVC and HVs converge, and the areas close to the pulmonary arteries, where flow from the SVC and conduit converge. This observation indicates that the Fontan tunnel plays an important role in the generation of power losses in some way. In Fig. 3.6 representing the 16 mm conduit the transition from the IVC and HVs to the conduit is less smooth than in the figure representing the 18 mm conduit (Fig. 3.5), this is reflected in the power losses occurring already before entering the tunnel.

Then, the results found for the calculated power loss are displayed in Fig. 3.7. In general, from this figure it becomes clear that no significant differences are found between the three conduit sizes. Interestingly, during the exercise condition and inspiration higher power losses are reported for all conduits. In addition, the median and interquartile ranges are reported in Appendix Table F.3 and the exact p-values in Appendix Table F.6 and F.7.

3.3.2. Pressure Drop

The results of the pressure drops are displayed in Fig. 3.8. From this figure, it becomes clear that only for a resting condition in the expiratory phase a significant difference is found between conduit sizes (16 and 18 mm). As found for the power loss, higher pressure drops occur with exercise and inspiration compared to the resting condition and expiration phase. The median and interquartile ranges are reported in Appendix Table F.4 and the exact p-values in Appendix Table F.6 and F.7.

3.3.3. Normalised Resistance

The results of the normalised resistance are displayed in Fig. 3.9. This figure shows significant higher normalised resistances in the 16 mm conduit during the expiratory phase in rest, compared to the 18 mm conduit, and in exercise. compared to the 20 mm conduit. In general, the exercise condition result in higher normalised resistances. However, unlike the power loss and pressure drop, the values for the normalised resistant in inspiration and expiration are comparable. The median and interquartile ranges are reported in Appendix Table F.5 and the exact p-values in Appendix Table F.6 and F.7.

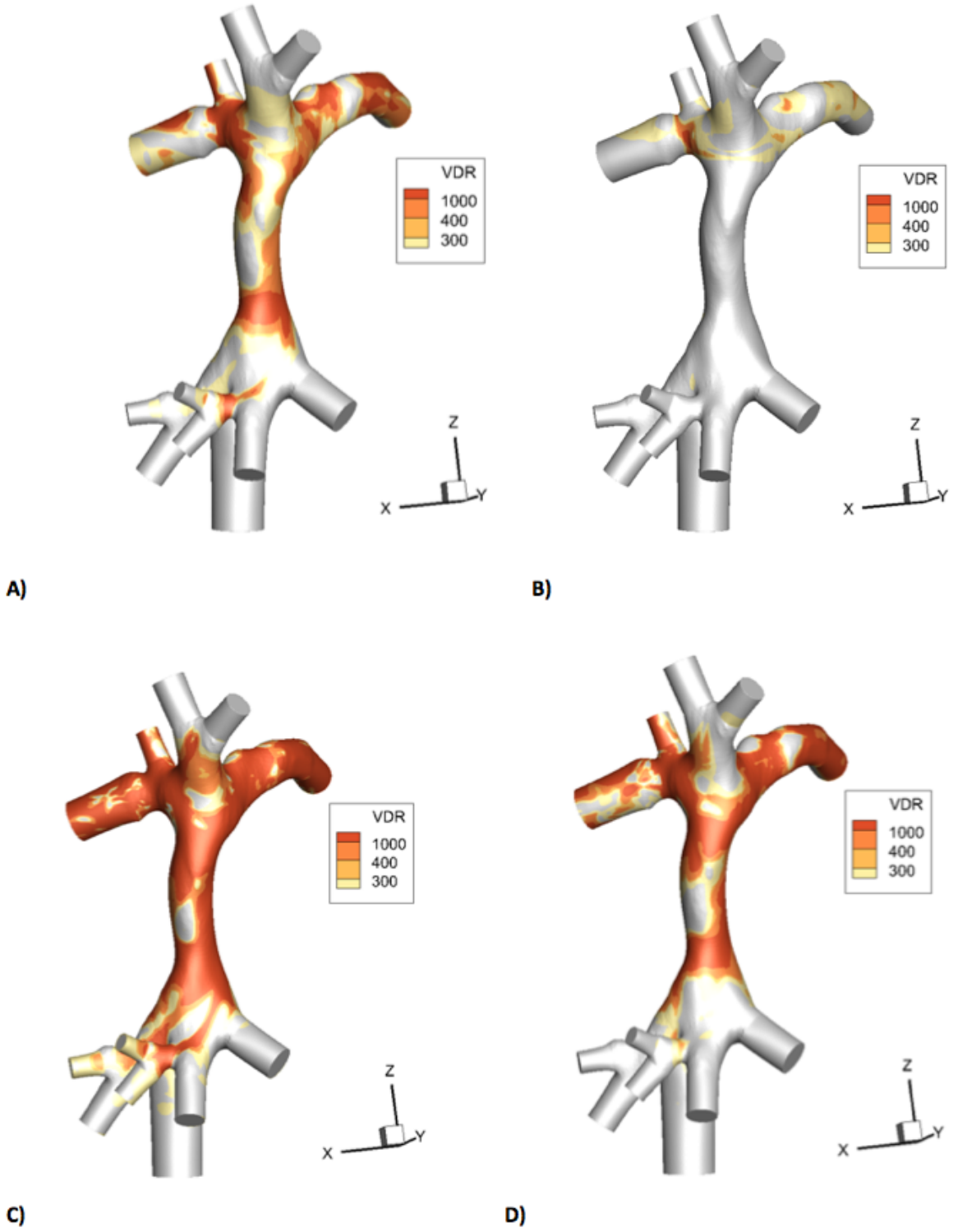

Figure 3.5: Maximal power loss [mW] measured with the Viscous Dissipation Rate (VDR) of a patient with an 18 mm conduit implanted: A) Resting condition - inspiratory phase B) Resting condition - expiratory phase. C) Exercise condition - inspiratory phase. D) Exercise condition - expiratory phase.

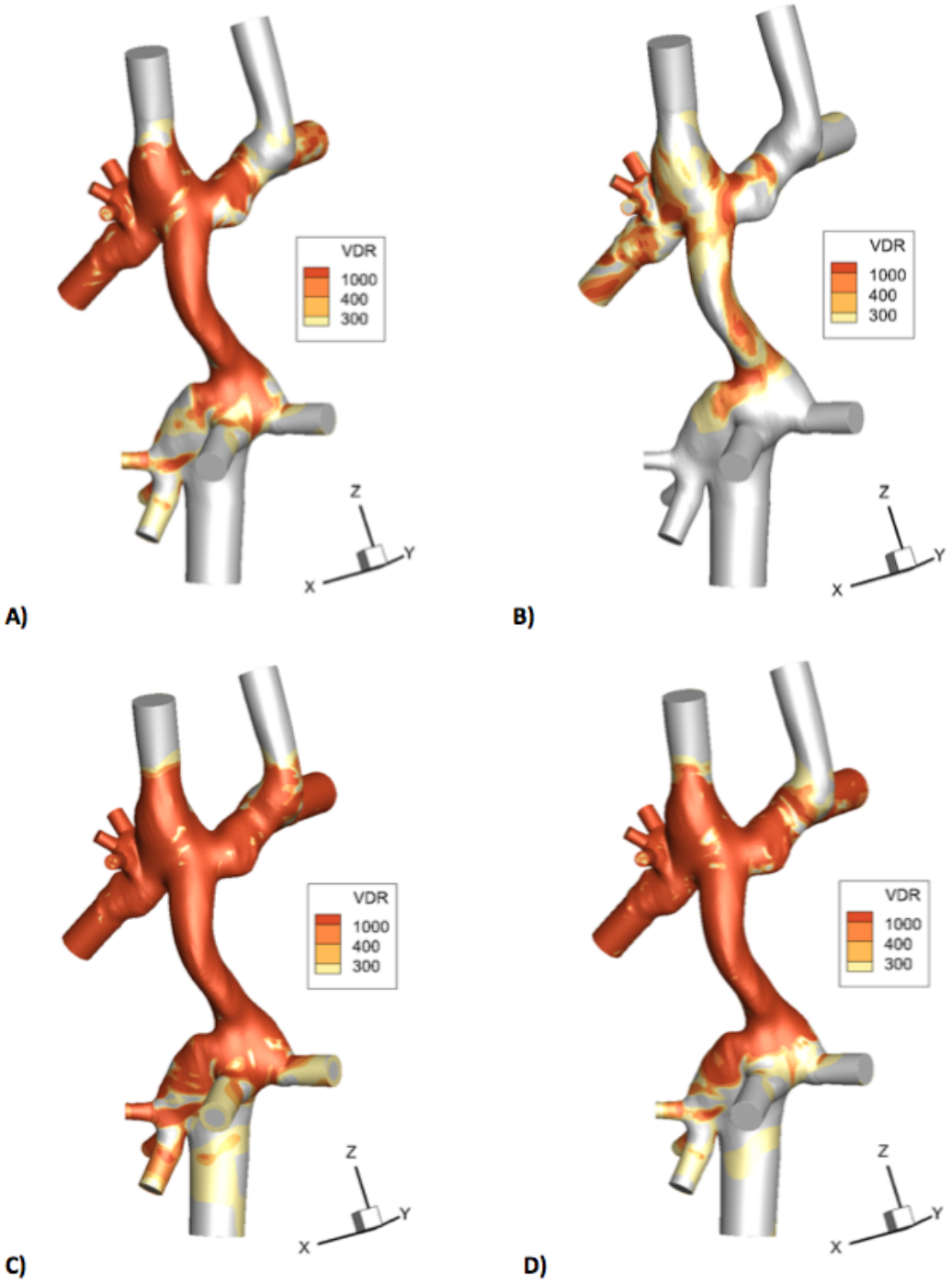

Figure 3.6: Maximal power loss [mW] measured with the Viscous Dissipation Rate (VDR) of a patient with an 16 mm conduit implanted: A) Resting condition - inspiratory phase B) Resting condition - expiratory phase. C) Exercise condition - inspiratory phase. D) Exercise condition - expiratory phase.

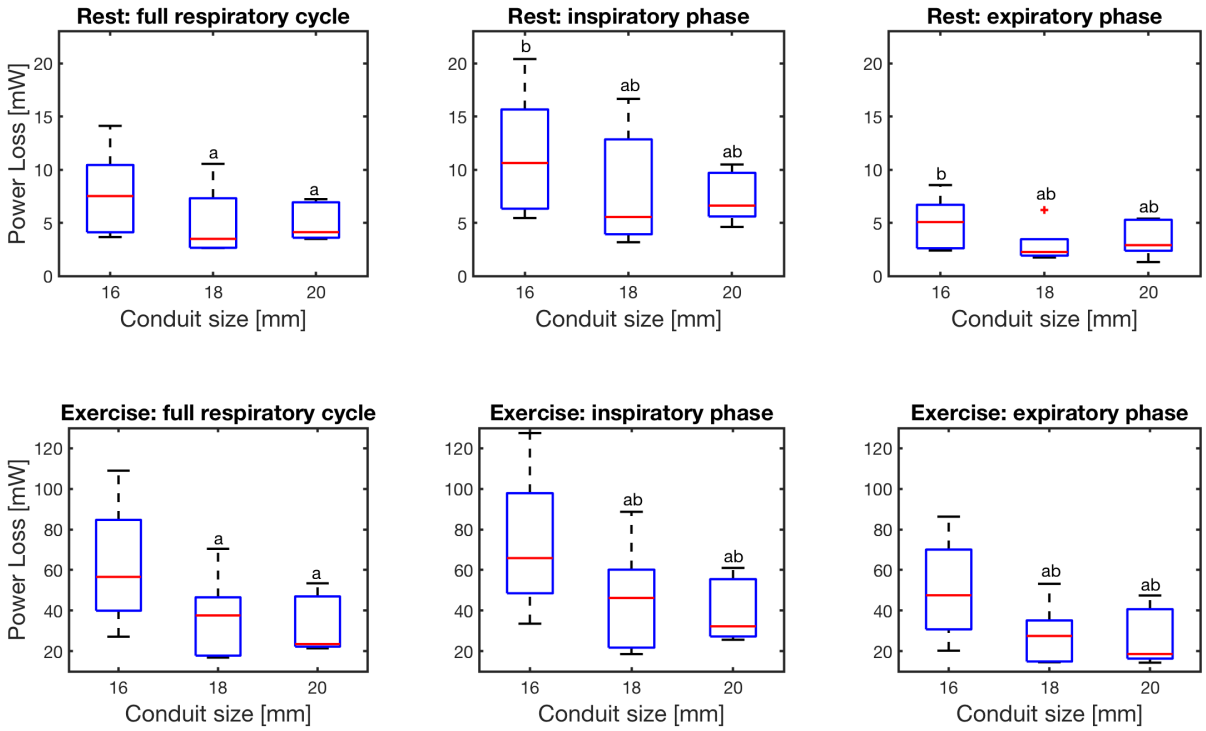

Figure 3.7: Power loss [mW] given for three conduit size groups (16, 18 and 20 mm) in two physical conditions (rest and exercise) for the full respiration cycle, the inspiratory phase and the expiratory phase. *a* Significant different from other physical condition (p<0.05). *b* Significant different from other respiration phase (p<0.05).

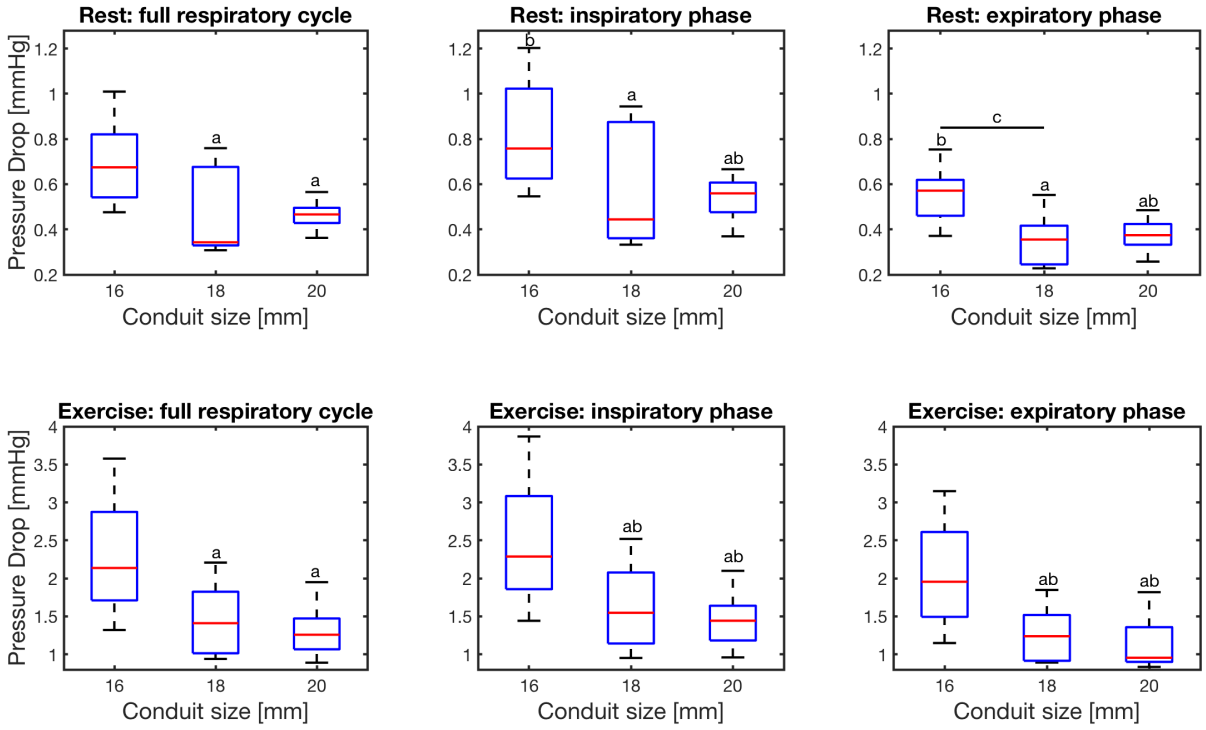

Figure 3.8: Pressure drop [mmHg] given for three conduit size groups (16, 18 and 20 mm) in two physical conditions (rest and exercise) for the full respiration cycle, the inspiratory phase and the expiratory phase. *a* Significant different from other physical condition (p<0.05). *b* Significant different from other respiration phase (p<0.05). *c* Significant difference between 16 and 18 mm groups.

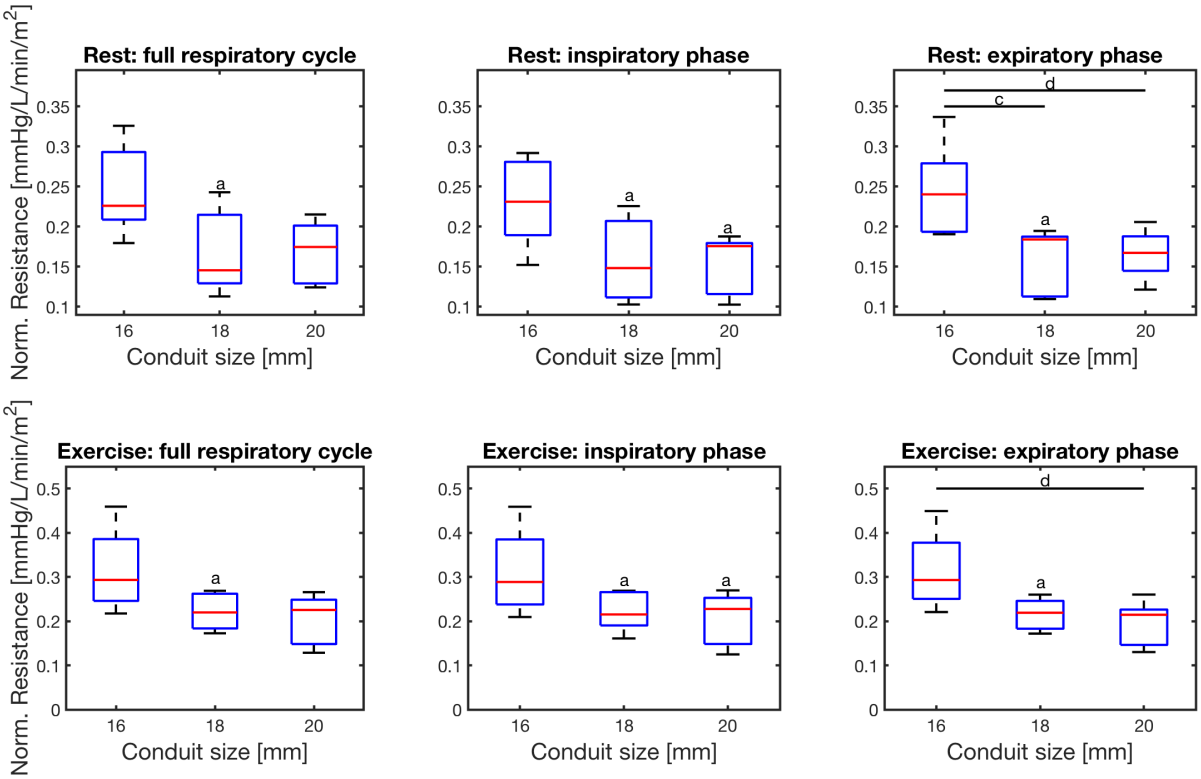

Figure 3.9: Normalised resistance [mmHg/L/min/m^2] given for three conduit size groups (16, 18 and 20 mm) in two physical conditions (rest and exercise) for the full respiration cycle, the inspiratory phase and the expiratory phase. *a* Significant different from other physical condition (p<0.05). *b* Significant different from other respiration phase (p<0.05). *c* Significant difference between 16 and 18 mm groups. *d* Significant difference between 16 and 20 mm groups.

3.3.4. Flow Stagnation Volume

Before presenting the actual results, a small analysis is done according to the flow extensions added to the geometry. Since it is decided to remove the flow extensions while analysing the flow stagnation volumes, the found values will be accurate. However, the ability to analyse the parameters over time got lost. To get insight into the overestimation when the flow extensions would be included the flow stagnation volume is calculated for three patients including and excluding flow extensions when the fluid flow is maximal in a resting condition. The results are presented in Table 3.9 and indicate that a mean overestimation of approximately 4% would be included.

Table 3.9: Blood flow stagnation volume [%] for three patients at maximal fluid flow in the TCPC including and excluding the flow extensions.

Patient	**Including flow extensions** [%]	**Excluding flow extensions** [%]	**Difference** [%]
A	3.3	3.0	-8
B	3.4	3.2	-4
C	4.3	4.1	-3

In Fig. 3.10 and 3.11, the blood flow velocities are displayed for two patients (18 and 16 mm accordingly) in a resting and exercise condition at the time of a maximal fluid flow. These figures show clearly that exercise results in higher velocities compared to the resting condition. Also, it is noticeable that an increase in velocity occurs when the blood flow enters the tunnel. This effect is more present in Fig. 3.11, which include a patient with a 16 mm conduit size, than in Fig. 3.10.

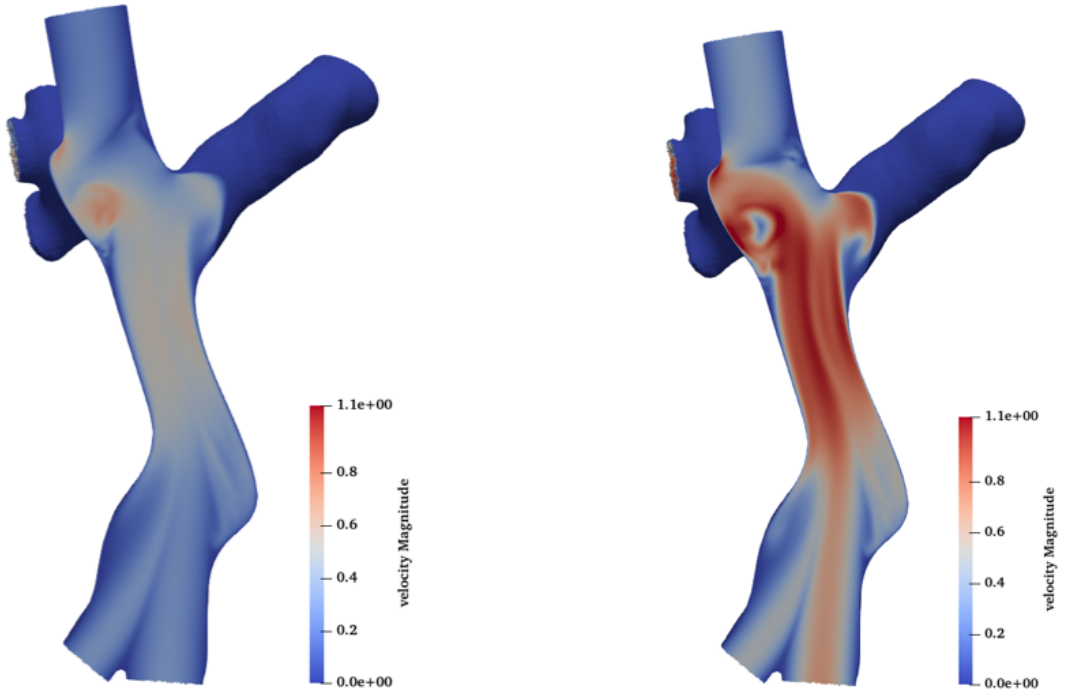

Figure 3.10: Blood flow velocity [m/s] profile of a patient with a 18 mm conduit implanted at maximal fluid flow. Left: resting condition. Right: exercise condition.

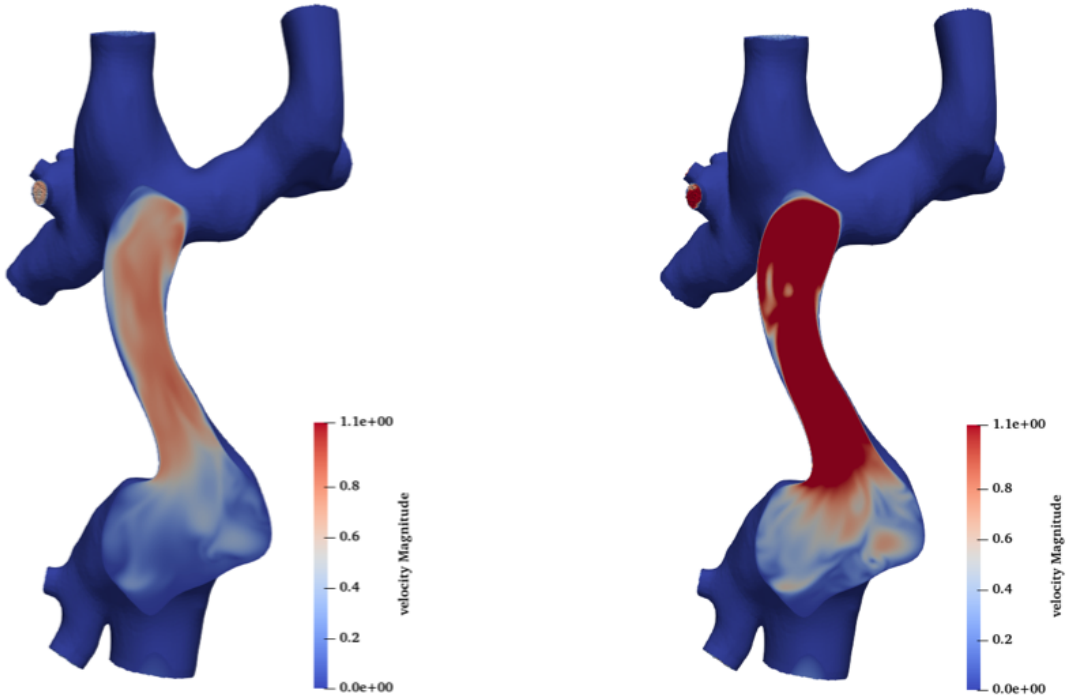

Figure 3.11: Blood flow velocity [m/s] profile of a patient with a 16 mm conduit implanted at maximal fluid flow. Left: resting condition. Right: exercise condition.

Then, in Table 3.10 and 3.11, an overview is given for the results of the flow stagnation volumes at maximal fluid flow in the full ECTC and the Fontan tunnel, for the three groups with different implanted conduit sizes. The flow stagnation volume at maximal fluid flow is assumed to correspond to the minimal flow stagnation volume. The results show that all values are smaller than 5% in the ECTC and approximately 0.5% in the Fontan tunnel. The flow stagnation volume in the ECTC is for the 18 and 20 mm conduits significant higher in a resting condition compared to the exercise condition. Interestingly for the 16 mm conduit this difference did reach statistically significance (p=0.07). Furthermore, no significant differences were found between the three groups (see Appendix Table F.7). In the Fontan tunnel, only for the 20 mm conduit group, a significant difference in stagnation volume at exercise compared to rest could be demonstrated.

Table 3.10: Flow Stagnation Volume at maximal fluid flow in the ECTC (median [IQR]).

Size	N	Blood Volume in ECTC 0.0m/s [%]	Minimal Flow Stagnation ECTC Rest [%]	N	Minimal Flow Stagnation ECTC Exercise [%]
16mm	5	2.6 [0.3]	3.6 [1.3]	4	2.8 [0.3]
18mm	5	2.4 [0.6]	3.9 [1.4][a]	5	2.9 [0.9][a]
20mm	5	2.4 [0.2]	4.1 [1.3][a]	5	3.1 [0.7][a]

[a] Significant difference (p<0.05) between resting and exercise condition.

Table 3.11: Flow Stagnation Volume at maximal fluid flow in the Fontan tunnel (median [IQR]).

Size	N	Blood Volume in Tunnel 0.0m/s [%]	Minimal Flow Stagnation Tunnel Rest [%]	N	Minimal Flow Stagnation Tunnel Exercise [%]
16mm	5	0.42 [0.12]	0.52 [0.46]	4	0.47 [0.14]
18mm	5	0.44 [0.17]	0.53 [0.16]	5	0.47 [0.16]
20mm	5	0.46 [0.26]	0.48 [0.28][a]	5	0.47 [0.25][a]

[a] Significant difference (p<0.05) between resting and exercise condition.

3.4. Part 2: The effect of body growth on the conduit's performance

In this section, the results are presented answering the second part of the research question where the effect of body growth, described in order of BSA, on the conduit's performance is questioned. First, the correlation between BSA and Fontan tunnel flow is analysed, and then the relation between BSA and each performance parameter is presented. Note that this is not done for the patients with a 20 mm conduit implanted. For the 20 mm conduit there were too few patients included in the cohort with a variety in BSA to mimic body growth. Besides the results described here, several additional statistics can be found in Appendix F.3.

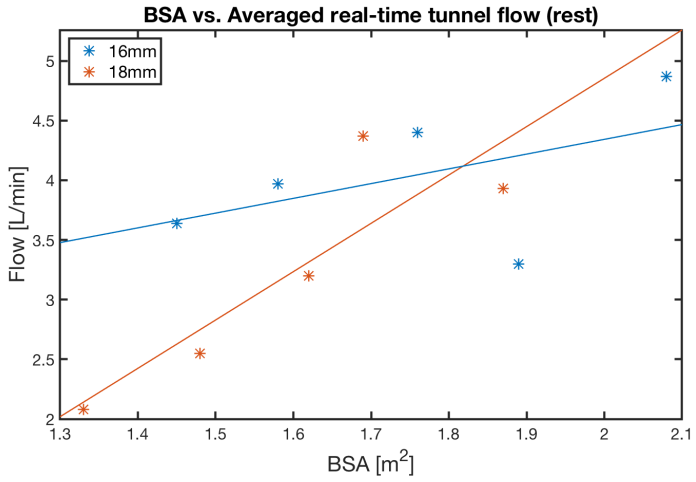

Figure 3.12: The relation between body surface area [m^2] and the averaged Fontan tunnel flow [L/min] measured with real-time MRI for two different implanted conduit size groups (16mm: r_s=0.40, p=0.51 & 18mm: r_s=0.90, p<0.05).

3.4.1. Fontan Tunnel Flow

The results show a strong significant positive correlation (r_s=0.90, p<0.05) for the patients with an 18 mm conduit implanted, between the averaged real-time tunnel flow, measured in resting condition, and BSA (see Fig. 3.12). In contrast, no significant correlation is found for the patient group with a 16 mm conduit implanted (r_s=0.40, p=0.51).

3.4.2. Power Loss and Pressure Drop

The power loss and pressure drop in relation to BSA are displayed in Fig. 3.13 and 3.14. For the patient group with a 16 mm conduit implanted, a strong significant positive correlation between power loss or pressure drop and BSA was observed. Specifically in a resting condition according to the full respiratory cycle (r_s=0.90, p<0.05) and inspiration phase (r_s=1.00, p<0.01). Also a non-significant positive correlation is seen for the exercise condition for the 16 mm conduit. The 18 mm conduit seems not to be correlated to BSA.

3.4.3. Normalised Resistance

The results according to the relation between normalised resistance and body growth is displayed in Fig. 3.15. The figure shows a strong significant positive correlation, for the patient group with a 16 mm conduit implanted. Specifically, in a resting condition according to the full respiratory cyle (r_s=1.00, p<0.01), inspiration phase (r_s=1.00, p<0.01) and expiration phase (r_s=1.00, p<0.01). As for the power loss and pressure drop, the correlation is also clearly present in exercise, although it is not significant. For the patients with a 18 mm conduit implanted no significant correlations are found.

3.4.4. Flow Stagnation Volume

The results for the correlations with BSA concerning the flow stagnation volume in the ECTC and Fontan tunnel, are displayed in Fig. 3.16. The top half of the figure show a strong significant correlation for the patients with a 16 mm conduit implanted between the flow stagnation volume in the ECTC and the body surface area in both physical conditions (rest: r_s=0.90, p<0.05 and exercise: r_s=1.00, p<0.01). No significant correlations were found for the flow stagnation volume in the Fontan tunnel, but a non-significant trend is visible for the 16 mm conduit. When interpreting these found results, it should be kept in mind that the blood flow velocity at the vessel wall is 0 m/s. Since the criteria for stagnated blood volume corresponds to a velocity between 0 m/s and 1 m/s, the amount of volume at the wall should be considered when interpreting the found results. Therefore, in Fig. 3.16 (top and bottom left), the amount of volume with a velocity of 0 m/s is presented. In the Fontan tunnel, these values correspond approximately with the minimal flow stagnation volumes, meaning that almost no flow stagnation exists with a velocity between 0 m/s and 0.1 m/s.

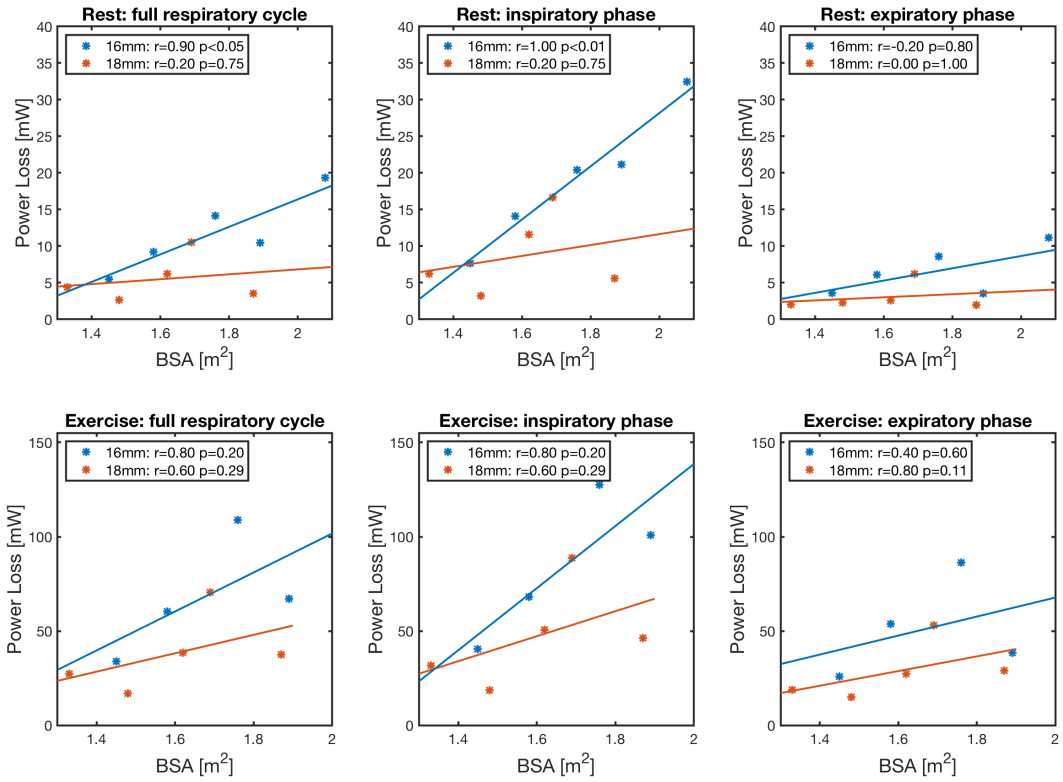

Figure 3.13: Power loss in relation to BSA given for two conduit size groups (16, 18 and 20 mm) in two physical conditions (rest and exercise) for the full respiration cycle, the inspiratory phase and the expiratory phase.

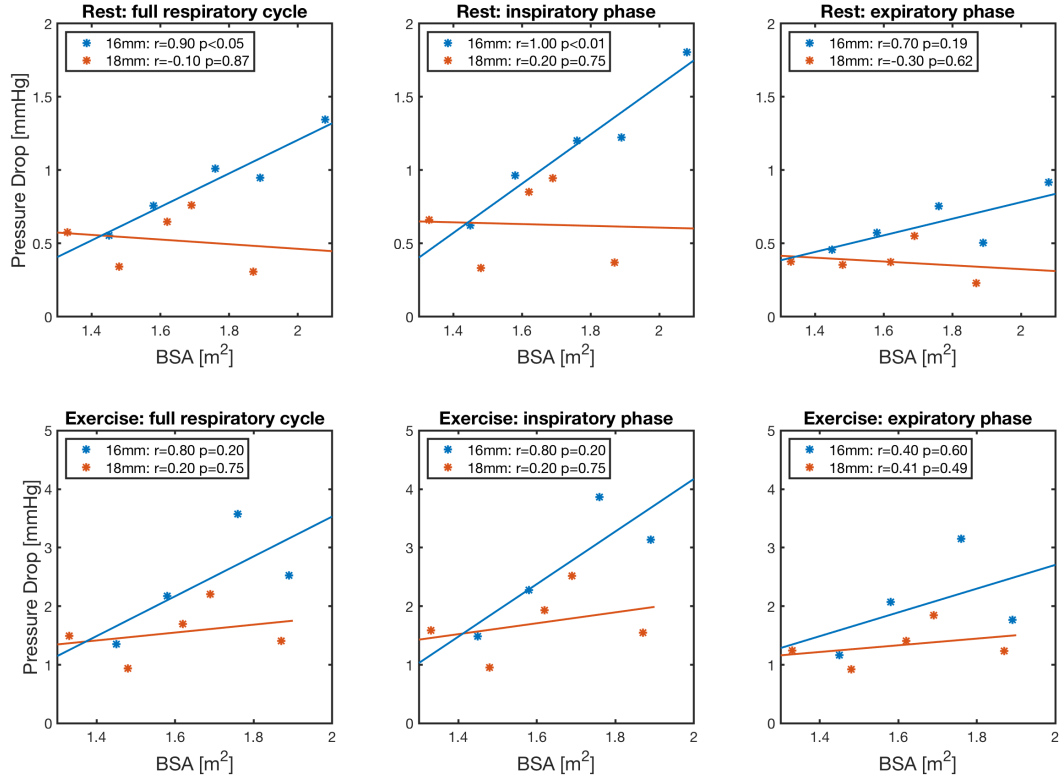

Figure 3.14: Pressure drop in relation to BSA given for two conduit size groups (16, 18 and 20 mm) in two physical conditions (rest and exercise) for the full respiration cycle, the inspiratory phase and the expiratory phase.

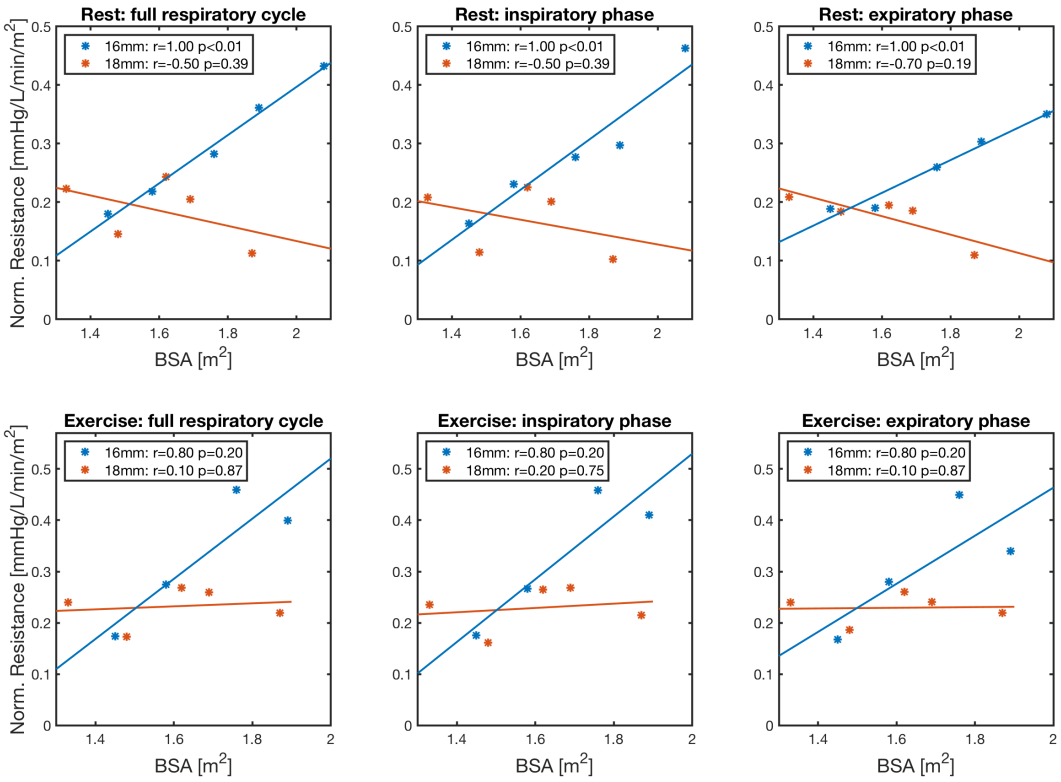

Figure 3.15: Normalised resistance in relation to BSA given for two conduit size groups (16, 18 and 20 mm) in two physical conditions (rest and exercise) for the full respiration cycle, the inspiratory phase and the expiratory phase.

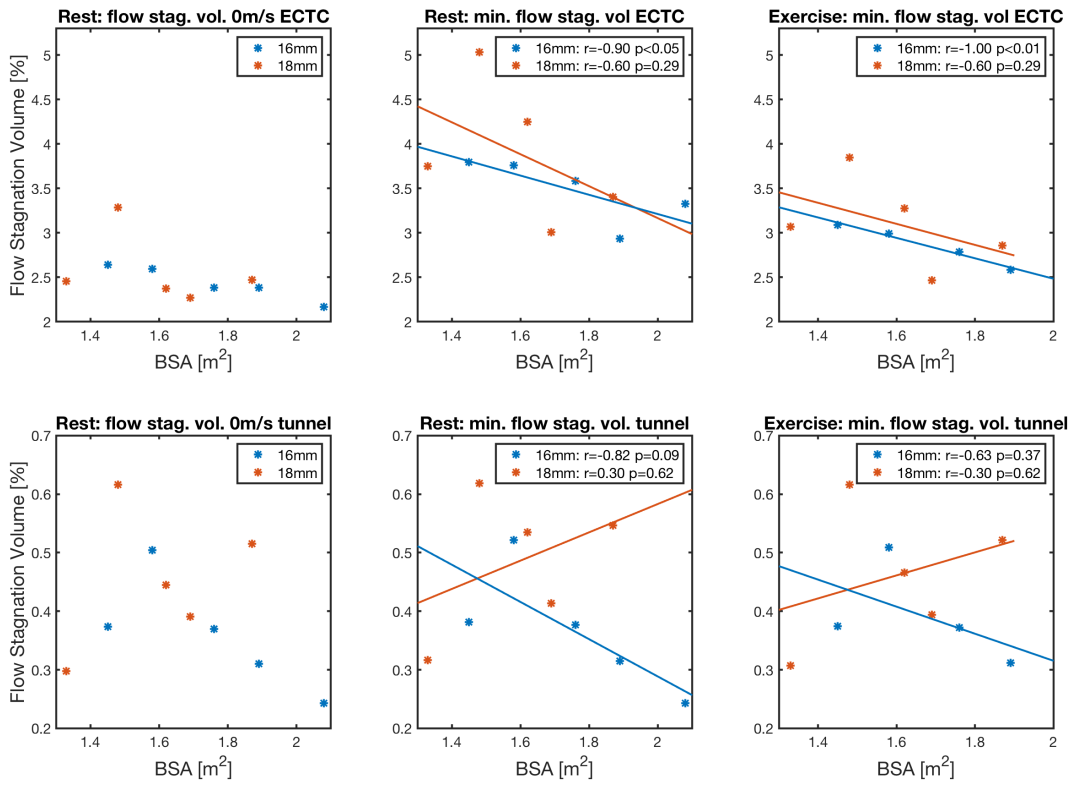

Figure 3.16: Minimal flow stagnation volume, in the ECTC and tunnel, in relation to BSA given for two conduit size groups (16, 18 and 20 mm) in two physical conditions (rest and exercise).

4

Discussion

The Fontan operation is the final stage of surgical palliation for children born with congenital heart defect with a single ventricle. In this procedure, the IVC is directly connected to the PAs via an extracardiac conduit, bypassing the heart. The extracardiac conduit exists in several conventional sizes. Little knowledge is available on the performance of these different sizes, especially when patients grow older. Therefore, it is difficult to make a well-informed choice on the conduit size at the time of implantation. This study aimed to investigate the impact of different conduit sizes on the hemodynamic performance of the Fontan circulation. More specifically, the performance of three conduit sizes (16, 18 and 20 mm) is researched and compared. In addition, the effect of increasing BSA to mimic body growth is studied concerning the performance of two conduit sizes (16 and 18 mm). With the acquired knowledge, probably better-substantiated choices can be made on the most suitable conduit size for each patient.

Furthermore, based on the literature, it was proposed that several additional variables, besides conduit size and body growth, affect the performance of the conduits. These parameters include physical condition and respiration. In order to verify their importance, they are investigated in the first place based on all patients included and then within the performance analysis of the different conduit sizes. The results are presented in the previous chapter and will be interpreted in this chapter. Also, the limitations, recommendations, and a general conclusion will be discussed.

4.1. Evaluation of the general results

Several interesting trends and relations are presented in the results on all patients of this study. First of all, the power loss and pressure drop appear to depend on the average tunnel flow in a resting condition. However, the normalised resistance was not related to the tunnel flow. This result was expected due to the correction for the systemic blood flow in calculating this parameter. Eliminating the influence of the systemic blood flow in the normalised resistance emphasises the role of the geometry, including conduit size, as a determinant in the conduit's performance.

Furthermore, with exercise, higher values were found for power loss, pressure drop and normalised resistance. These findings agree with the study of Whitehead et al. [58], which emphasises the importance of including exercise because baseline conditions may not adequately characterise the ECTC efficiency. When looking at the found flow stagnation volume, lower values were found compared to the resting condition. These lower values are in accordance with the study of Itatani et al. [33], but the values found in their study were much higher. High stagnation volumes are associated with the risk for thrombosis and can indicate oversized conduits. In the study of Itatani et al. [33], these numbers are in order of 5% to 35%. However, in the current study, the values are rather in the order of 1-5%. The low values indicate that the risk for thrombosis in these patients due to high stagnated volumes, i.e. oversized implanted conduits, was probably of no importance.

Furthermore, it was stated in the literature that the conduit's performance differs across the respiration cycle, specifically in inspiration and expiration [33]. The results found confirm this statement: inspiration

results in higher power losses and pressure drops but lower flow stagnation volumes compared to expiration.

The last variable researched in this study that may affect the conduit's performance is the body growth as reflected by an increasing BSA. The results show a clear positive correlation between BSA and power loss. In other words, body growth may have a disadvantageous effect on the conduit's hemodynamic performance according to the findings based on all patients included in the study.

Thus, overall, our data confirm the previously in the literature described relevance of several variables that significantly affect the conduit's performance. According to these findings, it is established that these variables should be considered when investigating the conduit's performance in any way. In this study particularly, when researching the different conduit sizes.

4.2. Performance evaluation of different implanted conduit sizes

4.2.1. Power Loss

The same trend was described for each conduit size, considering the power loss, as reported in the general results for all patients. Higher values are found with exercise and inspiration, emphasising the importance of considering these variables. The spread is quite wide for each of the three groups, probably due to the variation in average tunnel flows within each group. The average tunnel flow is, as mentioned before, strongly correlated with energy losses. Furthermore, no significant differences were found between the conduit size groups, probably due to the variation in tunnel flows and the small patient population. However, a clear trend exists of higher power losses in patients with a 16 mm conduit implanted. This result confirms the findings of the study of Hsia et al. [34], in which a decrease in power loss was found with increasing conduit size.

When having a closer look at the visualisation of the ECTC including a 16 mm conduit at the time of maximum power loss (see Fig. 3.6), it can be seen that the power losses occur in the transition from the IVC to the Fontan tunnel, indicating that the conduit is the origin of this inefficiency. Lower power loss values are found for the visualised 18 mm conduit with a smoother transition (see Fig. 3.5). This result is in accordance with the study of Rijnberg et al. [40], describing the relation between energy loss and the mismatch in velocity between the IVC and conduit as a consequence of a transition in size; the IVC-conduit size ratio. In their study, they found higher energy losses with a larger velocity mismatch. In other words, a non-smooth transition causes a considerable difference in velocity that results in higher energy losses.

4.2.2. Pressure Drop

As for the power loss, the same trends are found for pressure drop as for all patients taken together. Higher pressure drops are found with exercise and inspiration. Furthermore, the pressure drop decrease with conduit size. In particular, the difference between the 16 mm conduit and the other two conduit sizes is observed. Although only a significant difference between the 16 and 18 mm conduit was found in a resting condition during expiration, an overall clear trend is seen with statistics towards significant. It is expected that with a larger patient population, more significant differences between groups will be found.

Additional information is needed to place the found results on pressure drop in a clinical perspective. According to Ohm's law, an increase in flow through a resistor must be accompanied by an increase in pressure drop over the resistance. Normally, a patient has a right ventricle that pumps blood through the pulmonary arteries. These arteries can be seen as resistances, over which a pressure drop takes place. The resistance is also called pulmonary vascular resistance (PVR). The ventricle can compensate for this pressure drop by applying pressure through a contraction. However, this working principle is affected in a Fontan circulation. In the Fontan circulation, two main things are changed. First of all, an extra resistance, the conduit, is added to the circulation. Second, the organ normally responsible for overcoming the pressure drop across this resistance, the ventricle, has been removed from the circulation.

Consequently, in patients with a Fontan circulation, the central venous pressure (CVP) increases to overcome the pressure drop across the ECTC [64]. In this study, pressure drops up to 4 mmHg (in 16 mm conduits in exercise) are found. This pressure drop describes the resistance of the ECTC, meaning that the resistance of the pulmonary arteries, i.e. PVR, needs to be added up. To place the amount of ±4 mmHg in perspective,

the average pressure at CVP is 14 mmHg [65]. So, pressure drops found perform a considerable continuing burden on the CVP and the surrounding organs, with strong elevations caused by exercise. A chronic increase in CVP can, for example, lead to liver fibrosis and protein-losing enteropathy, which is a severe complication with an incidence of 4-13% after Fontan surgery [32, 66]. However, it is unknown whether the pressure drops found are clinically significant for these patients and need to be further investigated in a future study.

4.2.3. Normalised Resistance

For all three conduit sizes apart, the results found for the physical conditions and respiration are in accordance with the general results. Exercise causes higher normalised resistances, whereas no difference in the resistance is found for the two respiration phases. The spread of the data for each group is less wide than, for example, in the power loss. This might be due to the normalisation for flow in this parameter, which excludes the variation in tunnel flow within each group. Furthermore, as for the energy loss and pressure drop, the 16 mm conduit performs the least well considering the normalised resistances. Significant differences during the expiration phase in rest and exercise between the 16 mm conduit size and the other two conduit sizes confirm this statement. These results were expected regarding the found results for power loss and pressure drop. As mentioned earlier, this parameter mainly describes the effect of the geometry, including conduit size, of the ECTC on the conduit's performance. Therefore, the lesser performance of the 16 mm conduit is most likely caused by geometry related factors such as the conduit size rather than, for example, blood flow and body posture.

Since this parameter is normalised for flow, it is not expected to find a difference in physical condition. The exercise condition is simulated as an increase in blood flow; therefore, nothing has changed in the ECTC's resistance. However, slight differences in the normalised resistance are reported in the results. Although the actual resistance of the geometry did not change with exercise, the effective resistance of the ECTC may have changed. Meaning that due to a higher flow rate, the ECTC geometry is not used optimally and experiences more resistance because, for example, the flow with a high speed does not bend immediately right or left after the conduit with the geometry towards the pulmonary arteries, but first direct straight ahead and collides with the SVC flow resulting in possible vortices and recirculation. This effective resistance is then not only depending on the geometry but also on the flow patterns.

The found normalised resistances are in order of ±0.23 mmHg/L/min/m2 for the 16 mm conduit. To place this value in perspective, in the study of Haggerty et al. [59] the normal pulmonary vascular resistance has been reported to be ±1.5 WU in patients undergoing the Fontan procedure. The found value for the normalised resistance in the current study would add approximately 15% to the resistance that need to be overcome. 15% seems to be a considerable increase assigned to the inefficiency of the ECTC geometry. However, as described for the pressure drop, it is unknown whether these values are clinically significant and should be further researched in the future.

4.2.4. Flow Stagnation Volume

The results presented a decline in flow stagnation volume with exercise, both for the ECTC and tunnel. Also, an increase in flow stagnation volume in the ECTC is observed with an increase in conduit size, which is following the results found in the study of Itatani et al. [33]. However, no increase is observed for the flow stagnation in the tunnel. The stagnation volumes in the tunnel are ±0.5%, which is approaching zero and even includes the blood volume at the wall. These low stagnation volumes can be attributed to the fact that the blood velocity increases when the blood enters the tunnel (see Fig. 3.10 & Fig. 3.11) due to the difference in IVC-conduit size. These findings indicate that in this relatively older patient group (16.6 ±3.7 years), the flow stagnation in the tunnel does not play a role as a limiting factor, as it was in the study of Itatani et al. [33] that included young children (±3 years old). Therefore, it could be stated that the implanted 16, 18 and 20 mm conduits are not oversized for the current patient population.

4.3. The effect of body growth on the conduit's performance

All performance parameters seem to be strongly positively correlated with the BSA for patients with a 16 mm conduit implanted. In contrast, no correlations or trends were found for the patients with an 18 mm conduit implanted. For the 16 mm conduit, the clearest correlation was found for the normalised resistance. As mentioned earlier, the normalised resistance describes most precisely the influence of the geometry, includ-

ing the conduit size, due to normalisation for flow. Since body growth can cause changes in the geometry, this also affects the performance of the conduit. For example, the study of Hagler et al. [39] described body growth as the main cause for stenosed conduits in adults as a consequence of a lengthening conduit. Such a change in the geometry may influence the conduit's performance. However, in this study, no follow-up data was available to analyse the direct effect of body growth on the conduit's performance. Nevertheless, growth has been mimicked by selecting patients with an increase in BSA. Of course, these patients have a different geometry of the ECTC, but an attempt has been made to find out more about the effect with a cross-sectional study. Due to the wide range in BSA, it was expected that it would show up in the results if there was an effect. This effect was found for the patients with a 16 mm conduit implanted; a strong relationship was found. In contrast, no relation has been found for the 18 mm group. These results indicate that the 16 mm conduit size is detrimental to hemodynamic performance when patients grow. This finding is in accordance with the study of Rijnberg et al. [40], who also found a positive correlation between power loss and BSA. However, it does not seem to play any role in the performance of the 18 mm conduit.

4.4. Limitations

During the complete pipeline of the study, many choices are made, ranging from patient selection to choosing analysis procedure. Several limitations come with these choices. The most relevant limitations will be discussed here.

Patient population The number of patients included in this study is the main limitation. The low number, certainly viewed per group, are reflected in the relationships and p-values found. However, from the results, it appears that the number of patients included already allows highlighting existing trends. This finding is promising for future studies that include larger patient groups. It is relevant to mention here that only a small selection of a larger cohort has been used in the current study. Therefore, it is intended to expand this study using the same research pipeline but includes the remaining patients of the cohort.

MRI acquisition and boundary conditions Already prior to this study, the MRI acquisition is performed by the research group. Due to technical issues, the flow in the hepatic veins and pulmonary arteries is not acquired with real-time MRI. Instead, the HV flow is calculated from the flow in the IVC and tunnel, and the outflow through the pulmonary arteries is based on flow ratios acquired from 2D ECG gated 3dir PC-MRI. These simplifications may affect the results. However, it is not expected to have that large influence since the flow through the hepatic veins is still included using an approximation and contributes to a lesser extent than the IVC. For the outflow ratios, the value is averaged, and it is not expected that the simplification will have an essential effect on the results.

Flow extensions The reasoning for the inclusion of the flow extensions is already discussed in chapter 2.6. Although the pros outweighed the cons, it does bring errors in the outcome data. In order to quantify the error in the outcome data, a small analysis was performed. The maximum power loss is calculated, for three patients, including and excluding the flow extensions. The results show an increase of 18% when including the flow extensions, which is quite a large overestimation. The absolute values found, including the overestimation, should therefore be interpreted with care. In this study, the data was mainly used to compare the included groups and find general trends.

Exercise As described, the simulated exercise condition was approximated based on variables found in the literature. Although this simulation is expected to be close to reality, it has not been an actual patient-specific measurement. The results found clearly show what a possible effect is of exercise compared to the resting condition. However, for further research, it would be ideal to perform MRI measurements when the patient is exercising so that the exercise condition can be included on a patient-specific basis and compared to the simulated exercise results.

Body growth In this study, body growth was approached using different patients with ascending BSAs. This approach has been used because no follow-up data was available. With the use of different patients, individual factors will have influenced the results. Although clear trends have been found, the data is less reliable than when data would be used from each patient measured at different moments over several years. However,

the found results show a strong correlation for the patients with a 16 mm conduit implanted and no correlation for the patients with an 18 mm conduit implanted. Since these are evident findings, it is not expected that the results would be highly different. Although these results seem convincing, it will be very interesting to do follow-up measurements in future research to confirm the trends found here.

Tunnel extraction In order to analyse the performance of the tunnel considering the flow stagnation volume, the tunnel is extracted from the ECTC geometry with the use of a box clipping tool. This method approximates the tunnel geometry pretty well but not exactly due to missing small parts of the tunnel geometry that fell outside the box. It will not have made much difference for this study because the values found for the flow stagnation volume are so low in the tunnel that they do not limit the conduit's performance. It is therefore not expected that this conclusion would have been different with slightly more precise data. However, it might be better for future research to extract the tunnel exactly when it is desired to investigate other parameters in the tunnel.

Implanted versus measured conduit size Although promising trends are already emerging from the data obtained regarding conduit sizes and their performance, it is important to realise that these are implanted conduit sizes. In a recent study by Patel et al. [67], the change in conduit size with patient growth is researched. For a patient cohort of 158 patients, a decrease in cross-sectional area of 33% was found within approximately ten years after implantation. It is, therefore, expected that the implanted conduit size has also changed in the patients included in this study. Consequently, it is possible that conduit sizes from, for example, the 20 mm group have become smaller than conduits from the 18 mm group. Mixing up between groups could explain the fairly wide range of results within the groups. Furthermore, the conduit could be stretched and changed in shape, as was explained by the study of Hagler et al. [39]. Thus, the conduit as present in the body at the time of measurements will have to be further investigated in future research through a new classification based on the actual conduit size and considering the degree to which the conduit is changed in, for example, shape and length. The expectation is that more explicit differences will then emerge between groups.

Thrombus formation risk In this study, flow stagnation volume below a threshold of 0.01 m/s is used as a parameter to quantify thrombus formation risk. This parameter is a simplified approach that only includes low shear stress areas and neglect other possibly relevant indicators such as high shear stresses that are present in colliding blood flow areas [62] [68]. However, these additional indicators have not yet been studied in a Fontan circulation. So, existing knowledge on various shear stress-related aspects involved in thrombus formation is not yet fully exploited in Fontan patients, and it is unknown which parameters are most relevant for increased thrombosis risk in the Fontan circulation. Since the parameters are unknown, it was chosen in this study only to include the blood flow stagnation volume to explore the thrombus risk. However, it is obvious that this parameter falls short in describing the risk of thrombosis in these patients. Further fundamental research will therefore have to be carried out in order to be able to describe relevant parameters.

4.5. Clinical relevance

The main clinical goal of this research is to improve the quality of life of patients with a Fontan circulation. Investigation of the hemodynamics in the Fontan circulation may have clinical consequences. First of all, the found results present the 16 mm conduit being less efficient than the 18 and 20 mm conduits. This result may affect the choice of clinicians on implanting a certain conduit size during the Fontan procedure. However, whether the 18 and 20 mm conduit perform well enough can be questioned and should be further investigated according to clinical indicators. Furthermore, for patients with an inefficient Fontan circulation, it can be considered whether any adjustments to the existing geometry may improve their quality of life. A more efficient Fontan circulation increases the chance of fewer side effects such as liver fibrosis and an exhausted heart. However, it is important to consider the pros and cons per patient. Patients with inefficient Fontan circulation and a lesser exercise tolerance may be eligible for an adjustment in the ECTC geometry. Improving efficiency could increase this tolerance and thus improve the quality of life. From a clinical-technical point of view, patients who are eligible for geometry adjustments must meet two things. First, they have a high normalised resistance indicating an inefficient geometry of the ECTC. Second, they have a low PVR. Meaning that the resistance to overcome mainly comes from the ECTC geometry rather than from the pulmonary vessels. These two aspects are necessary to ensure that an adjustment in the geometry would have a positive

effect. Thus, the results of this study may have a clinically relevant contribution but will always have to be considered in a patient-specific and clinical context.

4.6. Recommendations

The most relevant recommendation is to increase the patient population. The results found in this study can then be confirmed, and more generalising conclusions can be drawn that may be clinically relevant. Furthermore, it is important to perform an additional analysis using the actual conduit size measured in the patients. This analysis will provide insight into the actual relationship of the conduit size with the performance parameters. If possible, ideally, some adjustments should be made to the method to make the results as realistic and reliable as possible, such as incorporating real exercise data and patient-specific body growth. From a technical perspective, performing simulations including variable outflow ratios instead of constant outflow ratios and analysing the outcome data without flow extensions would make the results even more relevant. However, these are major adjustments taking much work that may not be of important influence in demonstrating the trends and relationships as they already emerge from a small study such as this one. Furthermore, a fundamental study is needed to identify the relevant parameters that determine thrombosis risks. Finally, it would be very interesting to link the results found to clinical outcome parameters of these specific patients. With this linkage, the consequences of an inefficient Fontan circulation for the patient's quality of life could be determined.

4.7. General Conclusion

Overall, the 16mm conduit clearly underperforms the 18 and 20mm conduits regarding hemodynamical performance parameters. A statistical difference between the 18 and 20 mm conduits was not found in this study with the small patient population. Whether the 18 and 20 mm conduits perform clinically good enough need to be further investigated with clinical relevant indicators such as exercise tolerance. Furthermore, exercise and respiration appear to affect the conduit's performance significantly. Concerning body growth, the data shows that it negatively influences the conduit's performance for the patients with a 16 mm conduit implanted but not for the patients with an 18 mm conduit. Although these results have already become well visible with the current data, these results must be confirmed based on a larger patient population, possibly including patient-specific follow-up data and exercise measurements.

Bibliography

[1] Alyse M. Baron, Richard L. Donnerstein, Eric Kanter, F. John Meaney, and Stanley J. Goldberg. Congential heart disease in the Medicaid population of Southern Arizona. *American Journal of Cardiology*, 88(4): 462–465, aug 2001. ISSN 00029149. doi: 10.1016/S0002-9149(01)01706-4.

[2] S L Chadha, Neerpal Singh, and D K Shukla. Epidemiological Study of Congenital Heart Disease. Technical report.

[3] Ariane J Marelli, Andrew S Mackie, Raluca Ionescu-Ittu, Elham Rahme, and Louise Pilote. Congenital Heart Disease in the General Population Changing Prevalence and Age Distribution. 2007. doi: 10.1161/CIRCULATIONAHA.106.627224. URL http://www.circulationaha.org.

[4] S Mendis, P Puska, and B Norrving. Global atlas on cardiovascular disease prevention and control. *World Health Organization*, 2011.

[5] What Are Congenital Heart Defects?, 2011. URL https://web.archive.org/web/20150813182642/http:/www.nhlbi.nih.gov/health/health-topics/topics/chd/.

[6] S C Mitchell, S B Korones, and H W Berendes. Congenital Heart Disease in 56,109 Births Incidence and Natural History. Technical report. URL http://ahajournals.org.

[7] Walter F Boron and Emile L Boulpaep. *Medical Physiology, 2e Updated Edition: with STUDENT CONSULT Online Access*. 2012. ISBN 1455711810. URL https://books.google.nl/books?hl=nl{&}lr={&}id=54mxMgO5H{_}YC{&}oi=fnd{&}pg=PP1{&}dq=Boron,+W.+F.,+{%}26+Boulpaep,+E.+L.+(2012).+Medical+Physiology,+2e+Updated+Edition+E-Book.+Elsevier+health+sciences.{&}ots=lPoghJtp7l{&}sig=ZIIEgXq5ICuNL177ATjVhUig-d8{#}v=onepage{&}q=Boron{%}2C.

[8] F.O. Campos. Modeling Atrial Activation Sequences in the Rabbit Heart in Macroscopic and Microscopic Dimensions. *Graz University of Technology*, 2012. doi: 10.13140/2.13828.99204.

[9] Willem A. Helbing, Jelle P.G. van der Ven, Eva van den Bosch, and Ad J.C.C. Bogers. State of the art of the Fontan strategy for treatment of univentricular heart disease [version 1; referees: 2 approved]. *F1000Research*, 7(0):1–14, 2018. ISSN 1759796X. doi: 10.12688/f1000research.13792.1.

[10] Marc Gewillig. The Fontan circulation. *Heart*, 91(6):839–846, 2005. ISSN 13556037. doi: 10.1136/hrt.2004.051789.

[11] Daniëlle Robbers-Visser, Martijn Miedema, Aagje Nijveld, Eric Boersma, Ad J J C Bogers, Felix Haas, Willem A Helbing, and Livia Kapusta. Results of staged total cavopulmonary connection for functionally univentricular hearts; comparison of intra-atrial lateral tunnel and extracardiac conduit. 2009. doi: 10.1016/j.ejcts.2009.10.016. URL www.elsevier.com/locate/ejcts.

[12] S.H. Martinez. *Hypoplastic Left Heart Syndrome*. PhD thesis, 2016. URL https://radiologykey.com/hypoplastic-left-heart-syndrome/.

[13] M. R. De Leval, P. Kilner, M. Gewillig, and C. Bull. Total cavopulmonary connection: A logical alternative to atriopulmonary connection for complex Fontan operations. Experimental studies and early clinical experience. *Journal of Thoracic and Cardiovascular Surgery*, 96(5):682–695, 1988. ISSN 00225223. doi: 10.1016/s0022-5223(19)35174-8. URL http://dx.doi.org/10.1016/S0022-5223(19)35174-8.

[14] Kevin O. Maher, Christian Pizarro, Samuel S. Gidding, Katarzyna Januszewska, Edward Malec, William I. Norwood, and John D. Murphy. Hemodynamic profile after the Norwood procedure with right ventricle to pulmonary artery conduit. *Circulation*, 108(7):782–784, aug 2003. ISSN 00097322. doi: 10.1161/01.CIR.0000087338.09589.21. URL http://www.circulationaha.org.

[15] Girish Warrier, M Ch, Baiju Sasi Dharan, Sajan Koshy, Shenoj Kumar, Shivaprakasha Krishnanaik, and Gururaja Rao. Bidirectional glenn operation in infancy. Technical report.

[16] F Fontan and E Baudet. Surgical repair of tricuspid atresia. *Thorax*, page 240, 1971. doi: 10.1136/thx.26.3.240. URL http://thorax.bmj.com/.

[17] Gnalini Sathananthan, Boris S Lowe, and Tim S Hornung. THE FONTAN CIRCULATION. Technical report, 2016.

[18] Treatment for Your Child's Hypoplastic Ventricle: Stage III. Saint Luke's Health System, 2020. URL https://www.saintlukeskc.org/health-library/treatment-your-childs-hypoplastic-ventricle-stage-iii.

[19] Sandeep Nayak and Peter D. Booker. The Fontan circulation. *Continuing Education in Anaesthesia, Critical Care and Pain*, 8(1):26–30, 2008. ISSN 17431824. doi: 10.1093/bjaceaccp/mkm047. URL https://academic.oup.com/bjaed/article/8/1/26/277637.

[20] Lindsay S Rogers, Andrew C Glatz, Chitra Ravishankar, Thomas L Spray, Susan C Nicolson, Jack Rychik, † Christina, Hayden Rush, J William Gaynor, David J Goldberg, and † Philadelphia. 18 Years of the Fontan Operation at a Single Institution. *Journal of the American College of Cardiology*, 60:1018–1025, 2012. doi: 10.1016/j.jacc.2012.05.010. URL http://dx.doi.org/10.1016/j.jacc.2012.05.010.

[21] Yves D'udekem, Ajay J. Iyengar, John C. Galati, Victoria Forsdick, Robert G. Weintraub, Gavin R. Wheaton, Andrew Bullock, Robert N. Justo, Leeanne E. Grigg, Gary F. Sholler, Sarah Hope, Dorothy J. Radford, Thomas L. Gentles, David S. Celermajer, and David S. Winlaw. Redefining expectations of long- Term survival after the fontan procedure twenty-five years of follow-up from the entire population of Australia and New Zealand. *Circulation*, 130(11):S32–S38, 2014. ISSN 15244539. doi: 10.1161/CIRCULATIONAHA.113.007764. URL http://circ.ahajournals.org.

[22] Eva Van Den Bosch, Sjoerd S M Bossers, J J C Bogers, Daniëlle Robbers-Visser, Arie P J Van Dijk, Jolien W Roos-Hesselink, Hans M P J Breur, Felix Haas, Livia Kapusta, Willem A Helbing, and W A Helbing. Staged total cavopulmonary connection: serial comparison of intra-atrial lateral tunnel and extracardiac conduit taking account of current surgical adaptations. *Interactive CardioVascular and Thoracic Surgery*, 29:453–460, 2019. doi: 10.1093/icvts/ivz081. URL https://academic.oup.com/icvts/article/29/3/453/5436498.

[23] Matthew S. Lemler, Claudio Ramaciotti, Daniel Stromberg, William A. Scott, and Steven R. Leonard. The extracardiac lateral tunnel Fontan, constructed with bovine pericardium: Comparison with the extracardiac conduit Fontan. *American Heart Journal*, 151(4):928–933, 2006. ISSN 00028703. doi: 10.1016/j.ahj.2005.06.015.

[24] Toshihide Nakano, Hideaki Kado, Hideki Tatewaki, Kazuhiro Hinokiyama, Shinichiro Oda, Hiroya Ushinohama, Koichi Sagawa, Makoto Nakamura, Naoki Fusazaki, and Shiro Ishikawa. Results of extracardiac conduit total cavopulmonary connection in 500 patients. *European Journal of Cardio-thoracic Surgery*, 48(6):825–832, 2015. ISSN 1873734X. doi: 10.1093/ejcts/ezv072. URL https://academic.oup.com/ejcts/article/48/6/825/2465055.

[25] E. Petrossian, V. M. Reddy, D. B. McElhinney, G. P. Akkersdijk, P. Moore, A. J. Parry, L. D. Thompson, F. L. Hanley, and R. A. Jonas. Early results of the extracardiac conduit fontan operation. *Journal of Thoracic and Cardiovascular Surgery*, 117(4):688–696, 1999. ISSN 00225223. doi: 10.1016/S0022-5223(99)70288-6.

[26] Vincent K.H. Tam, Bruce E. Miller, and Kathy Murphy. Modified Fontan without use of cardiopulmonary bypass. *Annals of Thoracic Surgery*, 68(5):1698–1703, 1999. ISSN 00034975. doi: 10.1016/S0003-4975(99)01067-X.

[27] Anthony Azakie, Brian W. McCrindle, Glen Van Arsdell, Lee N. Benson, John Coles, Robert Hamilton, Robert M. Freedom, and William G. Williams. Extracardiac conduit versus lateral tunnel cavopulmonary connections at a single institution: Impact on outcomes. *Journal of Thoracic and Cardiovascular Surgery*, 122(6):1219–1228, 2001. ISSN 00225223. doi: 10.1067/mtc.2001.116947.

[28] Carlo F. Marcelletti, Fiore S. Iorio, and Raul F. Abella. Late Results of Extracardiac Fontan Repair. *Seminars in Thoracic and Cardiovascular Surgery: Pediatric Cardiac Surgery Annual*, 2(1):131–141, 1999. ISSN 10929126. doi: 10.1016/s1092-9126(99)70014-1. URL http://dx.doi.org/10.1016/S1092-9126(99)70014-1.

[29] Lucio Careddu, Francesco Dimitri Petridis, Emanuela Angeli, Anna Balducci, Elisabetta Mariucci, Gabriele Egidy Assenza, Andrea Donti, and Gaetano Domenico Gargiulo. Dacron Conduit for Extracardiac Total Cavopulmonary Anastomosis: A Word of Caution. *Heart Lung and Circulation*, 28(12):1872–1880, dec 2019. ISSN 14442892. doi: 10.1016/j.hlc.2018.11.005.

[30] Cheul Lee, Chang-Ha Lee, Seong Wook Hwang, Hong Gook Lim, Soo-Jin Kim, Jae Young Lee, Woo-Sup Shim, and Woong-Han Kim. Midterm follow-up of the status of Gore-Tex graft after extracardiac conduit Fontan procedure §. *European journal of cardio-thoracic surgery*, 31(6):1008–1012, 2007. doi: 10.1016/j.ejcts.2007.03.013. URL www.elsevier.com/locate/ejcts.

[31] Friso M. Rijnberg, Mark G. Hazekamp, Jolanda J. Wentzel, Patrick J.H. De Koning, Jos J.M. Westenberg, Monique R.M. Jongbloed, Nico A. Blom, and Arno A.W. Roest. Energetics of blood flow in cardiovascular disease: Concept and clinical implications of adverse energetics in patients with a fontan circulation. *Circulation*, 137(22):2393–2407, 2018. ISSN 15244539. doi: 10.1161/CIRCULATIONAHA.117.033359.

[32] Marc Gewillig and David J Goldberg. Failure of the Fontan Circulation. *Heart Failure Clinics*, 10(1):105–116, 2014.

[33] Keiichi Itatani, Kagami Miyaji, Takahiro Tomoyasu, Yayoi Nakahata, Kuniyoshi Ohara, Shinichi Takamoto, and Masahiro Ishii. Optimal Conduit Size of the Extracardiac Fontan Operation Based on Energy Loss and Flow Stagnation. *The Annals of thoracic surgery*, 88(2):565–573, 2009. doi: 10.1016/j.athoracsur.2009.04.109.

[34] Tain Yen Hsia, Francesco Migliavacca, Simone Pittaccio, Alessandro Radaelli, Gabriele Dubini, Giancarlo Pennati, and Marc De Leval. Computational fluid dynamic study of flow optimization in realistic models of the total cavopulmonary connections. *Journal of Surgical Research*, 116(2):305–313, 2004. ISSN 00224804. doi: 10.1016/j.jss.2003.08.004.

[35] Sang Yun Lee, Mi kyoung Song, Gi Beom Kim, Eun Jung Bae, Seong Ho Kim, So Ick Jang, Sung Kyu Cho, Jae Gun Kawk, Woong Han Kim, Chang Ha Lee, Hyun Jeong Kim, and Jayoun Kim. Relation Between Exercise Capacity and Extracardiac Conduit Size in Patients with Fontan Circulation. *Pediatric Cardiology*, 40(8):1584–1590, 2019. ISSN 14321971. doi: 10.1007/s00246-019-02190-4. URL https://doi.org/10.1007/s00246-019-02190-4.

[36] Robert J. Dabal, James K. Kirklin, Manisha Kukreja, Robert N. Brown, David C. Cleveland, Michael C. Eddins, and Yung Lau. The modern Fontan operation shows no increase in mortality out to 20 years: A new paradigm. *Journal of Thoracic and Cardiovascular Surgery*, 148(6):2517–2524.e1, 2014. ISSN 1097685X. doi: 10.1016/j.jtcvs.2014.07.075. URL http://dx.doi.org/10.1016/j.jtcvs.2014.07.075.

[37] Sungkyu Cho, Woong Han Kim, Eun Seok Choi, Jae Gun Kwak, Hyoung Woo Chang, Kwanyong Hyun, and Chang Ha Lee. Outcomes after extracardiac Fontan procedure with a 16-mm polytetrafluoroethylene conduit. *European Journal of Cardio-thoracic Surgery*, 53(1):269–275, 2018. ISSN 1873734X. doi: 10.1093/ejcts/ezx238. URL https://academic.oup.com/ejcts/article-abstract/53/1/269/4080375.

[38] R J Ascuitto, D W Kydon, and N T Ross-Ascuitto. Pressure Loss from Flow Energy Dissipation: Relevance to Fontan-Type Modifications. *Pediatric Cardiology*, 22(2):110–115, 2001. doi: 10.1007/s002460010172.

[39] Donald J. Hagler, William R. Miranda, Brielle J. Haggerty, Jason H. Anderson, Jonathan N. Johnson, Frank Cetta, Sameh M. Said, and Nathaniel W. Taggart. Fate of the Fontan connection: Mechanisms of stenosis and management. *Congenital Heart Disease*, 14(4):571–581, 2019. ISSN 17470803. doi: 10.1111/chd.12757.

[40] Friso M Rijnberg, Mohammed S M Elbaz, Jos J M Westenberg, Vivian P Kamphuis, Willem A Helbing, Lucia J Kroft, Nico A Blom, Mark G Hazekamp, and Arno A W Roest. Four-dimensional

flow magnetic resonance imaging-derived blood flow energetics of the inferior vena cava-to-extracardiac conduit junction in Fontan patients. *European Journal of Cardio-Thoracic Surgery*, 55(6):1202–1210, jun 2019. ISSN 1010-7940. doi: 10.1093/ejcts/ezy426. URL https://academic.oup.com/ejcts/article-abstract/55/6/1202/5259359?redirectedFrom=fulltexthttps://academic.oup.com/ejcts/article/55/6/1202/5259359.

[41] J.A. Elger, D.F., LeBret, B.A., Crowe, C.T., Roberson. Engineering fluid mechanics. John Wiley and Sons Inc., 2020.

[42] Laurent Stainier. *A Variational Approach to Modeling Coupled Thermo-Mechanical Nonlinear Dissipative Behaviors*, volume 46. Elsevier Inc., 1 edition, 2013. ISBN 9780123965226. doi: 10.1016/B978-0-12-396522-6.00002-5. URL http://dx.doi.org/10.1016/B978-0-12-396522-6.00002-5.

[43] Yunlong Liu, Alfred Moser, Daniel Gubler, and Alois Schaelin. Influence of time step length and subiteration number on the convergence behavior and numerical accuracy for transient CFD. In *Proceedings of the 11th Annual Conference of the CFD Society of Canada*, pages 481–486, 2003.

[44] R Woodward, P, Freimarck. MRI for Technologists. 1995.

[45] Gabrielle Torre. The Brain's Building Blocks: Of Protons and Voxels, 2017. URL https://knowingneurons.com/2017/09/27/mri-voxels/.

[46] Patrick Le Fèvre. Safe power in magnetic resonance imaging environment, 2019.

[47] Perry Sprawls. *Magnetic Resonance Imaging: principles, methods and techniques*. Medical Physics Publishing, Madison, 2000.

[48] A.S. Mushabbar. Basic Principles of Cardiovascular MRI. 2015.

[49] Paul Yushkevich, Joseph Piven, Heather Cody, and Sean Ho. User-guided level set segmentation of anatomical structures with ITK-SNAP. *Neuroimage*, 31(3):1116–1128, 2006. URL www.cognitica.com/snap.

[50] Luca Antiga, Marina Piccinelli, Lorenzo Botti, Bogdan Ene-Iordache, Andrea Remuzzi, and David A. Steinman. An image-based modeling framework for patient-specific computational hemodynamics. *Medical and Biological Engineering and Computing*, 46(11):1097–1112, 2008. ISSN 01400118. doi: 10.1007/s11517-008-0420-1.

[51] Phillip M. Trusty, Zhenglun Wei, Megan Sales, Kirk R. Kanter, Mark A. Fogel, Ajit P. Yoganathan, and Timothy C. Slesnick. Y-graft modification to the Fontan procedure: Increasingly balanced flow over time. *Journal of Thoracic and Cardiovascular Surgery*, 159(2):652–661, 2020. ISSN 1097685X. doi: 10.1016/j.jtcvs.2019.06.063. URL https://doi.org/10.1016/j.jtcvs.2019.06.063.

[52] Zhenglun Alan Wei, Connor Huddleston, Phillip M. Trusty, Shelly Singh-Gryzbon, Mark A. Fogel, Alessandro Veneziani, and Ajit P. Yoganathan. Analysis of Inlet Velocity Profiles in Numerical Assessment of Fontan Hemodynamics. *Annals of Biomedical Engineering*, 47(11):2258–2270, 2019. ISSN 15739686. doi: 10.1007/s10439-019-02307-z.

[53] Taewon Seo, Levanto G Schachter, and Abdul I Barakat. Computational study of fluid mechanical disturbance induced by endovascular stents. *Annals of Biomedical Engineering*, 33(4):444–456, 2005. ISSN 00906964. doi: 10.1007/s10439-005-2499-y.

[54] Zhenglun Wei, Kevin K. Whitehead, Reza H. Khiabani, Michael Tree, Elaine Tang, Stephen M. Paridon, Mark A. Fogel, and Ajit P. Yoganathan. Respiratory Effects on Fontan Circulation during Rest and Exercise Using Real-Time Cardiac Magnetic Resonance Imaging. *Annals of Thoracic Surgery*, 101(5):1818–1825, 2016. ISSN 15526259. doi: 10.1016/j.athoracsur.2015.11.011. URL http://dx.doi.org/10.1016/j.athoracsur.2015.11.011.

[55] Colin Pennington and M.S. Kinesiology. The Exercise Effect on the Anaerobic Threshold in Response to Graded Exercise. *International Journal of Health Sciences (IJHS)*, 3(1), 2015. ISSN 23725060. doi: 10.15640/ijhs.v3n1a14.

[56] V. E. Hjortdal, K. Emmertsen, E. Stenbøg, T. Fründ, M. Rahbek Schmidt, O. Kromann, K. Sørensen, and E. M. Pedersen. Effects of exercise and respiration on blood flow in total cavopulmonary connection: A real-time magnetic resonance flow study. *Circulation*, 108(10):1227–1231, 2003. ISSN 00097322. doi: 10.1161/01.CIR.0000087406.27922.6B.

[57] Zhenglun Alan Wei, Michael Tree, Phillip M. Trusty, Wenjun Wu, Shelly Singh-Gryzbon, and Ajit Yoganathan. The Advantages of Viscous Dissipation Rate over Simplified Power Loss as a Fontan Hemodynamic Metric. *Annals of Biomedical Engineering*, 46(3):404–416, 2018. ISSN 15739686. doi: 10.1007/s10439-017-1950-1.

[58] Kevin K. Whitehead, Kerem Pekkan, Hiroumi D. Kitajima, Stephen M. Paridon, Ajit P. Yoganathan, and Mark A. Fogel. Nonlinear power loss during exercise in single-ventricle patients after the Fontan: Insights from computational fluid dynamics. *Circulation*, 116(11 SUPPL. 1):165–171, 2007. ISSN 00097322. doi: 10.1161/CIRCULATIONAHA.106.680827.

[59] Christopher M. Haggerty, Maria Restrepo, Elaine Tang, Diane A. De Zélicourt, Kartik S. Sundareswaran, Lucia Mirabella, James Bethel, Kevin K. Whitehead, Mark A. Fogel, and Ajit P. Yoganathan. Fontan hemodynamics from 100 patient-specific cardiac magnetic resonance studies: A computational fluid dynamics analysis. *Journal of Thoracic and Cardiovascular Surgery*, 148(4):1481–1489, 2014. ISSN 1097685X. doi: 10.1016/j.jtcvs.2013.11.060.

[60] Kartik S Sundareswaran, Kerem Pekkan, Lakshmi P Dasi, Kevin Whitehead, Shiva Sharma, Kirk R Kanter, Mark A Fogel, and Ajit P Yoganathan. The total cavopulmonary connection resistance: A significant impact on single ventricle hemodynamics at rest and exercise. *American Journal of Physiology - Heart and Circulatory Physiology*, 295(6):2427–2435, 2008. ISSN 03636135. doi: 10.1152/ajpheart.00628.2008. URL `www.ajpheart.org`.

[61] David J. Goldberg and Stephen M. Paridon. Fontan circulation: The search for targeted therapy. *Circulation*, 130(23):1999–2001, 2014. ISSN 15244539. doi: 10.1161/CIRCULATIONAHA.114.013365.

[62] Chantal Attard, Joanna Huang, Paul Monagle, and Vera Ignjatovic. Pathophysiology of thrombosis and anticoagulation post Fontan surgery. *Thrombosis Research*, 172(November 2017):204–213, 2018. ISSN 18792472. doi: 10.1016/j.thromres.2018.04.011. URL `https://doi.org/10.1016/j.thromres.2018.04.011`.

[63] Scott L. Diamond. Systems Analysis of Thrombus Formation. *Circulation Research*, 118(9):1348–1362, 2016. ISSN 15244571. doi: 10.1161/CIRCRESAHA.115.306824.

[64] Yvette Koeken, Theo Arts, and Tammo Delhaas. Simulation of the Fontan circulation during rest and exercise. *Proceedings of the Annual International Conference of the IEEE Engineering in Medicine and Biology Society, EMBS*, pages 6673–6676, 2012. ISSN 1557170X. doi: 10.1109/EMBC.2012.6347525.

[65] Antonio F. Corno, Matt J. Owen, Andrea Cangiani, Edward J.C. Hall, and Aldo Rona. Physiological Fontan procedure. *Frontiers in Pediatrics*, 7(MAY):196, may 2019. ISSN 22962360. doi: 10.3389/fped.2019.00196. URL `www.frontiersin.org`.

[66] D. Holmgren, H. Berggren, H. Wåhlander, M. Hallberg, and U. Myrdal. Reversal of protein-losing enteropathy in a child with Fontan circulation is correlated with central venous pressure after heart transplantation. *Pediatric Transplantation*, 5(2):135–137, 2001. ISSN 13973142. doi: 10.1034/j.1399-3046.2001.005002135.x.

[67] Neil D. Patel, Connie Friedman, Cynthia Herrington, John C. Wood, and Andrew L. Cheng. Progression in Fontan conduit stenosis and hemodynamic impact during childhood and adolescence. *Journal of Thoracic and Cardiovascular Surgery*, 90027:1–12, 2020. ISSN 1097685X. doi: 10.1016/j.jtcvs.2020.09.140. URL `https://doi.org/10.1016/j.jtcvs.2020.09.140`.

[68] Akshita Rana, Erik Westein, Be'eri Niego, and Christoph E. Hagemeyer. Shear-Dependent Platelet Aggregation: Mechanisms and Therapeutic Opportunities. *Frontiers in Cardiovascular Medicine*, 6 (September):1–21, 2019. ISSN 2297055X. doi: 10.3389/fcvm.2019.00141.

A

Technical pipeline

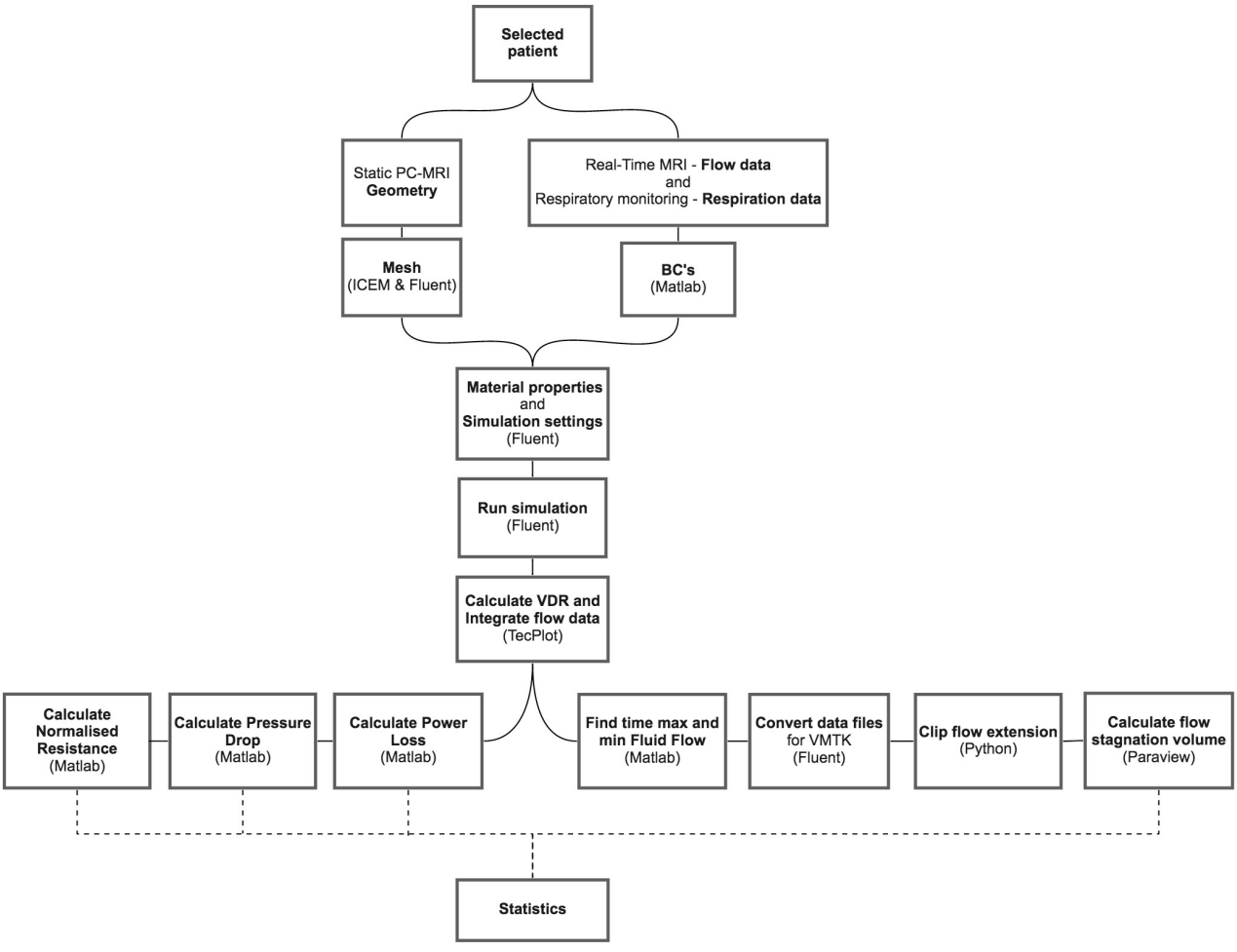

Figure A.1: Technical pipeline.

B

ECTC geometries

Figure B.1: Frontal view of the ECTC geometries of the included patients having a 16mm conduit implanted.

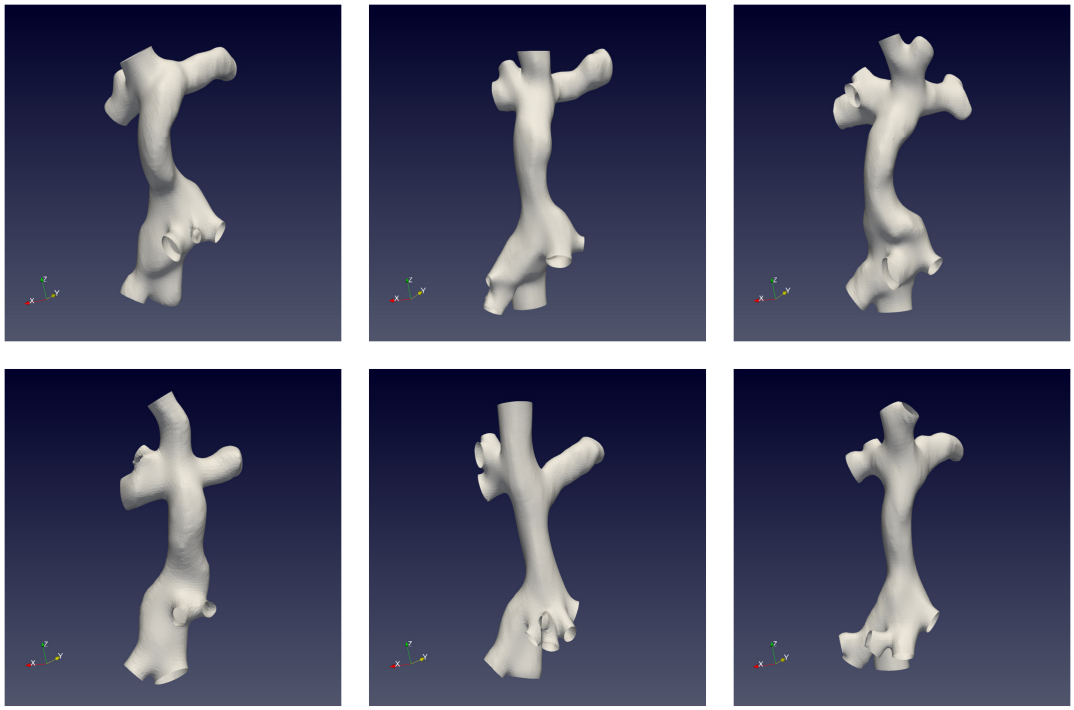

Figure B.2: Frontal view of the ECTC geometries of the included patients having a 18mm conduit implanted.

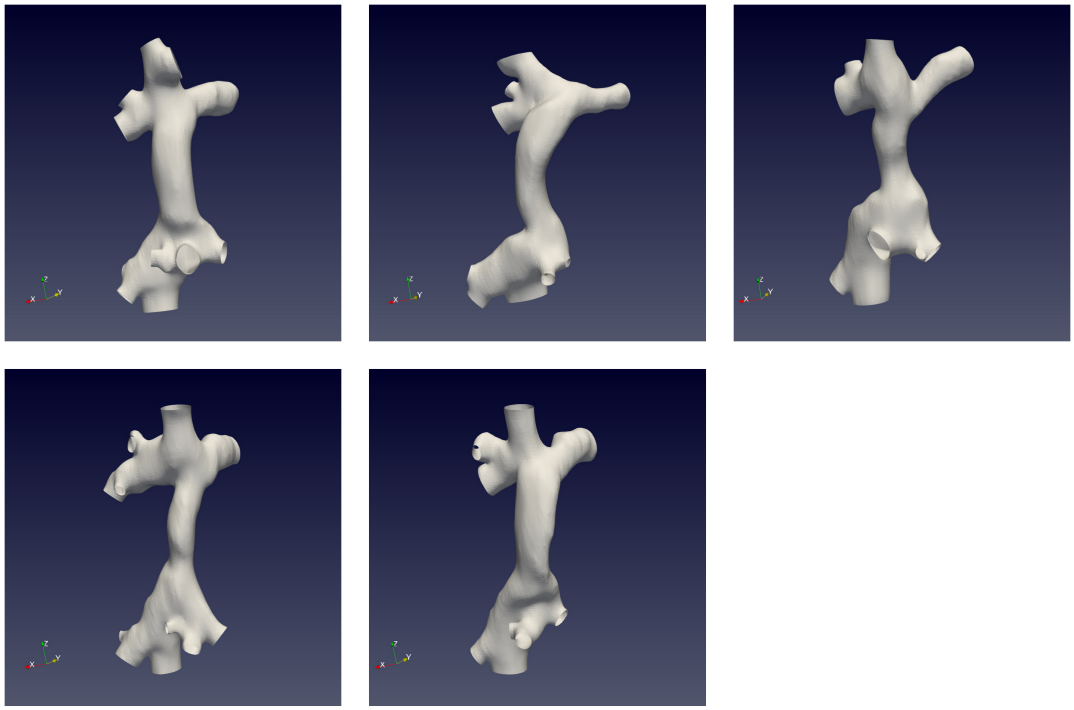

Figure B.3: Frontal view of the ECTC geometries of the included patients having a 20mm conduit implanted.

C

Mesh Independence Study

This mesh independence study is performed previously by the research group and is is performed for one of the included Fontan patients in this master thesis. The maximum element sizes included were calculated from the average diameter vessel divided by 15, 20 and 30. This results in the following mesh types:

- Mesh type 1: 0.8 mm
- Mesh type 2: 0.6 mm
- Mesh type 3: 0.4 mm

It was found that the differences in cross-sectional velocity profiles were small but relevant (see Fig. C.1). Therefore, the simulations are performed with the smallest mesh size.

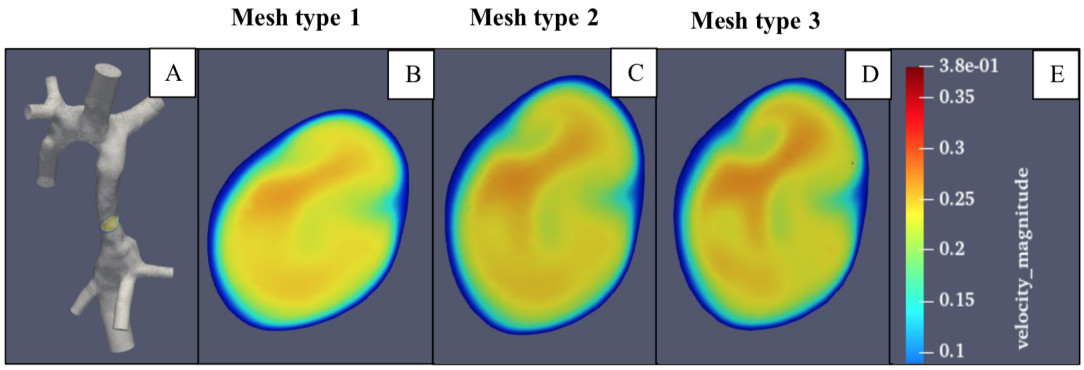

Figure C.1: A: Location of the cross-section in the ECTC geometry. B: Mesh type 1. C: Mesh type 2. D: Mesh type 3. E: Velocity magnitude [m/s] scale.

D

Matlab Codes

D.1. Create velocity profiles (exercise)

```
%% Inlet flow velocity profiles - Fourier Coefficients (exercise condition)
% This Matlab file creates the Fourier coefficients from the inlet
% velocities needed as boundary conditions  of the inlet vessels
% in Computational Fluid Dynamics for the Top Flow project.

%% Read data
ICEM_name = 'ICEM_Data.xlsx';
ParamFile = 'Case_XX_Param_Exc';
sheet = 1;
HV_Range = 'C3:C11';
IVC_Range = 'C13:C17';
SVC_Range = 'C19:C23';
RPA_Range = 'C25:C29';
LPA_Range = 'C31:C35';

HV = nonzeros(xlsread(ICEM_name, sheet, HV_Range));
IVC = nonzeros(xlsread(ICEM_name, sheet, IVC_Range));
SVC = nonzeros(xlsread(ICEM_name, sheet, SVC_Range));
RPA = nonzeros(xlsread(ICEM_name, sheet, RPA_Range));
LPA = nonzeros(xlsread(ICEM_name, sheet, LPA_Range));

T = 1/496;
Fs = 1/T;

clear ICEM_name sheet HV_Range IVC_Range SVC_Range RPA_Range LPA_Range;

%% Ratio's
% Calculate area ratios
HV_ratio = HV/sum(HV);
IVC_ratio = IVC/sum(IVC);
SVC_ratio = SVC/sum(SVC);
RPA_ratio = RPA/sum(RPA);
LPA_ratio = LPA/sum(LPA);

% Ensures that the ratio of single matrixes are actually 1
if length(HV_ratio) == 1
    HV_ratio = 1;
end
if length(IVC_ratio) == 1
    IVC_ratio = 1;
end
if length(SVC_ratio) == 1
    SVC_ratio = 1;
end
if length(RPA_ratio) == 1
    RPA_ratio = 1;
```

```
end
if length(LPA_ratio) == 1
    LPA_ratio = 1;
end

%% Read mat files
load mean_IVC.mat
load mean_SVC.mat
load mean_tunnel.mat

load calc_IVC.mat
load calc_SVC.mat
load calc_tunnel.mat

load full_IVC.mat
load full_SVC.mat
load full_tunnel.mat

% Average inspiration and expiration is calculated
avg_insp = round((max_point_IVC + max_point_SVC + max_point_tunnel)/3);
avg_exp = round((length(t_avg_IVC) + length(t_avg_SVC) + length(t_avg_tunnel))/3) - avg_insp;

%% Interpolating time vector
t_IVC_insp = t_avg_IVC(1:max_point_IVC);
t_IVC_exp = t_avg_IVC(max_point_IVC+1:end);
t_SVC_insp = t_avg_SVC(1:max_point_SVC);
t_SVC_exp = t_avg_SVC(max_point_SVC+1:end);
t_tunnel_insp = t_avg_tunnel(1:max_point_tunnel);
t_tunnel_exp = t_avg_tunnel(max_point_tunnel+1:end);

t_avg_insp = linspace(T, avg_insp*T, avg_insp);
t_avg_exp = t_avg_insp(end) + linspace(T, avg_exp*T, avg_exp);

t_avg = [t_avg_insp, t_avg_exp];

t1_IVC_insp = linspace(t_avg_insp(1), t_avg_insp(end), length(t_IVC_insp));
t1_IVC_exp = linspace(t_avg_exp(1), t_avg_exp(end), length(t_IVC_exp));
t1_SVC_insp = linspace(t_avg_insp(1), t_avg_insp(end), length(t_SVC_insp));
t1_SVC_exp = linspace(t_avg_exp(1), t_avg_exp(end), length(t_SVC_exp));
t1_tunnel_insp = linspace(t_avg_insp(1), t_avg_insp(end), length(t_tunnel_insp));
t1_tunnel_exp = linspace(t_avg_exp(1), t_avg_exp(end), length(t_tunnel_exp));

%% Interpolating respiration vector
phys_IVC_insp = phys_avg_IVC(1:max_point_IVC);
phys_IVC_exp = phys_avg_IVC(max_point_IVC+1:end);
phys_SVC_insp = phys_avg_SVC(1:max_point_SVC);
phys_SVC_exp = phys_avg_SVC(max_point_SVC+1:end);
phys_tunnel_insp = phys_avg_tunnel(1:max_point_tunnel);
phys_tunnel_exp = phys_avg_tunnel(max_point_tunnel+1:end);

phys_avg_insp_IVC = pchip(t1_IVC_insp, phys_IVC_insp, t_avg_insp);
phys_avg_exp_IVC = pchip(t1_IVC_exp, phys_IVC_exp, t_avg_exp);
phys_avg_insp_SVC = pchip(t1_SVC_insp, phys_SVC_insp, t_avg_insp);
phys_avg_exp_SVC = pchip(t1_SVC_exp, phys_SVC_exp, t_avg_exp);
phys_avg_insp_tunnel = pchip(t1_tunnel_insp, phys_tunnel_insp, t_avg_insp);
phys_avg_exp_tunnel = pchip(t1_tunnel_exp, phys_tunnel_exp, t_avg_exp);

phys_avg_IVC = [phys_avg_insp_IVC, phys_avg_exp_IVC];
phys_avg_SVC = [phys_avg_insp_SVC, phys_avg_exp_SVC];
phys_avg_tunnel = [phys_avg_insp_tunnel, phys_avg_exp_tunnel];

%% Interpolating flow vector and include exercise condition
Q_IVC_insp = Q_avg_IVC(1:max_point_IVC);
Q_IVC_exp = Q_avg_IVC(max_point_IVC+1:end);
Q_SVC_insp = Q_avg_SVC(1:max_point_SVC);
Q_SVC_exp = Q_avg_SVC(max_point_SVC+1:end);
Q_tunnel_insp = Q_avg_tunnel(1:max_point_tunnel);
Q_tunnel_exp = Q_avg_tunnel(max_point_tunnel+1:end);

Q_avg_insp_IVC = pchip(t1_IVC_insp, Q_IVC_insp, t_avg_insp);
Q_avg_exp_IVC = pchip(t1_IVC_exp, Q_IVC_exp, t_avg_exp);
```

```
Q_avg_insp_SVC = pchip(t1_SVC_insp, Q_SVC_insp, t_avg_insp);
Q_avg_exp_SVC = pchip(t1_SVC_exp, Q_SVC_exp, t_avg_exp);
Q_avg_insp_tunnel = pchip(t1_tunnel_insp, Q_tunnel_insp, t_avg_insp);
Q_avg_exp_tunnel = pchip(t1_tunnel_exp, Q_tunnel_exp, t_avg_exp);

Insp_fraction_rest = length(Q_avg_insp_IVC)/(length(Q_avg_insp_IVC)...
    +length(Q_avg_exp_IVC)); %inspiratory fraction rest
Exp_fraction_rest = length(Q_avg_exp_IVC)/(length(Q_avg_insp_IVC)...
    +length(Q_avg_exp_IVC));   %expiratory fraction rest

l_IVC_insp = length(Q_avg_insp_IVC); %length inspiration rest
l_IVC_exp = length(Q_avg_exp_IVC);   %length inspiration rest

Insp_fraction_exc = Insp_fraction_rest * 1.17; %inspiratory fraction exc
Exp_fraction_exc = 1 - Insp_fraction_exc;      %expiratory fraction exc

%length inspiration exercise
l_exc_IVC_insp = round((l_IVC_insp*Insp_fraction_exc)/Insp_fraction_rest);

%length expiration exercise
l_exc_IVC_exp = round((l_IVC_exp*Exp_fraction_exc)/Exp_fraction_rest);

y_IVC = (l_exc_IVC_insp+l_exc_IVC_exp)/((l_IVC_insp+l_IVC_exp)/1.6);

t_IVC_insp_exc = linspace(T, t_avg_insp(end), l_exc_IVC_insp/y_IVC);
t_IVC_exp_exc = linspace(T+t_IVC_insp_exc(end), t_avg_exp(end),l_exc_IVC_exp/y_IVC);

Q_avg_insp_IVC_exc = pchip(t_avg_insp, Q_avg_insp_IVC, t_IVC_insp_exc);
Q_avg_exp_IVC_exc = pchip(t_avg_exp, Q_avg_exp_IVC, t_IVC_exp_exc);

Q_avg_IVC_exc = [Q_avg_insp_IVC_exc, Q_avg_exp_IVC_exc];

l_SVC_insp = length(Q_avg_insp_SVC);
l_SVC_exp = length(Q_avg_exp_SVC);
%length inspiration exercise
l_exc_SVC_insp = round((l_SVC_insp*Insp_fraction_exc)/Insp_fraction_rest);
%length expiration exercise
l_exc_SVC_exp = round((l_SVC_exp*Exp_fraction_exc)/Exp_fraction_rest);
y_SVC = (l_exc_SVC_insp+l_exc_SVC_exp)/((l_SVC_insp+l_SVC_exp)/1.6);

t_SVC_insp_exc = linspace(T, t_avg_insp(end), l_exc_SVC_insp/y_SVC);
t_SVC_exp_exc = linspace(T+t_SVC_insp_exc(end), t_avg_exp(end),...
    l_exc_SVC_exp/y_SVC);

Q_avg_insp_SVC_exc = pchip(t_avg_insp, Q_avg_insp_SVC, t_SVC_insp_exc);
Q_avg_exp_SVC_exc = pchip(t_avg_exp, Q_avg_exp_SVC, t_SVC_exp_exc);

Q_avg_SVC_exc = [Q_avg_insp_SVC_exc, Q_avg_exp_SVC_exc];

l_tunnel_insp = length(Q_avg_insp_tunnel);
l_tunnel_exp = length(Q_avg_exp_tunnel);
l_exc_tunnel_insp = round((l_tunnel_insp*Insp_fraction_exc)/...
    Insp_fraction_rest); %length inspiration exercise
l_exc_tunnel_exp = round((l_tunnel_exp*Exp_fraction_exc)/...
    Exp_fraction_rest); %length expiration exercise
y_tunnel = (l_exc_tunnel_insp+l_exc_tunnel_exp)/...
    ((l_tunnel_insp+l_tunnel_exp)/1.6);

t_tunnel_insp_exc = linspace(T, t_avg_insp(end), l_exc_tunnel_insp/y_tunnel);
t_tunnel_exp_exc = linspace(T+t_tunnel_insp_exc(end), t_avg_exp(end), l_exc_tunnel_exp/y_tunnel);

Q_avg_insp_tunnel_exc = pchip(t_avg_insp, Q_avg_insp_tunnel, t_tunnel_insp_exc);
Q_avg_exp_tunnel_exc = pchip(t_avg_exp, Q_avg_exp_tunnel, t_tunnel_exp_exc);

Q_avg_tunnel_exc = [Q_avg_insp_tunnel_exc, Q_avg_exp_tunnel_exc];
t_avg_exc = linspace(T, length(Q_avg_tunnel_exc)*T, length(Q_avg_tunnel_exc));
t_avg_insp_exc = t_avg_exc(1:length(Q_avg_insp_tunnel_exc));
t_avg_exp_exc = t_avg_exc(length(Q_avg_insp_tunnel_exc):length(Q_avg_exp_tunnel_exc)+...
    length(Q_avg_insp_tunnel_exc)-1);

Q_avg_IVC = [Q_avg_insp_IVC, Q_avg_exp_IVC];
```

```
Q_avg_SVC = [Q_avg_insp_SVC, Q_avg_exp_SVC];
Q_avg_tunnel = [Q_avg_insp_tunnel, Q_avg_exp_tunnel];

mean_IVC_exc    = 2.4375*mean(Q_avg_IVC_exc);
mean_tunnel_exc = 2.4375*mean(Q_avg_tunnel_exc);
mean_SVC_exc    = 1.6667*mean(Q_avg_SVC_exc);

Q_avg_IVC_exc       = Q_avg_IVC_exc - mean(Q_avg_IVC_exc) + mean_IVC_exc;
Q_avg_insp_IVC_exc  = Q_avg_IVC_exc(1:length(Q_avg_insp_tunnel_exc));
Q_avg_exp_IVC_exc   = Q_avg_IVC_exc(length(Q_avg_insp_tunnel_exc)+1:...
    length(Q_avg_exp_tunnel_exc)+length(Q_avg_insp_tunnel_exc));

Q_avg_tunnel_exc       = Q_avg_tunnel_exc - mean(Q_avg_tunnel_exc) + mean_tunnel_exc;
Q_avg_insp_tunnel_exc  = Q_avg_tunnel_exc(1:length(Q_avg_insp_tunnel_exc));
Q_avg_exp_tunnel_exc   = Q_avg_tunnel_exc(length(Q_avg_insp_tunnel_exc)+1:...
    length(Q_avg_exp_tunnel_exc)+length(Q_avg_insp_tunnel_exc));

Q_avg_SVC_exc       = Q_avg_SVC_exc - mean(Q_avg_SVC_exc) + mean_SVC_exc;
Q_avg_insp_SVC_exc  = Q_avg_SVC_exc(1:length(Q_avg_insp_tunnel_exc));
Q_avg_exp_SVC_exc   = Q_avg_SVC_exc(length(Q_avg_insp_tunnel_exc)+1:...
    length(Q_avg_exp_tunnel_exc)+length(Q_avg_insp_tunnel_exc));

% Extract min / max inlet flow
Q_avg_inlets = (Q_avg_SVC.*-1) + Q_avg_tunnel;
Q_avg_inlets_exc = (Q_avg_SVC_exc.*-1) + Q_avg_tunnel_exc;

[max_inlets,I_max_inlets] = max(Q_avg_inlets);
I_time_max_inlets = t_avg(end) + t_avg(I_max_inlets);

[max_inlets_exc,I_max_inlets_exc] = max(Q_avg_inlets_exc);
I_time_max_inlets_exc = t_avg_exc(end) + t_avg_exc(I_max_inlets_exc);

% Rename flow signals
Q_avg_IVC = Q_avg_IVC_exc;
Q_avg_SVC = Q_avg_SVC_exc;
Q_avg_tunnel = Q_avg_tunnel_exc;

Increase_insp_fraction = Insp_fraction_exc/Insp_fraction_rest;
%% Clearing variables from workspace
clear avg_exp avg_insp

%% Calculating HV flow
phys_avg_HV = phys_avg_tunnel - phys_avg_IVC;
phys_avg_insp_HV = phys_avg_insp_tunnel - phys_avg_insp_IVC;
phys_avg_exp_HV = phys_avg_exp_tunnel - phys_avg_exp_IVC;

Q_avg_HV = Q_avg_tunnel - Q_avg_IVC;
Q_avg_insp_HV = Q_avg_insp_tunnel - Q_avg_insp_IVC;
Q_avg_exp_HV = Q_avg_exp_tunnel - Q_avg_exp_IVC;

%% Splitting flow curves in ratios
% Initiate matrixes
Q_HV_ratiod = zeros(length(Q_avg_HV), length(HV_ratio));
Q_IVC_ratiod = zeros(length(Q_avg_IVC), length(IVC_ratio));
Q_SVC_ratiod = zeros(length(Q_avg_SVC), length(SVC_ratio));

for i = 1:length(Q_avg_HV)
    Q_HV_ratiod(i, :) = Q_avg_HV(i)*HV_ratio;
end

for i = 1:length(Q_avg_IVC)
    Q_IVC_ratiod(i, :) = Q_avg_IVC(i)*IVC_ratio;
end

for i = 1:length(Q_avg_SVC)
    Q_SVC_ratiod(i, :) = Q_avg_SVC(i)*SVC_ratio;
end

%% Fourier transfer
n = 9; % Number of times to replicate
```

```
t_avg_rep = linspace(T, n*t_avg_exc(end), n*length(t_avg_exc))';
Q_HV_rep = repmat(Q_HV_ratiod, [n, 1]);
Q_IVC_rep = repmat(Q_IVC_ratiod, [n, 1]);
Q_SVC_rep = repmat(Q_SVC_ratiod, [n, 1]);
[L, W_HV] = size(Q_HV_rep);
[L, W_SVC] = size(Q_SVC_rep);
[L, W_IVC] = size(Q_IVC_rep);
metric_conv = ones(18, 1).*10^-6;
metric_conv(18, 1) = 1;


% Settings for Fourier fit
opt = fitoptions('Method', 'NonlinearLeastSquares');
typ = fittype('fourier8');

% Fitting of HV
for i = 1:W_HV
    [temp_fit, temp_gof] = fit(t_avg_rep, Q_HV_rep(:, i), typ, opt);
    HV_fit.(matlab.lang.makeValidName(['HV' num2str(i)])) = temp_fit;
    HV_gof.(matlab.lang.makeValidName(['HV' num2str(i)])) = temp_gof;
    HV_coeff.(matlab.lang.makeValidName(['HV' num2str(i)])) = sum(eye(18).*...
        (metric_conv*coeffvalues(temp_fit)), 1)';
end

% Fitting of SVC
for i = 1:W_SVC
    [temp_fit, temp_gof] = fit(t_avg_rep, Q_SVC_rep(:, i), typ, opt);
    SVC_fit.(matlab.lang.makeValidName(['SVC' num2str(i)])) = temp_fit;
    SVC_gof.(matlab.lang.makeValidName(['SVC' num2str(i)])) = temp_gof;
    SVC_coeff.(matlab.lang.makeValidName(['SVC' num2str(i)])) = sum(eye(18).*...
        (metric_conv*coeffvalues(temp_fit)), 1)';
end

% Fitting of IVC
for i = 1:W_IVC
    [temp_fit, temp_gof] = fit(t_avg_rep, Q_IVC_rep(:, i), typ, opt);
    IVC_fit.(matlab.lang.makeValidName(['IVC' num2str(i)])) = temp_fit;
    IVC_gof.(matlab.lang.makeValidName(['IVC' num2str(i)])) = temp_gof;
    IVC_coeff.(matlab.lang.makeValidName(['IVC' num2str(i)])) = sum(eye(18).*...
        (metric_conv*coeffvalues(temp_fit)), 1)';
end

coeff_names = coeffnames(temp_fit)';

% Create table containing the Fourier coefficients
HV_table = struct2table(HV_coeff, 'RowNames', coeff_names);
SVC_table = struct2table(SVC_coeff, 'RowNames', coeff_names);
IVC_table = struct2table(IVC_coeff, 'RowNames', coeff_names);

isteken = strings(1, 18);
isteken(1:18) = '=';
isteken = isteken';
semiteken = strings(1, 18);
semiteken(1:18) = ';';
semiteken = semiteken';

sizeHV = size(HV_table);
sizeIVC = size(IVC_table);
sizeSVC = size(SVC_table);

HV_table = addvars(HV_table, semiteken, 'After', sizeHV(2));
SVC_table = addvars(SVC_table, semiteken, 'After', sizeSVC(2));
IVC_table = addvars(IVC_table, semiteken, 'After', sizeIVC(2));

HV_table = addvars(HV_table, isteken, 'Before', 1);
SVC_table = addvars(SVC_table, isteken, 'Before', 1);
IVC_table = addvars(IVC_table, isteken, 'Before', 1);

%% Save tables
filename = 'Fourier_Coefficients_exc.xlsx';
writetable(HV_table, filename, 'Sheet', 1, 'WriteRowNames', 1)
```

```
writetable(SVC_table, filename, 'Sheet', 2, 'WriteRowNames', 1)
writetable(IVC_table, filename, 'Sheet', 3, 'WriteRowNames', 1);
```

D.2. Create User Defined Function (exercise)

```
%% Automatisation of creating the UDF file (exercise condition)
% This Matlab file creates autoamtically the UDF file for the Top Flow proect
% with the use of Fourier Coefficients. The resulting file can be used for
% Computational Fluid Dynamics in Ansys Fluent.

%% Make sure to adapt this part to the right case numer and file names
casenr = ...;

ICEM_name = 'ICEM_Data.xlsx';
Fourier_name = 'Fourier_Coefficients_exc.xlsx';
filename = ['Veloc' num2str(casenr) '_resp_exc.c'];

%% Extract vein areas and number of veins
sheet = 1;
HV_Range = 'C3:C11';
IVC_Range = 'C13:C17';
SVC_Range = 'C19:C23';

HV_area  = nonzeros(xlsread(ICEM_name, sheet, HV_Range));
IVC_area = nonzeros(xlsread(ICEM_name, sheet, IVC_Range));
SVC_area = nonzeros(xlsread(ICEM_name, sheet, SVC_Range));

n_HV  = length(HV_area);
n_IVC = length(IVC_area);
n_SVC = length(SVC_area);

%% Extract curve parameter matrices from ICEM for IVC, SVC & HVs
IVC_curve = zeros(n_IVC, 5);
for ii = 1:n_IVC
[temp1, IVC1] = xlsread(ICEM_name, sheet, ['D' num2str(12+ii)]);
IVC1 = cell2mat(IVC1);
IVC1_cleared = regexprep(IVC1, '[Length, Radius, Cr, =]', ' ');
IVC1_cleared = strsplit(IVC1_cleared);
IVC1_vector = str2double(IVC1_cleared);
IVC1_vector = IVC1_vector(2:end);
IVC_curve(ii,:) = IVC1_vector;
end

SVC_curve = zeros(n_SVC, 5);
for ii = 1:n_SVC
[temp1, SVC1] = xlsread(ICEM_name, sheet, ['D' num2str(18+ii)]);
SVC1 = cell2mat(SVC1);
SVC1_cleared = regexprep(SVC1, '[Length, Radius, Cr, =]', ' ');
SVC1_cleared = strsplit(SVC1_cleared);
SVC1_vector = str2double(SVC1_cleared);
SVC1_vector = SVC1_vector(2:end);
SVC_curve(ii,:) = SVC1_vector;
end

HV_curve = zeros(n_HV, 5);
for ii = 1:n_HV
[temp1, HV1] = xlsread(ICEM_name, sheet, ['D' num2str(2+ii)]);
HV1 = cell2mat(HV1);
HV1_cleared = regexprep(HV1, '[Length, Radius, Cr, =]', ' ');
HV1_cleared = strsplit(HV1_cleared);
HV1_vector = str2double(HV1_cleared);
HV1_vector = HV1_vector(2:end);
HV_curve(ii,:) = HV1_vector;
end

%% Extract Fourier coefficients
HV_sheet  = 1;
SVC_sheet = 2;
IVC_sheet = 3;

IVC_coef = xlsread(Fourier_name, IVC_sheet);
SVC_coef = xlsread(Fourier_name, SVC_sheet);
```

```
SVC_coef = [SVC_coef(1:end-1, 1:n_SVC).*-1; SVC_coef(end, 1:n_SVC)];
HV_coef = xlsread(Fourier_name, HV_sheet);

%% Write UDF
%Standard text
fid = fopen(filename,'wt');
fprintf(fid, '/**********************************************************************/\n');
fprintf(fid, ['/* Unsteady_parabolic velocity profile - veloc_' num2str(casenr)  '_respiration\n']);
fprintf(fid, '*/\n');
fprintf(fid, '/* UDFs for specifying time dependent, parabolic velocity profile boundary condition\n');
fprintf(fid, '*/\n');
fprintf(fid, '/*made by S.F.S. van der Woude */\n');
fprintf(fid, '/**********************************************************************/\n');
fprintf(fid, '#include "udf.h"\n');
fprintf(fid, '\n');


%% IVC
for ii = 1:n_IVC
    fid = fopen(filename,'a+');

    fprintf(fid, ['DEFINE_PROFILE(IVC_' num2str(ii) '_unsteady,thread,position)\n']);
    fprintf(fid,  '{\n');
    fprintf(fid,  'real A,Q;\n');
    fprintf(fid,  'real x,y,z;\n');
    fprintf(fid,  'real posvec[ND_ND]; /* this will hold the position vector */\n');
    fprintf(fid,  'real x0,y0,z0;\n');
    fprintf(fid,  'real vmean,vmax;\n');
    fprintf(fid,  'real pi,r,r2,w,T;\n');
    fprintf(fid,  'real a0,a1,b1,a2,b2,a3,b3,a4,b4,a5,b5,a6,b6,a7,b7,a8,b8;/*Fourier coeffiecients*/\n');
    fprintf(fid,  'real flow_time;\n');
    fprintf(fid,  'face_t f;\n');
    fprintf(fid,  'f=0;\n');
    fprintf(fid,  'pi= 3.14159265358979;\n');
    fprintf(fid,  '#if !RP_HOST /*SERIAL or NODE*/\n');
    fprintf(fid,  'flow_time = RP_Get_Real("flow-time");\n');
    fprintf(fid,  '\n');
    fprintf(fid,  '/************************************************************/\n');
    fprintf(fid,  '/* CASE SPECIFIC PARAMETERS\n');
    fprintf(fid,  'MAKE SURE TO ADAPT TO THE CURRENT CASE */\n');
    fprintf(fid,  ['A = ' num2str(IVC_area(ii),'%.6f') 'e-6; /* inlet area (m^2) */\n']);
    fprintf(fid,  ['x0 = ' num2str(IVC_curve(ii,3),'%.6f') 'e-3; /* x coordinate of inlet center */\n']);
    fprintf(fid,  ['y0 = ' num2str(IVC_curve(ii,4),'%.6f') 'e-3; /* y coordinate of inlet center */\n']);
    fprintf(fid,  ['z0 = ' num2str(IVC_curve(ii,5),'%.6f') 'e-3; /* z coordinate of inlet center */\n']);
    fprintf(fid,  '/************************************************************/\n');
    fprintf(fid,  '\n');
    fprintf(fid,  '/*Fourier series, order 8*/\n');
    fprintf(fid,  ['\t a0   =   ' num2str(IVC_coef(1,ii), '%.15f') ';\n']);
    fprintf(fid,  ['\t a1   =   ' num2str(IVC_coef(2,ii), '%.15f') ';\n']);
    fprintf(fid,  ['\t b1   =   ' num2str(IVC_coef(3,ii), '%.15f') ';\n']);
    fprintf(fid,  ['\t a2   =   ' num2str(IVC_coef(4,ii), '%.15f') ';\n']);
    fprintf(fid,  ['\t b2   =   ' num2str(IVC_coef(5,ii), '%.15f') ';\n']);
    fprintf(fid,  ['\t a3   =   ' num2str(IVC_coef(6,ii), '%.15f') ';\n']);
    fprintf(fid,  ['\t b3   =   ' num2str(IVC_coef(7,ii), '%.15f') ';\n']);
    fprintf(fid,  ['\t a4   =   ' num2str(IVC_coef(8,ii), '%.15f') ';\n']);
    fprintf(fid,  ['\t b4   =   ' num2str(IVC_coef(9,ii), '%.15f') ';\n']);
    fprintf(fid,  ['\t a5   =   ' num2str(IVC_coef(10,ii), '%.15f') ';\n']);
    fprintf(fid,  ['\t b5   =   ' num2str(IVC_coef(11,ii), '%.15f') ';\n']);
    fprintf(fid,  ['\t a6   =   ' num2str(IVC_coef(12,ii), '%.15f') ';\n']);
    fprintf(fid,  ['\t b6   =   ' num2str(IVC_coef(13,ii), '%.15f') ';\n']);
    fprintf(fid,  ['\t a7   =   ' num2str(IVC_coef(14,ii), '%.15f') ';\n']);
    fprintf(fid,  ['\t b7   =   ' num2str(IVC_coef(15,ii), '%.15f') ';\n']);
    fprintf(fid,  ['\t a8   =   ' num2str(IVC_coef(16,ii), '%.15f') ';\n']);
    fprintf(fid,  ['\t b8   =   ' num2str(IVC_coef(17,ii), '%.15f') ';\n']);
    fprintf(fid,  ['\t w   =   ' num2str(IVC_coef(18,ii), '%.15f') ';\n']);
    fprintf(fid,  '\n');
    fprintf(fid,  'Q = a0 + a1*cos(flow_time*w) + b1*sin(flow_time*w) +a2*cos(2*flow_time*w) +');
    fprintf(fid,  'b2*sin(2*flow_time*w) +a3*cos(3*flow_time*w) + b3*sin(3*flow_time*w)');
    fprintf(fid,  '+a4*cos(4*flow_time*w)+ b4*sin(4*flow_time*w) +a5*cos(5*flow_time*w)');
    fprintf(fid,  '+ b5*sin(5*flow_time*w) +a6*cos(6*flow_time*w) + b6*sin(6*flow_time*w)');
    fprintf(fid,  '+a7*cos(7*flow_time*w) + b7*sin(7*flow_time*w) +a8*cos(8*flow_time*w)');
```

```
    fprintf(fid,  '+ b8*sin(8*flow_time*w);\n');
    fprintf(fid,  'vmean = Q/A;\n');
    fprintf(fid,  'vmax = 2*vmean;\n');
    fprintf(fid,  'r = sqrt(A/pi);\n');
    fprintf(fid,  'r2 = (pow((r),2));\n');
    fprintf(fid,  '\n');
    fprintf(fid,  '/* PARABOLOID-SHAPED VELOCITY PROFILE */\n');
    fprintf(fid,  'begin_f_loop (f,thread)\n');
    fprintf(fid,  '\t \t {\n');
    fprintf(fid,  '\t \t \t F_CENTROID(posvec,f,thread);\n');
    fprintf(fid,  '\t \t \t x=posvec[0];\n');
    fprintf(fid,  '\t \t \t y=posvec[1];\n');
    fprintf(fid,  '\t \t \t z=posvec[2];\n');
    fprintf(fid,  '\n');
    fprintf(fid,  '\t \t \t F_PROFILE(f,thread,position)= - (vmax/r2)*( (pow((x-x0),2))+(pow((y-y0),2))+');
    fprintf(fid,  '(pow((z-z0),2)) ) + vmax;\n');
    fprintf(fid,  '\n');
    fprintf(fid,  '\t \t }\n');
    fprintf(fid,  '\t end_f_loop(f,thread)\n');
    fprintf(fid,  '\n');
    fprintf(fid,  '#endif   /*!RP_HOST*/\n');
    fprintf(fid,  '}\n');
    fprintf(fid,  '\n');
    fprintf(fid,  '\n');

    fclose(fid);
end

%% SVC
for ii = 1:n_SVC
    fid = fopen(filename,'a+');
    fprintf(fid, ['DEFINE_PROFILE(SVC_' num2str(ii) '_unsteady,thread,position)\n']);
    fprintf(fid,  '{\n');
    fprintf(fid,  'real A,Q;\n');
    fprintf(fid,  'real x,y,z;\n');
    fprintf(fid,  'real posvec[ND_ND]; /* this will hold the position vector */\n');
    fprintf(fid,  'real x0,y0,z0;\n');
    fprintf(fid,  'real vmean,vmax;\n');
    fprintf(fid,  'real pi,r,r2,w,T;\n');
    fprintf(fid,  'real a0,a1,b1,a2,b2,a3,b3,a4,b4,a5,b5,a6,b6,a7,b7,a8,b8;/*Fourier coeffiecients*/\n');
    fprintf(fid,  'real flow_time;\n');
    fprintf(fid,  'face_t f;\n');
    fprintf(fid,  'f=0;\n');
    fprintf(fid,  'pi= 3.14159265358979;\n');
    fprintf(fid,  '#if !RP_HOST /*SERIAL or NODE*/\n');
    fprintf(fid,  'flow_time = RP_Get_Real("flow-time");\n');
    fprintf(fid,  '\n');
    fprintf(fid,  '/************************************************************/\n');
    fprintf(fid,  '/* CASE SPECIFIC PARAMETERS\n');
    fprintf(fid,  'MAKE SURE TO ADAPT TO THE CURRENT CASE */\n');
    fprintf(fid,  ['A = ' num2str(SVC_area(ii),'%.6f') 'e-6; /* inlet area (m^2) */\n']);
    fprintf(fid,  ['x0 = ' num2str(SVC_curve(ii,3),'%.6f') 'e-3; /* x coordinate of inlet center */\n']);
    fprintf(fid,  ['y0 = ' num2str(SVC_curve(ii,4),'%.6f') 'e-3; /* y coordinate of inlet center */\n']);
    fprintf(fid,  ['z0 = ' num2str(SVC_curve(ii,5),'%.6f') 'e-3; /* z coordinate of inlet center */\n']);
    fprintf(fid,  '/************************************************************/\n');
    fprintf(fid,  '\n');
    fprintf(fid,  '/*Fourier series, order 8*/\n');
    fprintf(fid,  ['\t a0   =   ' num2str(SVC_coef(1,ii), '%.15f') ';\n']);
    fprintf(fid,  ['\t a1   =   ' num2str(SVC_coef(2,ii), '%.15f') ';\n']);
    fprintf(fid,  ['\t b1   =   ' num2str(SVC_coef(3,ii), '%.15f') ';\n']);
    fprintf(fid,  ['\t a2   =   ' num2str(SVC_coef(4,ii), '%.15f') ';\n']);
    fprintf(fid,  ['\t b2   =   ' num2str(SVC_coef(5,ii), '%.15f') ';\n']);
    fprintf(fid,  ['\t a3   =   ' num2str(SVC_coef(6,ii), '%.15f') ';\n']);
    fprintf(fid,  ['\t b3   =   ' num2str(SVC_coef(7,ii), '%.15f') ';\n']);
    fprintf(fid,  ['\t a4   =   ' num2str(SVC_coef(8,ii), '%.15f') ';\n']);
    fprintf(fid,  ['\t b4   =   ' num2str(SVC_coef(9,ii), '%.15f') ';\n']);
    fprintf(fid,  ['\t a5   =   ' num2str(SVC_coef(10,ii), '%.15f') ';\n']);
    fprintf(fid,  ['\t b5   =   ' num2str(SVC_coef(11,ii), '%.15f') ';\n']);
    fprintf(fid,  ['\t a6   =   ' num2str(SVC_coef(12,ii), '%.15f') ';\n']);
    fprintf(fid,  ['\t b6   =   ' num2str(SVC_coef(13,ii), '%.15f') ';\n']);
    fprintf(fid,  ['\t a7   =   ' num2str(SVC_coef(14,ii), '%.15f') ';\n']);
```

```
    fprintf(fid,  ['\t b7   =   ' num2str(SVC_coef(15,ii), '%.15f') ';\n']);
    fprintf(fid,  ['\t a8   =   ' num2str(SVC_coef(16,ii), '%.15f') ';\n']);
    fprintf(fid,  ['\t b8   =   ' num2str(SVC_coef(17,ii), '%.15f') ';\n']);
    fprintf(fid,  ['\t w   =   ' num2str(SVC_coef(18,ii), '%.15f') ';\n']);
    fprintf(fid,  '\n');
    fprintf(fid,  'Q = a0 + a1*cos(flow_time*w) + b1*sin(flow_time*w) +a2*cos(2*flow_time*w) +');
    fprintf(fid,  'b2*sin(2*flow_time*w) +a3*cos(3*flow_time*w) + b3*sin(3*flow_time*w)');
    fprintf(fid,  '+a4*cos(4*flow_time*w)+ b4*sin(4*flow_time*w) +a5*cos(5*flow_time*w)');
    fprintf(fid,  '+ b5*sin(5*flow_time*w) +a6*cos(6*flow_time*w) + b6*sin(6*flow_time*w)');
    fprintf(fid,  '+a7*cos(7*flow_time*w) + b7*sin(7*flow_time*w) +a8*cos(8*flow_time*w)');
    fprintf(fid,  '+ b8*sin(8*flow_time*w);\n');
    fprintf(fid,  'vmax = 2*vmean;\n');
    fprintf(fid,  'r = sqrt(A/pi);\n');
    fprintf(fid,  'r2 = (pow((r),2));\n');
    fprintf(fid,  '\n');
    fprintf(fid,  '/* PARABOLOID-SHAPED VELOCITY PROFILE */\n');
    fprintf(fid,  'begin_f_loop (f,thread)\n');
    fprintf(fid,  '\t \t {\n');
    fprintf(fid,  '\t \t \t F_CENTROID(posvec,f,thread);\n');
    fprintf(fid,  '\t \t \t x=posvec[0];\n');
    fprintf(fid,  '\t \t \t y=posvec[1];\n');
    fprintf(fid,  '\t \t \t z=posvec[2];\n');
    fprintf(fid,  '\n');
    fprintf(fid,  '\t \t \t F_PROFILE(f,thread,position)= - (vmax/r2)*( (pow((x-x0),2))+(pow((y-y0),2))+')
    fprintf(fid,  '(pow((z-z0),2)) ) + vmax;\n');
    fprintf(fid,  '\n');
    fprintf(fid,  '\t \t }\n');
    fprintf(fid,  '\t end_f_loop(f,thread)\n');
    fprintf(fid,  '\n');
    fprintf(fid,  '#endif   /*!RP_HOST*/\n');
    fprintf(fid,  '}\n');
    fprintf(fid,  '\n');
    fprintf(fid,  '\n');

    fclose(fid);
end

%% HVs
for ii = 1:n_HV
    fid = fopen(filename,'a+');
    fprintf(fid, ['DEFINE_PROFILE(HV_' num2str(ii) '_unsteady,thread,position)\n']);
    fprintf(fid,  '{\n');
    fprintf(fid,  'real A,Q;\n');
    fprintf(fid,  'real x,y,z;\n');
    fprintf(fid,  'real posvec[ND_ND]; /* this will hold the position vector */\n');
    fprintf(fid,  'real x0,y0,z0;\n');
    fprintf(fid,  'real vmean,vmax;\n');
    fprintf(fid,  'real pi,r,r2,w,T;\n');
    fprintf(fid,  'real a0,a1,b1,a2,b2,a3,b3,a4,b4,a5,b5,a6,b6,a7,b7,a8,b8;/*Fourier coeffiecients*/\n');
    fprintf(fid,  'real flow_time;\n');
    fprintf(fid,  'face_t f;\n');
    fprintf(fid,  'f=0;\n');
    fprintf(fid,  'pi= 3.14159265358979;\n');
    fprintf(fid,  '#if !RP_HOST /*SERIAL or NODE*/\n');
    fprintf(fid,  'flow_time = RP_Get_Real("flow-time");\n');
    fprintf(fid,  '\n');
    fprintf(fid,  '/*********************************************************/\n');
    fprintf(fid,  '/* CASE SPECIFIC PARAMETERS\n');
    fprintf(fid,  'MAKE SURE TO ADAPT TO THE CURRENT CASE */\n');
    fprintf(fid,  ['A = ' num2str(HV_area(ii),'%.6f') 'e-6; /* inlet area (m^2) */\n']);
    fprintf(fid,  ['x0 = ' num2str(HV_curve(ii,3),'%.6f') 'e-3; /* x coordinate of inlet center */\n']);
    fprintf(fid,  ['y0 = ' num2str(HV_curve(ii,4), '%.6f') 'e-3; /* y coordinate of inlet center */\n']);
    fprintf(fid,  ['z0 = ' num2str(HV_curve(ii,5), '%.6f') 'e-3; /* z coordinate of inlet center */\n']);
    fprintf(fid,  '/*********************************************************/\n');
    fprintf(fid,  '\n');
    fprintf(fid,  '/*Fourier series, order 8*/\n');
    fprintf(fid,  ['\t a0   =   ' num2str(HV_coef(1,ii), '%.15f') ';\n']);
    fprintf(fid,  ['\t a1   =   ' num2str(HV_coef(2,ii), '%.15f') ';\n']);
    fprintf(fid,  ['\t b1   =   ' num2str(HV_coef(3,ii), '%.15f') ';\n']);
    fprintf(fid,  ['\t a2   =   ' num2str(HV_coef(4,ii), '%.15f') ';\n']);
    fprintf(fid,  ['\t b2   =   ' num2str(HV_coef(5,ii), '%.15f') ';\n']);
```

```
    fprintf(fid,  ['\t a3   =   ' num2str(HV_coef(6,ii), '%.15f') ';\n']);
    fprintf(fid,  ['\t b3   =   ' num2str(HV_coef(7,ii), '%.15f') ';\n']);
    fprintf(fid,  ['\t a4   =   ' num2str(HV_coef(8,ii), '%.15f') ';\n']);
    fprintf(fid,  ['\t b4   =   ' num2str(HV_coef(9,ii), '%.15f') ';\n']);
    fprintf(fid,  ['\t a5   =   ' num2str(HV_coef(10,ii), '%.15f') ';\n']);
    fprintf(fid,  ['\t b5   =   ' num2str(HV_coef(11,ii), '%.15f') ';\n']);
    fprintf(fid,  ['\t a6   =   ' num2str(HV_coef(12,ii), '%.15f') ';\n']);
    fprintf(fid,  ['\t b6   =   ' num2str(HV_coef(13,ii), '%.15f') ';\n']);
    fprintf(fid,  ['\t a7   =   ' num2str(HV_coef(14,ii), '%.15f') ';\n']);
    fprintf(fid,  ['\t b7   =   ' num2str(HV_coef(15,ii), '%.15f') ';\n']);
    fprintf(fid,  ['\t a8   =   ' num2str(HV_coef(16,ii), '%.15f') ';\n']);
    fprintf(fid,  ['\t b8   =   ' num2str(HV_coef(17,ii), '%.15f') ';\n']);
    fprintf(fid,  ['\t w    =   ' num2str(HV_coef(18,ii), '%.15f') ';\n']);
    fprintf(fid,  '\n');
    fprintf(fid,  'Q = a0 + a1*cos(flow_time*w) + b1*sin(flow_time*w) +a2*cos(2*flow_time*w) +');
    fprintf(fid,  'b2*sin(2*flow_time*w) +a3*cos(3*flow_time*w) + b3*sin(3*flow_time*w)');
    fprintf(fid,  '+a4*cos(4*flow_time*w)+ b4*sin(4*flow_time*w) +a5*cos(5*flow_time*w)');
    fprintf(fid,  '+ b5*sin(5*flow_time*w) +a6*cos(6*flow_time*w) + b6*sin(6*flow_time*w)');
    fprintf(fid,  '+a7*cos(7*flow_time*w) + b7*sin(7*flow_time*w) +a8*cos(8*flow_time*w)');
    fprintf(fid,  '+ b8*sin(8*flow_time*w);\n');
    fprintf(fid,  'vmean = Q/A;\n');
    fprintf(fid,  'vmax = 2*vmean;\n');
    fprintf(fid,  'r = sqrt(A/pi);\n');
    fprintf(fid,  'r2 = (pow((r),2));\n');
    fprintf(fid,  '\n');
    fprintf(fid,  '/* PARABOLOID-SHAPED VELOCITY PROFILE */\n');
    fprintf(fid,  'begin_f_loop (f,thread)\n');
    fprintf(fid,  '\t \t {\n');
    fprintf(fid,  '\t \t \t F_CENTROID(posvec,f,thread);\n');
    fprintf(fid,  '\t \t \t x=posvec[0];\n');
    fprintf(fid,  '\t \t \t y=posvec[1];\n');
    fprintf(fid,  '\t \t \t z=posvec[2];\n');
    fprintf(fid,  '\n');
    fprintf(fid,  '\t \t \t F_PROFILE(f,thread,position)= - (vmax/r2)*( (pow((x-x0),2))+(pow((y-y0),2))+');
    fprintf(fid,  '(pow((z-z0),2)) ) + vmax;\n');
    fprintf(fid,  '\n');
    fprintf(fid,  '\t \t }\n');
    fprintf(fid,  '\t end_f_loop(f,thread)\n');
    fprintf(fid,  '\n');
    fprintf(fid,  '#endif   /*!RP_HOST*/\n');
    fprintf(fid,  '}\n');
    fprintf(fid,  '\n');
    fprintf(fid,  '\n');

    fclose(fid);
end
```

D.3. Output analysis (exercise)

```
%% Output Analysis TopFlow (exercise condition)
% Analyses the output files from Tecplot .txt files for the TopFlow project.
% Power loss, pressure drop and normalised resistance are calculated and
% minmum and maximum flow/energy loss is found.

CaseNr = ...;

BSA = ...; % Body Surface Area

TS_end_insp_exc = ...; %Time at end inspiration phase

n_IVC = ...; % Fill in number of vessels
n_SVC = ...;
n_HVL = ...;
n_HVM = ...;
n_HVR = ...;

%% Read fluid
[fluid_flow, Time]  =  Read_output_auto(['Veloc' num2str(CaseNr) '_fluid_flow_exc.txt']); %m3/sec;

%% Read IVC
IVC = [];
if n_IVC == 1
    [IVC_flow, Time]  =  Read_output_auto(['Veloc' num2str(CaseNr) '_IVC_flow_exc.txt']); %m3/sec
    IVC(:,1) = IVC_flow;
elseif n_IVC == 2
    [IVC1_flow, Time]  =  Read_output_auto(['Veloc' num2str(CaseNr) '_IVC1_flow_exc.txt']);
    [IVC2_flow]  =  Read_output_auto(['Veloc' num2str(CaseNr) '_IVC2_flow_exc.txt']);
    IVC(:,1) = IVC1_flow;
    IVC(:,2) = IVC2_flow;
end

%% Read SVC
SVC = [];
if n_SVC == 1
    [SVC_flow]  =  Read_output_auto(['Veloc' num2str(CaseNr) '_SVC_flow_exc.txt']);
    SVC(:,1) = SVC_flow;
elseif n_SVC  == 2
    [SVC1_flow]  =  Read_output_auto(['Veloc' num2str(CaseNr) '_SVC1_flow_exc.txt']);
    [SVC2_flow]  =  Read_output_auto(['Veloc' num2str(CaseNr) '_SVC2_flow_exc.txt']);
    SVC(:,1) = SVC1_flow;
    SVC(:,2) = SVC2_flow;
end

%% Read HVL
HVL = [];
if n_HVL == 1
    [HVL_flow]  =  Read_output_auto(['Veloc' num2str(CaseNr) '_HVL_flow_exc.txt']);
    HVL(:,1) = HVL_flow;
elseif n_HVL == 2
    [HVL1_flow]  =  Read_output_auto(['Veloc' num2str(CaseNr) '_HVL1_flow_exc.txt']);
    [HVL2_flow]  =  Read_output_auto(['Veloc' num2str(CaseNr) '_HVL2_flow_exc.txt']);
    HVL(:,1) = HVL1_flow;
    HVL(:,2) = HVL2_flow;
elseif n_HVL == 3
    [HVL1_flow]  =  Read_output_auto(['Veloc' num2str(CaseNr) '_HVL1_flow_exc.txt']);
    [HVL2_flow]  =  Read_output_auto(['Veloc' num2str(CaseNr) '_HVL2_flow_exc.txt']);
    [HVL3_flow]  =  Read_output_auto(['Veloc' num2str(CaseNr) '_HVL3_flow_exc.txt']);
    HVL(:,1) = HVL1_flow;
    HVL(:,2) = HVL2_flow;
    HVL(:,3) = HVL3_flow;
end

%% Read HVM
HVM = [];
if n_HVM == 1
    [HVM_flow]  =  Read_output_auto(['Veloc' num2str(CaseNr) '_HVM_flow_exc.txt']);
```

```
    HVM(:,1) = HVM_flow;
elseif n_HVM == 2
    [HVM1_flow]  =  Read_output_auto(['Veloc' num2str(CaseNr) '_HVM1_flow_exc.txt']);
    [HVM2_flow]  =  Read_output_auto(['Veloc' num2str(CaseNr) '_HVM2_flow_exc.txt']);
    HVM(:,1) = HVM1_flow;
    HVM(:,2) = HVM2_flow;
elseif n_HVM == 3
    [HVM1_flow]  =  Read_output_auto(['Veloc' num2str(CaseNr) '_HVM1_flow_exc.txt']);
    [HVM2_flow]  =  Read_output_auto(['Veloc' num2str(CaseNr) '_HVM2_flow_exc.txt']);
    [HVM3_flow]  =  Read_output_auto(['Veloc' num2str(CaseNr) '_HVM3_flow_exc.txt']);
    HVM(:,1) = HVM1_flow;
    HVM(:,2) = HVM2_flow;
    HVM(:,3) = HVM3_flow;
end

%% Read HVR
HVR =  [];
if n_HVR == 1
    [HVR_flow]  =  Read_output_auto(['Veloc' num2str(CaseNr) '_HVR_flow_exc.txt']);
    HVR(:,1) = HVR_flow;
elseif n_HVR == 2
    [HVR1_flow]  =  Read_output_auto(['Veloc' num2str(CaseNr) '_HVR1_flow_exc.txt']);
    [HVR2_flow]  =  Read_output_auto(['Veloc' num2str(CaseNr) '_HVR2_flow_exc.txt']);
    HVR(:,1) = HVR1_flow;
    HVR(:,2) = HVR2_flow;
elseif n_HVR == 3
    [HVR1_flow]  =  Read_output_auto(['Veloc' num2str(CaseNr) '_HVR1_flow_exc.txt']);
    [HVR2_flow]  =  Read_output_auto(['Veloc' num2str(CaseNr) '_HVR2_flow_exc.txt']);
    [HVR3_flow]  =  Read_output_auto(['Veloc' num2str(CaseNr) '_HVR3_flow_exc.txt']);
    HVR(:,1) = HVR1_flow;
    HVR(:,2) = HVR2_flow;
    HVR(:,3) = HVR3_flow;
end

%% Time
TS = 1:length(Time);
Time_corrected = Time - Time(1);

[~,I_end_insp] = (min(abs(Time_corrected - TS_end_insp_exc)));

%% Power Loss
[VDR, Time]  =  Read_output_auto(['Veloc' num2str(CaseNr) '_VDR_exc.txt']); %Watt
VDR_mW = VDR*1000;

Mean_VDR_mW = mean(VDR_mW);
Mean_VDR_mW_insp = mean(VDR_mW(1:I_end_insp));
Mean_VDR_mW_exp = mean(VDR_mW(I_end_insp+1:end));

[M_MaxVDR, I_MaxVDR]  = max(VDR_mW);
Time_MaxVDR = Time(I_MaxVDR);
[M_MinVDR, I_MinVDR]  = min(VDR_mW);
Time_MinVDR = Time(I_MinVDR);

%% Inlet Flow
InletFlow = sum(IVC,2) + sum(SVC,2) + sum(HVL,2) + sum(HVM,2) + sum(HVR,2);
InletFlow_Lmin = (InletFlow.*1000000)/1000*60;
FluidFlow_Lmin = (fluid_flow.*1000000)/1000*60;

Mean_InletFlow_Lmin = mean(InletFlow_Lmin);
Mean_InletFlow_Lmin_insp = mean(InletFlow_Lmin(1:I_end_insp));
Mean_InletFlow_Lmin_exp = mean(InletFlow_Lmin(I_end_insp+1:end));

[M_MaxFlow, I_MaxFlow]  = max(InletFlow_Lmin);
Time_MaxFlow = Time(I_MaxFlow);
[M_MinFlow, I_MinFlow]  = min(InletFlow_Lmin);
Time_MinFlow = Time(I_MinFlow);

[M_MaxFluidFlow, I_MaxFluidFlow]  = max(FluidFlow_Lmin);
Time_MaxFluidFlow = Time(I_MaxFluidFlow);
[M_MinFluidFlow, I_MinFluidFlow]  = min(FluidFlow_Lmin);
Time_MinFluidFlow = Time(I_MinFluidFlow);
```

```
%% Pressure drop
Pressure_drop =((Mean_VDR_mW/1000)/((Mean_InletFlow_Lmin/1000000)*1000/60))*(1/133.322);
Pressure_drop_insp = ((Mean_VDR_mW_insp/1000)/((Mean_InletFlow_Lmin_insp/1000000)*1000/60))*(1/133.322);
Pressure_drop_exp = ((Mean_VDR_mW_exp/1000)/((Mean_InletFlow_Lmin_exp/1000000)*1000/60))*(1/133.322);

%% Normalized resistance mmHg/L/min
NormResis = Pressure_drop / (Mean_InletFlow_Lmin / BSA);
NormResis_insp = Pressure_drop_insp / (Mean_InletFlow_Lmin_insp / BSA);
NormResis_exp = Pressure_drop_exp / (Mean_InletFlow_Lmin_exp / BSA);
```

D.3.1. Read automatic output function

```
function [variable, time] = Read_output_auto(input)

fid=fopen(input);

tline = fgetl(fid);
tlines = cell(0,1);
while ischar(tline)
    tlines{end+1,1} = tline;
    tline = fgetl(fid);
end
fclose(fid);

tlines_vector = [];
for ii=3:502
tlines1 = cell2mat(tlines(ii));
tlines_cleared = strsplit(tlines1);
tlines_vector(ii-2,:) = str2double(tlines_cleared);
end

time  = tlines_vector(:,1);
variable =  tlines_vector(:,2);
end
```

E

Validation CFD model

Table E.1: Validation results of the used CFD model. Results are given for all included patients in a resting and exercise condition. A: Average LPA flow measured with real-time MRI, before phase-shifting and interpolating the data. B: Average measured LPA flow with real-time MRI, after phase-shifting and interpolating the data. C: Average computed LPA flow with CFD model.

Patient + condition	**A** [m^3/s]	**B** [m^3/s]	**C** [m^3/s]	**Difference A&C** [%]	**Difference B&C** [%]
2 rest	3.78e-5	3.92e-5	3.92e-5	3.7	0.0
2 exercise	-	9.01e-5	9.02e-5	-	0.1
4 rest (LPA1)	2.16e-5	2.18e-5	2.18e-5	0.9	0.0
4 exercise (LPA1)	-	4.91e-5	4.91e-5	-	0.0
4 rest (LPA2)	3.66e-5	3.70e-5	3.70e-5	1.1	0.0
4 exercise (LPA2)	-	8.34e-5	8.34e-5	-	0.0
7 rest	3.39e-5	3.33e-05	3.34e-5	1.5	0.3
7 exercise	-	7.88e-05	7.89e-5	-	0.1
9 rest	2.07e-5	2.04e-5	2.04e-5	1.4	0.0
9 exercise	-	4.67e-05	4.67e-05	-	0.0
14 rest	5.15e-5	5.20e-5	5.19e-5	0.8	0.2
14 exercise	-	11.96e-5	11.95e-5	-	0.1
20 rest	1.69e-5	1.70e-5	1.70e-5	0.6	0.0
20 exercise	-	3.87e-5	3.87e-5	-	0.0
21 rest	3.45e-5	3.45e-5	3.45e-5	0.0	0.0
21 exercise	-	8.10e-5	8.11e-5	-	0.1
34 rest	3.79e-5	3.78e-5	3.78e-5	0.3	0.0
34 exercise	-	8.72e-5	-	-	-
38 rest	4.46e-5	4.60e-5	4.60e-5	3.1	0.0
38 exercise	-	10.52e-5	10.52e-5	-	0.0
39 rest	2.88e-5	3.04e-5	3.05e-5	5.9	0.3
39 exercise	-	7.33e-5	7.33e-5	-	0.0
41 rest	3.23e-5	3.19e-5	3.19e-5	1.2	0.0
41 exercise	-	7.16e-5	7.16e-5	-	0.0
42 rest	3.52e-5	3.48e-5	3.48e-5	1.1	0.0
42 exercise	-	8.09e-5	8.09e-5	-	0.0
43 rest	2.40e-5	2.45e-5	2.45e-5	2.1	0.0
43 exercise	-	5.87e-5	5.87e-5	-	0.0
44 rest	1.59e-5	1.60e-5	1.60e-5	0.6	0.0
44 exercise	-	3.48e-5	3.48e-5	-	0.0
50 rest	1.78e-5	1.92e-5	1.92e-5	7.8	0.0
50 exercise	-	4.41e-5	4.41e-5	-	0.0
51 rest	2.28e-5	2.27e-5	2.27e-5	0.4	0.0

Table E.1 continued from previous page

Patient + condition	A [m^3/s]	B [m^3/s]	C [m^3/s]	Difference A&C [%]	Difference B&C [%]
51 exercise	-	5.25e-5	5.25e-5	-	0.0
53 rest	4.37e-5	4.28e-5	4.28e-5	2.1	0.0
53 exercise	-	9.70e-5	9.71e-5	-	0.1
55 rest	4.66e-5	4.62e-5	4.62e-5	0.9	0.0
55 exercise	-	10.3e-5	10.3e-5	-	0.0
56 rest	2.23e-5	2.25e-5	2.25e-5	0.9	0.0
56 exercise	-	5.24e-5	-	-	-

F

Statistics

F.1. General Results

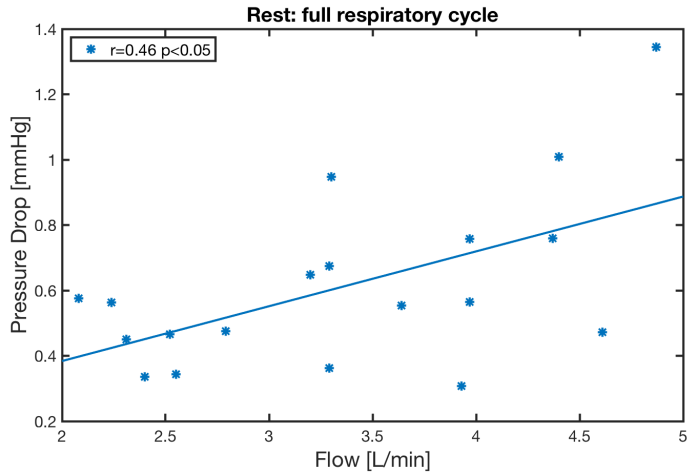

Figure F.1: Pressure drop related to the averaged real-time tunnel flow in a resting condition for the full respiratory cycle.

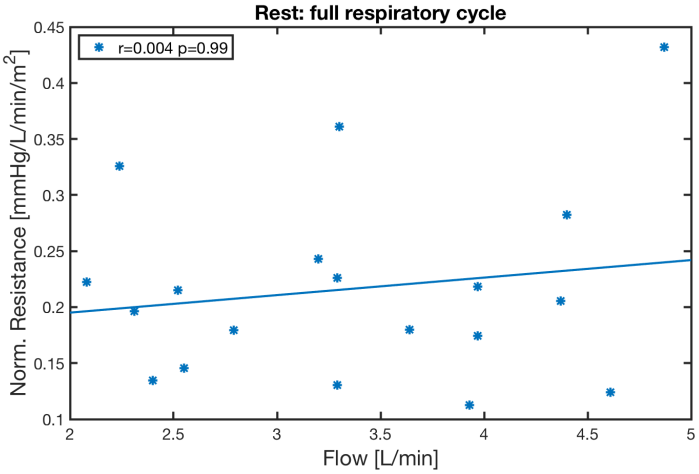

Figure F.2: Normalised resistance related to the averaged real-time tunnel flow in a resting condition for the full respiratory cycle.

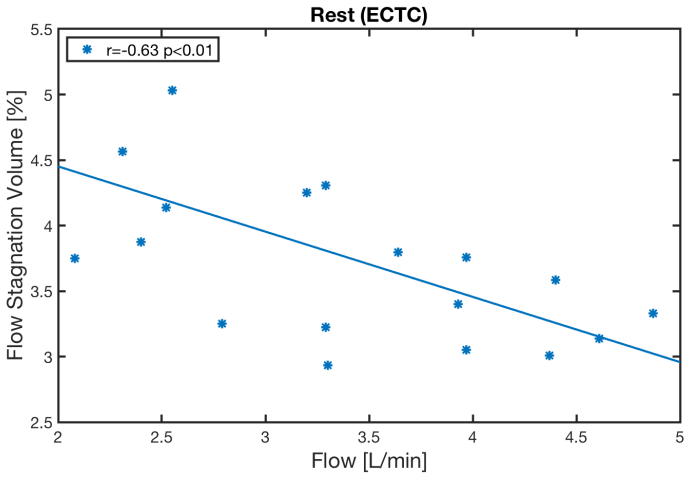

Figure F.3: Flow stagnation volume in the ECTC related to the averaged real-time tunnel flow in a resting condition for the full respiratory cycle.

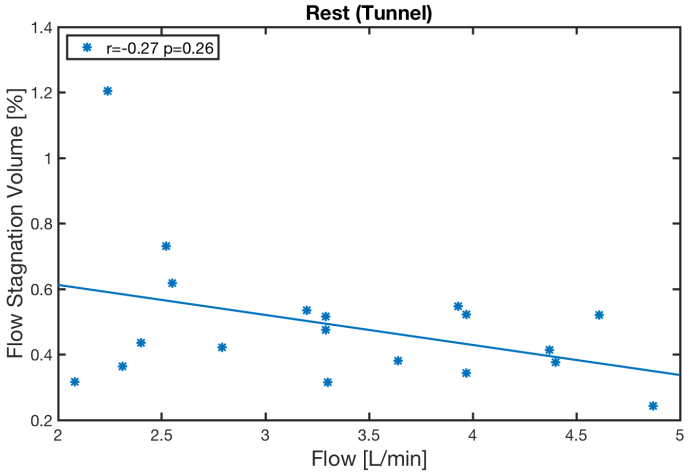

Figure F.4: Flow stagnation volume in the tunnel related to the averaged real-time tunnel flow in a resting condition for the full respiratory cycle.

Table F.1: Correlation between BSA and performance parameters: full respiration cycle, inspiration and expiration in rest and exercise for all included patients.

		Resting condition				**Exercise condition**		
Parameter	N	Full cycle p-value	Inspiration p-value	Expiration p-value	N	Full cycle p-value	Inspiration p-value	Expiration p-value
PL	19	<0.05	<0.05	0.13	17	<0.05	0.01	<0.05
PD	19	0.17	0.10	0.10	17	0.09	0.07	0.0
NR	19	0.23	0.13	0.24	17	0.12	0.09	0.16
FS_{ECTC}	19	0.09	-	-	17	0.07	-	-
FS_{Tunnel}	19	0.52	-	-	17	0.90	-	-

PL is Power Loss [mW]. PD is Pressure Drop [mmHg]. NR is Normalised Resistance [mmHg/L/min/m^2]. FS_{ECTC} is Minimal Flow Stagnation Volume ECTC [%]. FS_{Tunnel} is Minimal Flow Stagnation Volume tunnel [%].

Table F.2: Overall differences in the patient group in rest (N = 17) and exercise (N = 19) condition for all the parameters included also separated for inspiration and expiration phase. Wilcoxon signed rank test.

Parameter	**Condition**	**p-value**
Power Loss	Rest vs. Exercise	<0.001
	Rest: Insp. vs Exp.	<0.001
	Exercise: Insp. vs Exp.	<0.001
	Insp: rest vs. exercise	<0.001
	Exp: rest vs. exercise	<0.001
Pressure Drop	Rest vs. Exercise	<0.001
	Rest: Insp. vs Exp.	<0.001
	Exercise: Insp. vs Exp.	<0.001
	Insp: rest vs. exercise	<0.001
	Exp: rest vs. exercise	<0.001
Normalised Resistance	Rest vs. Exercise	0.001
	Rest: Insp. vs Exp.	0.55
	Exercise: Insp. vs Exp.	0.15
	Insp: rest vs. exercise	<0.001
	Exp: rest vs. exercise	0.001
Flow. Stag. Vol. ECTC	Rest vs. Exercise	<0.001
Flow. Stag. Vol. tunnel	Rest vs. Exercise	<0.001

F.2. Part 1

Table F.3: Power loss for full respiration cycle, inspiration and expiration in rest and exercise (median [IQR]).

		Power Loss Rest [mW]				**Power Loss Exercise [mW]**		
Size	N	Full cyle	Inspiration	Expiration	N	Full cyle	Inspiration	Expiration
16mm	5	7.5 [7.7]	10.6 [11.2][b]	5.1 [4.8][b]	4	56.6 [63.3]	65.9 [71.7]	47.6 [52.7]
18mm	5	3.5 [5.7][a]	5.6 [10.5][ab]	2.3 [2.5][ab]	5	37.6 [37.1][a]	46.2 [49.0][ab]	27.5 [26.4][ab]
20mm	5	4.1 [3.5][a]	6.6 [4.7][ab]	2.9 [3.3][ab]	5	23.5 [27.2][a]	32.2 [30.7][ab]	18.6 [27.3][ab]

[a] Significant difference (p<0.05) between resting and exercise condition. [b] Significant difference (p<0.05) between inspiration and expiration.

Table F.4: Pressure drop for full respiration cycle, inspiration and expiration in rest and exercise (median [IQR]).

		Pressure Drop Rest [mmHg]				**Pressure Drop Exercise [mmHg]**		
Size	N	Full cyle	Inspiration	Expiration	N	Full cyle	Inspiration	Expiration
16mm	5	0.67 [0.37]	0.76 [0.48][b]	0.57 [0.23][bd]	4	2.14 [1.71]	2.29 [1.83]	1.96 [1.56]
18mm	5	0.34 [0.38][a]	0.44 [0.55][a]	0.36 [0.22][ac]	5	1.41 [0.97][a]	1.55 [1.15][ab]	1.24 [0.72][ab]
20mm	5	0.47 [0.12][a]	0.56 [0.19][ab]	0.37 [0.13][ab]	5	1.26 [0.62][a]	1.44 [0.69][ab]	0.96 [0.64][ab]

[a] Significant difference (p<0.05) between resting and exercise condition. [b] Significant difference (p<0.05) between inspiration and expiration. [c] Significant different (p<0.05) from 16 mm conduit size group. [d] Significant different (p<0.05) from 18 mm conduit size group.

Table F.5: Normalised resistance for full respiration cycle, inspiration and expiration in rest and exercise (median [IQR]).

		Normalised Resistance Rest [mmHg/L/min/m^2]				**Normalised Resistance Exercise [mmHg/L/min/m^2]**		
Size	N	Full cyle	Inspiration	Expiration	N	Full cyle	Inspiration	Expiration
16mm	5	0.23 [0.11]	0.23 [0.11]	0.24 [0.11][de]	4	0.29 [0.19]	0.29 [0.20]	0.29 [0.18][e]
18mm	5	0.15 [0.10][a]	0.15 [0.10][a]	0.18 [0.08][ac]	5	0.22 [0.08][a]	0.22 [0.09][a]	0.22 [0.07][a]
20mm	5	0.17 [0.08]	0.18 [0.07][a]	0.17 [0.06][c]	5	0.23 [0.11]	0.23[0.12][a]	0.21 [0.10][c]

[a] Significant difference (p<0.05) between resting and exercise condition. [b] Significant difference (p<0.05) between inspiration and expiration. [c] Significant different (p<0.05) from 16 mm conduit size group. [d] Significant different (p<0.05) from 18 mm conduit size group. [e] Significant different (p<0.05) from 20 mm conduit size group.

Table F.6: Significance of he Wilcoxon signed rank test to test the different condition variables for the three conduit sizes (16, 18 and 20 mm) separately.

Parameter	**Condition**	**16mm:** p-value	**18mm:** p-value	**20mm:** p-value
Power Loss	Rest vs. Exercise	0.07	<0.05	<0.05
	Rest: inspiration vs. expiration	<0.05	<0.05	<0.05
	Exercise: inspiration vs. expiration	0.07	<0.05	<0.05
	Inspiration: rest vs. exercise	0.07	<0.05	<0.05
	Expiration: rest vs. exercise	0.07	<0.05	<0.05
Pressure Drop	Rest vs. Exercise	0.07	<0.05	<0.05
	Rest: inspiration vs. expiration	<0.05	0.08	<0.05
	Exercise: inspiration vs. expiration	0.07	<0.05	<0.05
	Inspiration: rest vs. exercise	0.07	<0.05	<0.05
	Expiration: rest vs. exercise	0.07	<0.05	<0.05
Normalised Resistance	Rest vs. Exercise	0.07	<0.05	0.08
	Rest: inspiration vs expiration	0.35	0.69	0.50
	Exercise: inspiration vs expiration	0.47	0.35	0.14
	Inspiration: rest vs. exercise	0.07	<0.05	<0.05
	Expiration: rest vs. exercise	0.07	<0.05	0.14
Flow. Stag. Vol. ECTC	Rest vs. Exercise	0.07	<0.05	<0.05
Flow. Stag. Vol. tunnel	Rest vs. Exercise	0.16	0.11	<0.05

Table F.7: Significance of the Kruskal-Wallis test, to investigate the difference between the three different sized conduits (16, 18 and 20 mm).

Parameter	**Condition**	**p-value**	**Specification**
Power Loss	Rest	0.20	
	Rest: inspiration	0.43	
	Rest: expiration	0.33	
	Exercise	0.24	
	Exercise: inspiration	0.19	
	Exercise: expiration	0.18	
Pressure Drop	Rest	0.10	
	Rest: inspiration	0.18	
	Rest: expiration	<0.05	16 vs 18mm: $p < 0.05$
	Exercise	0.11	
	Exercise: inspiration	0.19	
	Exercise: expiration	0.12	
Normalised Resistance	Rest	0.07	
	Rest: inspiration	0.07	
	Rest: expiration	<0.05	18 vs 16mm: $p < 0.05$ & 20 vs 16mm: $p < 0.05$
	Exercise	0.13	
	Exercise: inspiration	0.23	
	Exercise: expiration	<0.05	20 vs 16mm: p <0.05
Flow. Stag. Vol. ECTC	Rest	0.99	
	Exercise	0.62	
Flow. Stag. Vol. tunnel	Rest	0.6	
	Exercise	0.82	

F.3. Part 2

Table F.8: Significance of Spearman correlation between BSA and power loss.

		Power Loss: rest				**Power Loss: exercise**		
Size	N	Full cycle p-value	Inspiration p-value	Expiration p-value	N	Full cycle p-value	Inspiration p-value	Expiration p-value
16 mm	5	<0.05	<0.01	0.80	4	0.20	0.20	0.60
18 mm	5	0.75	0.75	1.00	5	0.29	0.29	0.10

Table F.9: Significance of Spearman correlation between BSA and pressure drop.

		Pressure Drop: rest				**Pressure Drop: exercise**		
Size	N	Full cycle p-value	Inspiration p-value	Expiration p-value	N	Full cycle p-value	Inspiration p-value	Expiration p-value
16 mm	5	<0.05	<0.01	0.19	4	0.20	0.20	0.60
18 mm	5	0.87	0.75	0.62	5	0.75	0.75	0.49

Table F.10: Significance of Spearman correlation between BSA and normalised resistance.

		Normalised Resistance: rest				**Normalised Resistance: exercise**		
Size	N	Full cycle p-value	Inspiration p-value	Expiration p-value	N	Full cycle p-value	Inspiration p-value	Expiration p-value
16 mm	5	<0.01	<0.01	<0.01	4	0.20	0.20	0.20
18 mm	5	0.39	0.39	0.19	5	0.87	0.75	0.87

Table F.11: Significance of Spearman correlation between BSA and minimal flow stagnation volume in the ECTC

		Min. Flow Stag. Volume ECTC: rest		**Min. Flow. Stag. Volume ECTC: exercise**
Parameter	N	p-value	N	p-value
16 mm	5	<0.05	4	<0.01
18 mm	5	0.29	5	0.29

Table F.12: Significance of Spearman correlation between BSA and minimal flow stagnation volume in the tunnel.

		Min. Flow Stag. Volume tunnel: rest		**Min. Flow. Stag. Volume tunnel: exercise**
Parameter	N	p-value	N	p-value
16 mm	5	0.09	4	0.37
18 mm	5	0.62	5	0.62